

**26th IEPC
'99**



IEPC 99-217

Computation of Current to a Moving Bare Tether

**T. Onishi and M. Martinez-Sanchez,
MIT, Cambridge, MA USA**

**D.L. Cooke,
Air Force Research Laboratory,
Space Vehicle Directorate, Hanscom AFB,
MA, USA**

20010124 002

**26th International Electric Propulsion Conference
October 17-21, 1999, Kitakyushu, Japan**

REPORT DOCUMENTATION PAGE

Public reporting burden for this collection of information is estimated to average 1 hour per response, including gathering and maintaining the data needed, and completing and reviewing the collection of information. Send comments regarding this burden estimate or any other aspect of this collection of information, including suggestions for reducing this burden, to Washington Headquarters Service, Paperwork Project, Suite 1204, Arlington, VA 22202-4302, and to the Office of Management and Budget, Paperwork Project, Suite 1204, Arlington, VA 22202-4302.

AFRL-SR-BL-TR-00-

sources,
t of this
fferson

1. AGENCY USE ONLY (Leave blank)		2. REPORT DATE 18 Dec 00	3. RE Final Report: 15 Jul 95 To 14 Jul 99
4. TITLE AND SUBTITLE 3-D Model Developments for Plasma Plumes			5. FUNDING NUMBERS F49620-95-1-0444
6. AUTHOR(S) Prof. D.E. Hastings Prof. M. Martinez Sanchez			
7. PERFORMING ORGANIZATION NAME(S) AND ADDRESS(ES) Massachusetts Institute Of Technology 77 Massachusetts Avenue Room E19-719 Cambridge, Massachusetts 02139			8. PERFORMING ORGANIZATION REPORT NUMBER
9. SPONSORING/MONITORING AGENCY NAME(S) AND ADDRESS(ES) AFOSR 801 N. Randolph St. Arlington VA 22203			10. SPONSORING/MONITORING AGENCY REPORT NUMBER
11. SUPPLEMENTARY NOTES			
12a. DISTRIBUTION AVAILABILITY STATEMENT Approved for Public Release: Distribution is unlimited			12b. DISTRIBUTION CODE
13. ABSTRACT (Maximum 200 words) Two different studies were supported under this AASERT Grant, One, performed by Master's Candidate, Gregory Yashko, examined the technical feasibility and economic impact of clusters of micro-satellites propelled by micro-ion engines. It was concluded that sensor distribution among several satellites is appropriate when savings from the increased reliability outweigh the increased deployment costs, and that large constellations of g-satellites could feasibly perform missions currently being carried out by large satellites. It was also found that the performance of micro-fabricated linear ion thrusters ~s poor because of insufficient primary electron confinement, so other micro-propulsion concepts appear to be necessary for implementation of g-sat clusters. The other study was carried out by Master's (later Ph.D.) candidate, Tatsuo Onishi, and it concerned the numerical modeling of electron capture by an ionospheric orbiting bare tether. A PIC method was developed for the simplified case in which magnetic field and relative plasma motion are ignored, and good agreement was found with classical results of Probe Theory for this case. These results opened the way for simulation of realistic tether configurations, a work which is now continuing under separate funding.			
14. SUBJECT TERMS 3-D Model Developments For Plasma Plumes			15. NUMBER OF PAGES
			16. PRICE CODE
17. SECURITY CLASSIFICATION OF REPORT UNCLASSIFIED	18. SECURITY CLASSIFICATION OF THIS PAGE UNCLASSIFIED	19. SECURITY CLASSIFICATION OF ABSTRACT UNCLASSIFIED	20. LIMITATION OF ABSTRACT UL

Computation of Current to a Moving Bare Tether

Tatsuo Onishi* and Manuel Martinez-Sanchez†

Massachusetts Institute of Technology

Cambridge, Massachusetts, USA

David L. Cooke

Air Force Research Laboratory

Space Vehicle Directorate, Hanscom AFB, MA, USA

Abstract

An electrodynamic bare tether has been considered as an alternative method of propulsion without expenditure of propellant. The object of the work reported here is the development of a numerical method, Particle-In-Cell method, for the calculation of electron current to a positive bare tether moving at orbital velocity in the ionosphere, i.e. in a flowing magnetized plasma under Maxwellian collisionless conditions. The code uses the quasi-neutrality condition to solve for the local potential at points in the plasma which coincide with the computational outside boundary. Given the boundary conditions, Poisson equation is solved in such a way that the presheath region can be captured in the computation. Electrons are assumed to have a Maxwellian distribution at the boundary due to their high mobility, whereas ions are assumed so only in the far upstream region and are also assumed to only decelerate one dimensionally due to their large mass. The results indicate a stable convergence, and clearly represent a presheath region. Collected currents turn out to be more than that predicted by the Orbital Motion Limit (OML) theory.

Introduction

In tethered satellite technology, it is important to estimate how many electrons a spacecraft can collect from its ambient plasma by its positively charged electrodynamic tether. The analysis is, however, quite complicated because of the small but significant Geomagnetic field and the spacecraft's relative motion to both ions and electrons. One of the approaches to this solution is the numerical method. In the numerical analysis of space plasma, one of the most reliable methods has been the Particle-In-Cell (PIC) method. In this paper we develop a PIC code for a two dimensional collisionless plasma under the

effects of magnetic field and the spacecraft's relative motion.

This paper is the continuation of the authors' work on a quiescent unmagnetized plasma [1]. In [1], the quasi-neutral condition was used to obtain the outside boundary condition for the Poisson solver. The quasi-neutral condition requires local densities of electrons and ions at points on the outside boundary. In computation, each density consists of two parts; one due to the incoming particles and the other due to the outgoing particles. Based on same assumptions, the density of the incoming particles can be analyzed and expressed as a function of the local potential. The density of the outgoing particles is computed by using the same technique in [1], namely, by estimation from the numerical results for the previous time step.

Since some electrons are absorbed on the surface of the tether, there is also a region called "presheath" outside the sheath, where the quasi-neutrality prevails but the electric potential is not equal to that of the ambient plasma at infinity. Thus, in order to reproduce the presheath region in the computation, the quasi-neutral condition is physically very reasonable.

In the wake region behind the tether, the Debye lengths of electrons become very large due to the low electron density, which in turn is due to the fact that ions are deflected by the tether potential and thus do not reside in that region. The large Debye length may exclude the quasi-neutral condition where the computational grid is smaller than the local Debye length. In our computation, we apply the quasi-neutrality where we can obtain the potential from it, otherwise we use the zero-gradient condition.

Computation

The major difficulty of a PIC method applied to an infinitely large plasma appears in the specification of the computational outside boundary condition, namely the velocity distribution func-

*Ph.D. Candidate

†Professor

Magnetic field	0.3 Gauss
Ion mass (O^+)	2.67×10^{-27} kg
Electron temperature	0.1 eV
Ion temperature	0.1 eV
Electron thermal velocity	212 km/sec
Ion thermal velocity	1 km/sec
Satellite speed	8 km/sec
Electron gyro radius	2.5 cm
Ion gyro radius	430 cm
Electron (Ion) density	$10^{11}/m^3$
Ion gyro radius	0.74 cm

Table 1: Physical parameters

tion at a boundary point. In order to treat the boundary, we assume Maxwellian velocity distribution¹ for electrons at the boundary and translating Maxwellian velocity function for ions at the far upstream. First, based on the assumption that ions are Maxwellian in the far upstream region and are accelerated/decelerated one dimensionally, we show the ion distribution function at the boundary as a function of the local potential. From this function, we calculate the density, which is required for the quasi-neutral condition, and the flux, which is required to calculate the number of ions replenished into the computational domain per timestep. Electrons are assumed to have a Maxwellian distribution at the boundary due to the fact that the electron thermal velocity is much faster than the satellite orbital speed.

The parameters used in this computation are typically as shown in Table 1.

Ions

Due to their large mass, ions are very slow compared to the satellite speed. This fact leads us to the assumption that ions are Maxwellian only in the far upstream region and that each ion is decelerated one-dimensionally by the potential field created by the tether. The latter assumption may be verified by the fact that in the frame moving with a tether, the major velocity component of an ion is in the direction of the tether velocity, but of opposite sign. Even if the ion is accelerated in a random direction, the major component of the ion velocity is still the same. Therefore the ion trajectory remains almost straight, leading to the assumption.

The ion density is obtained as follows. Assuming a Maxwellian distribution for ions in the plasma frame, we have an ion distribution function in the

far upstream region as

$$f_{ion,\infty} = n_\infty \left(\frac{m_i}{2\pi\kappa T_i} \right)^{3/2} \exp \left\{ -\frac{(w_x - U)^2 + w_y^2 + w_z^2}{v_{Ti}^2} \right\} \quad (1)$$

where n_∞ is ion density at infinity, m_i ion mass, T_i ion temperature, w_x, w_y and w_z , x-, y- and z-components of a particle velocity respectively, U the tether velocity (in the x-direction) and $v_{Ti} \equiv \sqrt{2\kappa T_i/m_i}$. From the energy conservation between infinity (the far upstream region) and a boundary point, we have

$$\frac{1}{2} m_i w_x^2 = \frac{1}{2} m_i \hat{w}_x^2 + Ze\hat{\phi}_b \quad (2)$$

$$w_y \approx \hat{w}_y \quad (3)$$

$$w_z \approx \hat{w}_z \quad (4)$$

where \hat{w}_x is an x-component of a particle velocity at a boundary point and $\hat{\phi}_b$ is a boundary potential. Substituting (2) into (1), we get the ion distribution function at the boundary as

$$\hat{f}_{ion,b} = \xi_i \exp \left[-\frac{\left(\sqrt{\hat{w}_x^2 + \frac{2e\hat{\phi}_b}{m_i}} - U \right)^2 + \hat{w}_y^2 + \hat{w}_z^2}{v_{Ti}^2} \right] \quad (5)$$

where $\xi_i = n_\infty (m_i/2\pi\kappa T_i)^{3/2}$. Hereafter we omit the hat to denote the quantities at the boundary. From this function, we obtain density and flux of incoming ions as a function of the boundary potential.

The density is given by

$$n_i^{in} = \int_0^\infty \lambda_i \exp \left[-\frac{\left(\sqrt{w_x^2 + \frac{2e\phi_b}{m_i}} - U \right)^2}{v_{Ti}^2} \right] dw_x \quad (6)$$

for $\phi_b > 0$, and

$$n_i^{in} = \int_{\sqrt{-\frac{2e\phi_b}{m_i}}}^\infty \lambda_i \exp \left[-\frac{\left(\sqrt{w_x^2 + \frac{2e\phi_b}{m_i}} - U \right)^2}{v_{Ti}^2} \right] dw_x \quad (7)$$

for $\phi_b < 0$, where the integral over w_y and w_z has been carried out, and $\lambda_i = n_\infty \sqrt{m_i/2\pi\kappa T_i}$. The flux is then given as

$$\Gamma_i^{in} = \int_0^\infty \lambda_i w_x \exp \left[-\frac{\left(\sqrt{w_x^2 + \frac{2e\phi_b}{m_i}} - U \right)^2}{v_{Ti}^2} \right] dw_x \quad (8)$$

for $\phi_b > 0$ and

$$\Gamma_i^{in} = \int_{\sqrt{-\frac{2e\phi_b}{m_i}}}^\infty \lambda_i w_x \exp \left[-\frac{\left(\sqrt{w_x^2 + \frac{2e\phi_b}{m_i}} - U \right)^2}{v_{Ti}^2} \right] dw_x \quad (9)$$

for $\phi_b < 0$. In consequence of the approximation, we assume no ions coming into the computational domain from downstream. Therefore, we have

$$n_i^{in} = 0 \quad (10)$$

$$\Gamma_i^{in} = 0 \quad (11)$$

for the downstream boundary.

¹Flowing effects on electrons are discussed and formulated in Appendix.

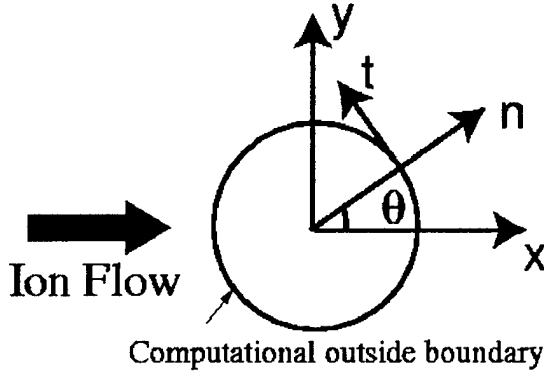


Figure 1: Geometry of Computation

Electrons

From Table 1 we see that electrons have a high mobility so that they reach the thermal equilibrium quickly. Assuming a Maxwellian distribution for incoming electrons at the boundary, we have

$$f_{e,b} = \xi_e \exp \left[-\frac{w_x^2 + w_y^2 + w_z^2}{v_{Te}^2} \right] \exp \left[\frac{e\phi_b}{\kappa T_e} \right] \quad (12)$$

where $\xi_e \equiv n_\infty (m_e/2\pi\kappa T_e)^{3/2}$. When $\phi_b < 0$, an electron has been decelerated by the time it reaches the boundary. Thus the minimum speed of an electron entering into the computational domain is still zero, otherwise it is $\sqrt{\frac{2e\phi_b}{m_e}}$. To facilitate the calculation of the local density and flux of incoming electrons, we change variables from (w_x, w_y) to (w_n, w_t) where w_n is the normal velocity component to the boundary surface, w_t the tangent component,

$$w_x = w_n \cos \theta - w_t \sin \theta \quad (13)$$

$$w_y = w_n \sin \theta + w_t \cos \theta \quad (14)$$

where θ is the angle between the normal of the surface and the plasma flow (in the positive x-direction) (See Figure 1).

Then we have a Maxwellian distribution function as

$$f_{e,b} = \Xi_e \exp \left[-\frac{m_e \{w_n^2 + w_t^2 + w_z^2\}}{2\kappa T_e} \right] \quad (15)$$

where

$$\Xi_e \equiv n_\infty \left(\frac{m_e}{2\pi\kappa T_e} \right)^{3/2} \exp \left(\frac{e\phi_b}{\kappa T_e} \right) \quad (16)$$

For $\phi_b < 0$, the density of incoming electrons at the boundary is given by

$$n_e^{in} = \int_{-\infty}^{\infty} \int_{-\infty}^{\infty} \int_{-\infty}^{\infty} f_{e,b} dw_n dw_t dw_z \quad (17)$$

$$= \frac{n_\infty}{2} \exp \left(\frac{e\phi_b}{\kappa T_e} \right) \quad (18)$$

When $\phi_b > 0$, all electrons are accelerated including a particle corresponding to $w = 0$ at infinity in the plasma frame. This particle is also accelerated by the positive potential, raising the minimum velocity of incoming electrons up to $\sqrt{\frac{2e\phi_b}{m_e}}$. Therefore electrons slower than this velocity are prohibited from entering the computational domain. The density of incoming electrons thus becomes

$$n_e^{in} = \Xi_e \iiint_{V \text{ except for } I_p} \exp \left\{ -\frac{w_n^2 + w_t^2 + w_z^2}{v_{Te}^2} \right\} d\vec{w} \quad (19)$$

where

$$V : \{-\infty < w_n < 0; -\infty < w_t < \infty; -\infty < w_z < \infty\} \quad (20)$$

$$I_p : w_n^2 + w_t^2 + w_z^2 \leq \frac{2e\phi_b}{m_e} \quad (21)$$

After some algebra, the density becomes

$$n_e^{in} = \frac{n_\infty}{2} \left\{ \exp \left(\frac{e\phi_b}{\kappa T_e} \right) \operatorname{erfc} \left(\sqrt{\frac{e\phi_b}{\kappa T_e}} \right) + \frac{2}{\sqrt{\pi}} \sqrt{\frac{e\phi_b}{\kappa T_e}} \right\} \quad (22)$$

not there. case with β , w_z is not constant. this factor should be 1

Electron flux is calculated likewise. For $\phi_b < 0$, we have

$$\Gamma_e^{in} = \int_{-\infty}^{\infty} \int_{-\infty}^{\infty} \int_{-\infty}^0 -w_n f_{e,b} dw_n dw_t dw_z \quad (23)$$

$$= \frac{n_\infty v_{Te}}{2\sqrt{\pi}} \exp \left(\frac{e\phi_b}{\kappa T_e} \right) \quad (24)$$

And for $\phi_b > 0$, we have

$$\Gamma_e^{in} = \Xi_e \iiint_{V \text{ except for } I_p} w_n \exp \left\{ -\frac{w_n^2 + w_t^2 + w_z^2}{v_{Te}^2} \right\} d\vec{w} \quad (25)$$

After some algebra, we obtain

$$\Gamma_e^{in} = \frac{n_\infty v_{Te}}{2\sqrt{\pi}} \left(\frac{e\phi_b}{\kappa T_e} + 1 \right) \quad (26)$$

Quasineutrality Condition

As shown above, densities due to incoming particles are given as a function of the local boundary potential ϕ_b . In [1], densities due to outgoing particles are calculated numerically by

$$n_{e,i}^{out} = \frac{k^2}{\sum_{i=1}^k \vec{w}_i \cdot \vec{n} dt S} \quad (27)$$

where k is the number of particles going out of the computational domain at a local boundary point (in computation, it is a cell), \vec{w}_i the particle velocity going out, \vec{n} the normal vector of the boundary surface, S the surface area, all of which are calculated at the same boundary point. The quasi-neutral condition is applied by equating the electric charge density of outgoing particles and incoming particles to zero. Densities of incoming particles are given as a function of a local boundary potential ϕ_b .

$$n_i^{out} - n_e^{out} = n_e^{in}(\phi_b) - n_i^{in}(\phi_b) \quad (28)$$

The boundary potential, ϕ_b , is solved numerically from (28), and used as a boundary condition in a Poisson solver.

Results

In this section, we show the results from our simulations. First, we consider the numerical convergence and stability. Figure 2 shows the sum of total energies of all particles in the computational domain. In this figure, we see the convergence of overall total energy of particles and the energy increase reported in [3] is not identified. This is because, in our simulations, particles refresh their energy once they either are absorbed by a tether or go out of the computational domain, and then are recycled for the computation. Therefore particles do not accumulate a numerical error throughout the simulation.

Figure 3 shows the number of particles which reside in the computational domain. It also indicates a steady state and does not show an increase in time as reported before [[5]].

Figure 4 shows typical trajectories of electrons. The effect of the magnetic field can be seen in the ram region where an electron is trapped in the field line. In and near the wake, due to the depletion of ions in the wake (Figure 5), the electric potential becomes negative with respect to infinity (Figure 6) so that most of the electrons are reflected by this potential bump. In the immediate vicinity of the tether, electric field effects become dominant over magnetic field effects. Thus the magnetization effect on electrons becomes very small.

Due to the high positive potential on the tether, ions are decelerated and deflected from its quasi one-dimensional trajectory, giving rise to a narrow layer in the shape of a bow shock in front of the tether, where ion density is high because ion trajectories are tangent to it (an "acoustic" surface) (Figure 5). The potential at the ion stagnation point is equal to the ion ram energy (5eV).

In order to maintain the quasi-neutrality, electrons are attracted to the ion "bow shock" (Figure 7). In Figure 8, right in front of the stagnation point, quasi-neutral electric charge density is recognized. To attract electrons along that magnetic field line, a positive potential "wing" spreads out along this field line, since the source of electrons is only from this direction, whereas electrons residing in front of this potential "wing" are trapped by the magnetic field, and can not contribute to the quasi-neutrality near the tether.

Finally Figure 9 shows the collected current and OML current. The collected current turns out to be twice as much as the OML current. This current collection may be partially attributed to the fact that, although the geometry is 2-dimensional (a long cylindrical tether), particles are accelerated 3-dimensionally through the magnetic gyration. That is, a particle which has an in-plane velocity equal to zero at infinity can have an in-plane velocity faster

than $\sqrt{\frac{2e\phi_b}{m_e}}$ at a boundary, whereas without the gyration, this is the velocity it must have at the boundary. This leads to more one-sided flux into the domain, hence more current collection. However further analysis should be performed to verify the correctness of this current collection result.

In conclusion, we present in this paper a PIC technique to treat the boundary for flowing magnetized plasmas. This method shows numerical convergence and stability. And as a preliminary result, we obtain a current collection which is twice as much as OML current.

Acknowledgement

This work is supported through a grant from the USAF space vehicle directorate.

Appendix: Flow effects on electrons

In this paper, we assumed a Maxwellian distribution for electrons at the boundary. When $U = 0$ this assumption becomes exact, since the Maxwellian distribution function is in the form of $\exp\left(-\frac{E}{\kappa T_e}\right)$ where $E = \frac{1}{2}m_e w^2 - e\phi$. Therefore under Maxwellian collisionless conditions, this is the exact solution at the boundary. However for $U \neq 0$, the distribution function given by

$$\hat{f}_{e,b} = \xi_e \exp\left[-\frac{(w_x - U)^2 + w_y^2 + w_z^2}{v_{Te}^2}\right] \exp\left[\frac{e\phi_b}{\kappa T_e}\right] \quad (29)$$

, where $\xi_e \equiv n_\infty (m_e/2\pi\kappa T_e)^{3/2}$, is in the form of $\exp\left(-\frac{E - m_e U w_x}{\kappa T_e}\right)$. Then the w_x term produces an error as the same distribution function (29) is assumed at the boundary as at infinity. In this appendix, the simulation using the shifted Maxwellian distribution (29) at the boundary is shown. And the result is compared with the case of Maxwellian distribution (12) and the error is discussed.

As we derived the density of incoming electrons from (12) to (18) and (22) and the flux from (12) to (24) and (26), we likewise derive the density and the flux from (29) with

$$V : \{-\infty < w_n < 0; -\infty < w_t < \infty; -\infty < w_z < \infty\} \quad (30)$$

$$I_p : (w_n - U \cos \theta)^2 + (w_t + U \sin \theta)^2 + w_z^2 \leq \frac{2e\phi}{m_e} \quad (31)$$

The result is as follows; The density is for $U \cos \theta \geq \sqrt{2e\phi/m_e}$ and for $\phi_b < 0$

$$n_e^{in} = \frac{n_\infty}{2} \exp\left(\frac{e\phi}{\kappa T_e}\right) \operatorname{erfc}\left(\frac{U}{v_{2t}} \cos \theta\right) \quad (32)$$

, for $U \cos \theta \leq -\sqrt{2e\phi/m_e}$

$$n_e^{in} = n_\infty \exp\left(\frac{e\phi}{\kappa T_e}\right) \operatorname{erfc}\left(\sqrt{\frac{e\phi}{\kappa T_e}}\right) + \frac{2}{\sqrt{\pi}} n_\infty \sqrt{\frac{e\phi}{\kappa T_e}} - \frac{n_\infty}{2} \exp\left(\frac{e\phi}{\kappa T_e}\right) \operatorname{erfc}\left(-\frac{U}{v_{Te}}\right) \quad (33)$$

and $|U \cos \theta| \leq \sqrt{2e\phi/m_e}$

$$n_e^{in} = \frac{n_\infty}{2} \left\{ \exp\left(\frac{e\phi}{\kappa T_e}\right) \operatorname{erfc}\left(\sqrt{\frac{e\phi}{\kappa T_e}}\right) + \frac{2}{\sqrt{\pi}} \left[\sqrt{\frac{e\phi}{\kappa T_e}} - \frac{U}{v_{Te}} \cos \theta \right] \right\} \quad (34)$$

And the flux is for $U \cos \theta \geq \sqrt{2e\phi/m_e}$ and for $\phi_b < 0$

$$\Gamma_e^{in} = \frac{n_\infty v_{Te}}{2\sqrt{\pi}} \left[\exp\left(\frac{e\phi_b}{\kappa T_e} - \frac{U^2}{v_{Te}^2} \cos^2 \theta\right) - \sqrt{\pi} \frac{U}{v_{Te}} \cos \theta \exp\left(\frac{e\phi_b}{\kappa T_e}\right) \operatorname{erfc}\left(\frac{U}{v_{Te}} \cos \theta\right) \right] \quad (35)$$

, for $U \cos \theta \leq -\sqrt{2e\phi/m_e}$

$$\Gamma_e^{in} = \frac{n_\infty v_{Te}}{2\sqrt{\pi}} \left[\exp\left(\frac{e\phi_b}{\kappa T_e} - \frac{U^2}{v_{Te}^2} \cos^2 \theta\right) - 2\sqrt{\frac{e\phi_b}{\kappa T_e}} \frac{U}{v_{Te}} \cos \theta - \sqrt{\pi} \frac{U}{v_{Te}} \cos \theta \exp\left(\frac{e\phi_b}{\kappa T_e}\right) \left\{ 1 - 2\operatorname{erf}\left(\sqrt{\frac{e\phi_b}{\kappa T_e}}\right) - \operatorname{erf}\left(\frac{U}{v_{Te}} \cos \theta\right) \right\} \right] \quad (36)$$

and for $|U \cos \theta| \leq \sqrt{2e\phi/m_e}$

$$\Gamma_e^{in} = \frac{n_\infty v_{Te}}{2\sqrt{\pi}} \left[\frac{e\phi_b}{\kappa T_e} - 2\sqrt{\frac{e\phi_b}{\kappa T_e}} \frac{U}{v_{Te}} \cos \theta + \frac{U^2}{v_{Te}^2} \cos^2 \theta + 1 - \sqrt{\pi} \frac{U}{v_{Te}} \cos \theta \exp\left(\frac{e\phi_b}{\kappa T_e}\right) \operatorname{erfc}\left(\sqrt{\frac{e\phi_b}{\kappa T_e}}\right) \right] \quad (37)$$

With these equations, the same simulation is performed. The result shows the current collection which is 20% more than the case of $U = 0$ (Figure 10). From this we can deduce that the error of using the non-shifted Maxwellian distribution function at the boundary is of the same order.

References

- [1] Onishi, T., *Electron Current Collection by a Positively Charged Tether, Using a Particle-In-Cell Method*. Master's Thesis, MIT (Aeronautics/Astronautics) May 1998
- [2] Cooke, D.L. and I. Katz, *TSS-1R electron currents: Magnetic limited collection from a heated presheath*, Geophys. Res. Lett., Vol.25, No.5, Pages753-756, March 1,1998

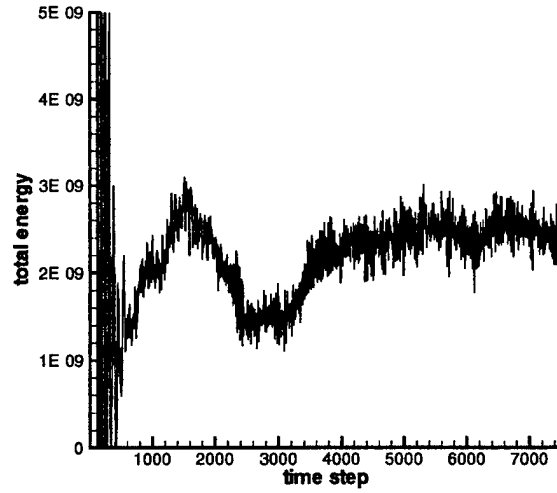


Figure 2: Total energy of particles in a domain

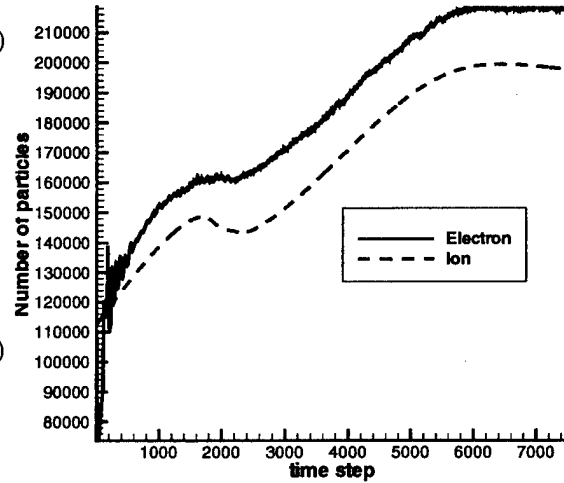


Figure 3: Number of particles in a domain

- [3] Birdsall, C.K. and A.B. Langdon, *Plasma Physics via computer simulation*, Institute of Physics Publishing, Bristol and Philadelphia, 1991.
- [4] Chung, P.M., L. Talbot and K.J. Touryan, *Electric Probes in Stationary and Flowing Plasmas; Theory and Application*, Springer-Verlag, 1975.
- [5] Singh, N., W.C. Leung and B.I. Vashi, *Potential structure near a probe in a flowing magnetoplasma and current collection*, J. of Geophys. Res., Vol. 102, No.A1, Pages 195-208, January 1, 1997.

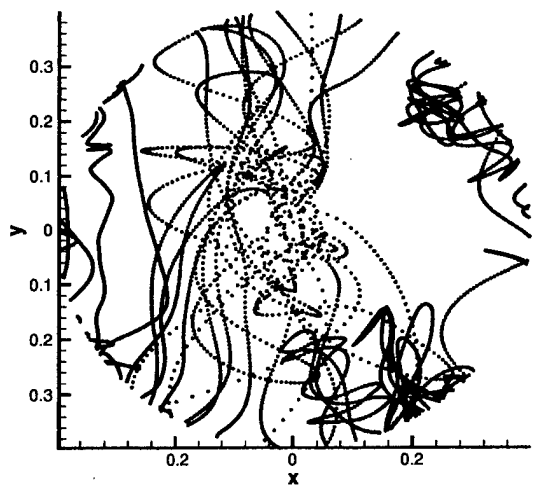


Figure 4: Trajectory of electrons

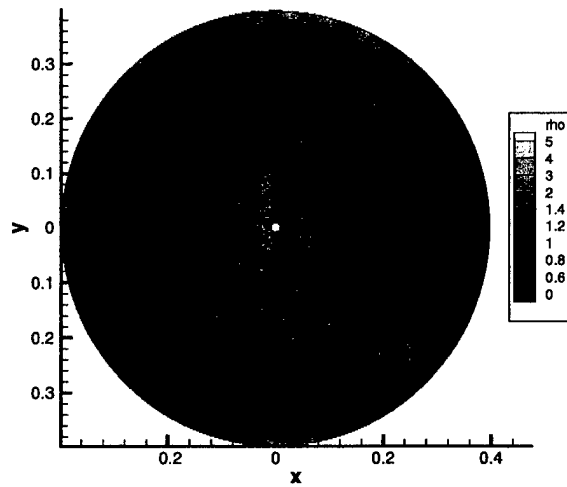


Figure 7: Electron density

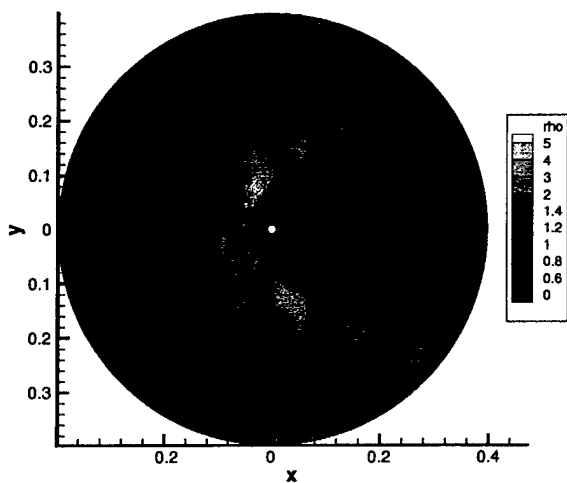


Figure 5: Ion density

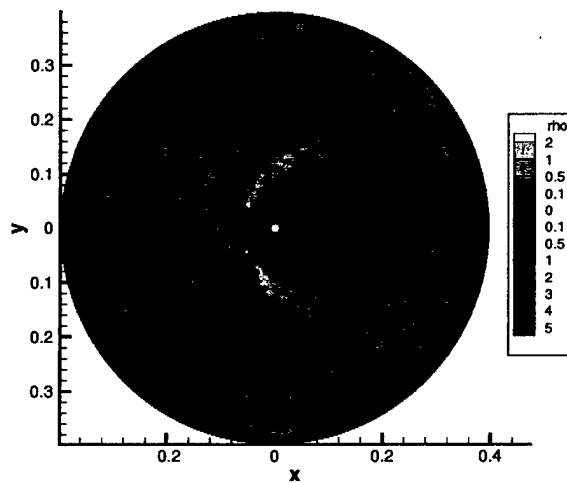


Figure 8: Electric charge density

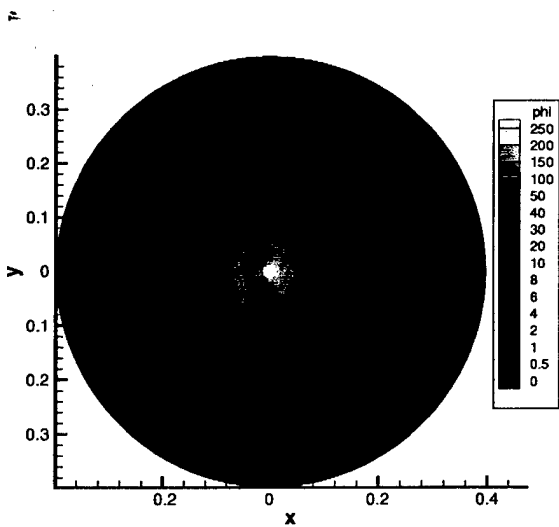


Figure 6: Electric potential

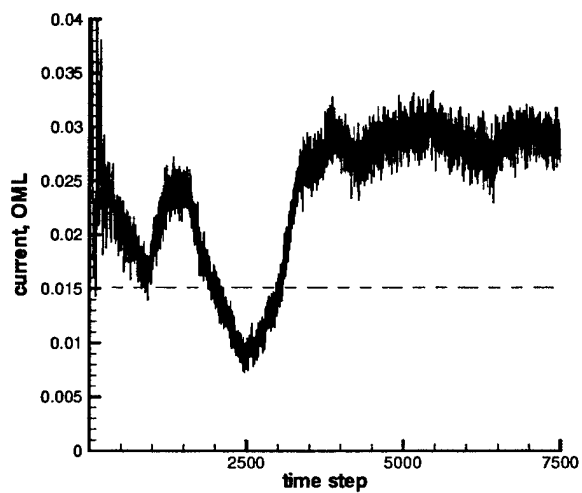


Figure 9: Collected current and OML current

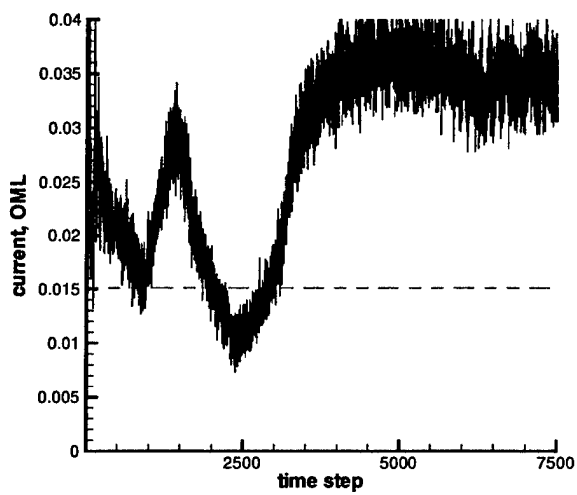


Figure 10: Collected current and OML current

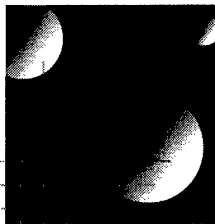
**Ion Micro-Propulsion and Cost
Modeling for Satellite Clusters**

Gregory Yashko

June 1998

SERC #9-98

(Under the supervision of Prof. Manuel Martinez-Sanchez)



*MIT
Space
Engineering
Research
Center*

Massachusetts
Institute of
Technology

Cambridge
Massachusetts
02139

Ion Micro-Propulsion and Cost Modeling for Satellite Clusters

by

Gregory Yashko

Submitted to the Department of Aeronautics and Astronautics
in partial fulfillment of the requirements for the degrees of

Master of Science in Aeronautics and Astronautics
and
Master of Science in Technology and Policy

Abstract

This thesis carries out both technical and policy analyses on a progression of topics. These topics are cost modeling of distributed satellite systems, determination of propulsion system requirements for satellite clusters and swarms, and an analysis of ion micropropulsion systems for use in swarms of microsatellites. The total cost over a 10 year mission life is calculated for configurations of the NPOESS mission in which the primary instruments were distributed among three smaller satellites. This increased reliability of the distributed configuration substantially reduces the number of ground and on-orbit spares required. As a result, mission costs are reduced compared to a single large satellite configuration. The relative positions of satellites in a cluster are altered by "tidal" accelerations which are a function of the cluster baseline and orbit altitude. Near continuous thrusting by a propulsive system was found necessary to maintain the relative positions of the satellites within allowable tolerances. Satellite mass, volume, and power constraints limit reasonable cluster baselines to approximately 30 m, 300 m, and 5000 m at 1000 km, 10,000 km, and GEO altitudes respectively. To maintain these cluster baselines, the propulsive system must operate at specific impulses and efficiencies consistent with those of ion engines. The performance of the linear ion microthruster concept is examined using Brophy's model to predict energy costs per beam ion. Efficiency of the linear ion microthruster was calculated to be in the range of 15%. At this efficiency, the linear ion microthruster is not able to perform station keeping requirements for cluster missions.

This page intentionally left blank

Acknowledgments

Completion of this thesis would not have been possible without the help of numerous individuals. First, I need to thank my mom for typing literally half the contents of this thesis while I recovered from tendonitis in my wrists (too many hours slaving away in the lab!). Her help included countless hours while I was at home on breaks and flights to Boston as deadlines approached.

Next, I want to acknowledge the contributions of my advisors, Professor Daniel Hastings and Professor Manuel Martinez-Sanchez. Their insight and experience kept me on track despite my efforts to pursue many dead ends.

I would be remiss if I did not mention those in the Space Systems Lab, especially Greg Giffin, Graeme Shaw and Ray Sedwick. At least the hours we spent there were broken up by some humor and an occasional softball game.

I can hardly express my feelings for my fiancée Kristin who, in coming to Boston, put her life on hold for a year so that we could be together.

Foremost, however, credit goes to my parents for their emotional and financial support in raising their sons. Their many sacrifices over the years have provided us with the opportunity to earn seven degrees among the three of us.

TABLE OF CONTENTS

Chapter 1 Introduction

1.1 Background	
1.1.1 Cost Modeling of Distributed Satellite Systems	11
1.1.2 Analysis of Cluster Missions.....	13
1.1.3 Modeling Performance of Micro Ion Engines.....	14
1.2 Preview of Chapters	16
1.3 Summary	17

Chapter 2 To Distribute or Not to Distribute: A Policy Analysis

2.1 Introduction to Distributed Systems	19
2.2 Considerations for Implementing Distributed Satellite Systems	20
2.2.1 Complexity	21
2.3 Modeling Distributed Satellite Systems	22
2.3.1 Model Overview	23
2.3.2 Payload Cost Model	24
2.3.3 Satellite Bus Cost Model	26
2.3.4 Similarity Factor	28
2.3.5 Learning Curve And Discounting	29
2.3.6 Replacement Model	30
2.4 Results Of Cluster Configuration Analysis	31
2.4.1 Cost Breakdown for Cluster Configurations	32
2.4.2 Total Mission Costs	34
2.4.3 Sensitivity of Costs to Instrument Reliability	37
2.5 Other Implementation Considerations	40
2.6 Summary and Conclusions	42

Chapter 3 Thruster Requirements for Local Satellite Clusters

3.1 Introduction to cluster missions	47
3.1.1 Synthetic Apertures	47
3.1.2 Interferometry / Sparse Arrays	48
3.1.3 Local Satellite Clusters	50
3.2 Orbital Dynamics Of Satellite Clusters	52
3.2.1 Tidal Forces	52
3.2.2 Impulsive vs. Continuous Thrusting	55
3.2.3 Dynamic Clusters	58
3.3 Propulsion System Requirements	60
3.3.1 Current Thruster Characteristics	60
3.3.2 Methodology	61
3.3.3 Analysis of Cluster Missions	64
3.4 Summary and Conclusions	69

Chapter 4 Numerical Modeling of Ion Engines

4.1 Operation of Ion Engines	71
4.2 Brophy's Model	72

4.2.1	Fundamental Equations	73
4.2.2	Discharge Energy Balance	74
4.2.3	Survival Equation for Primary Electrons	75
4.2.4	Calculation of Primary / Secondary Population Ratio	77
4.2.5	Calculation of Utilization Efficiency	81
4.3	Arakawa Algorithm	84
4.3.1	Magnetic Field Analysis	84
4.3.2	Primary Electron Containment Length	85
4.3.3	Discharge Chamber Performance	86
4.4	Summary	87
Chapter 5 Scaling of Cylindrical Ion Engines		
5.1	Scaling Argument	89
5.2	Scaling of Cylindrical Chambers	93
5.3	Summary And Conclusions	98
Chapter 6 Design Considerations of the Linear Ion Microthruster		
6.1	Introduction to the Linear Ion Microthruster.....	101
6.2	Performance of Linear Geometry	103
6.2.1	Determination of Electron Confinement Length	103
6.2.2	Energy Costs per Beam Ion	104
6.2.3	Mapping Ion Energy Cost to Efficiency.....	108
6.3	Linear ion microthruster vs. cold gas thruster	109
6.4	Summary And Conclusions	110
Chapter 7 Summary and Conclusions		113

LIST OF FIGURES

Figure 1-1 Cluster Configurations Analyzed	12
Figure 1-2. Satellite Cluster Formation	13
Figure 1-3. Operation of Ion Engines	14
Figure 1-4. Linear Ion Microthruster Concept	16
Figure 2-1 Cost Model Methodology	23
Figure 2-2 Cluster Configurations Analyzed.....	31
Figure 2-3 Total costs over 10 year mission life	44
Figure 3-1 Ground-based Radio Interferometer	49
Figure 3-2 Cluster Formation Normal to Reference Orbit Plane	51
Figure 3-3 Cluster Formation in Plane of Reference Orbit	51
Figure 3-4 Satellite Cluster Coordinate System.	52
Figure 3-5 Impulsive Thrusting Procedure	55
Figure 3-6 Time Until Tolerance is Exceeded	56
Figure 3-7 Propellant Savings from Impulsive Thrusting.	57
Figure 3-8 Dynamic Cluster Formation	58
Figure 3-9 Reduction in Cluster Maintenance ΔV	59
Figure 3-10 Current Thruster Capabilities	61
Figure 3-11 Feasible Isp vs. η at 1,000 km	65
Figure 3-12 Feasible Isp vs. η at 10,000 km	66
Figure 3-13 Feasible Isp vs. η at GEO	66
Figure 3-14 Thrust/mass Levels	68
Figure 3-15 Required ΔV	69
Figure 4-1 Current Balances in Ion Engines	72
Figure 4-2 Summary of Brophy's Model	83
Figure 4-3 Summary of Arakawa Algorithm	87
Figure 5-1. 7cm CSU magnetic potential contours.	93
Figure 5-2. 7cm CSU flux density contours.	94
Figure 5-3. ϵ_B vs. η_{lv}	95
Figure 5-4. Primary electron densities for 7cm chamber.	96
Figure 5-5. Plasma densities for 7cm chamber.	97
Figure 5-6. Plasma densities for 0.7cm chamber.	97
Figure 5-7. Plasma densities for 0.07cm chamber.	98
Figure 6-1. Linear Ion Microthruster	102
Figure 6-2. Sample Electron Trajectories in Linear Chamber	103
Figure 6-3. Variation of Electron Confinement Lengths with w_c/h_c	104
Figure 6-4. Linear analysis methodology.	106
Figure 6-5. Relationship between beam cost and number of chambers. .	107
Figure 6-6. Beam ion energy cost vs. chamber length	108
Figure 6-7. η vs. Isp at Several ϵ_B	109
Figure 6-8. Mission Propulsion mass (excluding thruster itself)	110

LIST OF TABLES

Table 2-1 GSFC Cost Model CLS and FAM values	25
Table 2-2 GSFC Cost Model Instrument Class and Designation	25
Table 2-3 Estimates of subsystem masses	26
Table 2-4 USAF Unmanned Spacecraft RDT&E and TFU CERs	27
Table 2-5 Launch Vehicle Costs and Capacities	28
Table 2-6 Distribution of sensors for cluster configurations	32
Table 2-7 Spacecraft mass and power characteristics	33
Table 2-8 1 sat / 1 set and 1 sat / 2 sets subsystem costs	33
Table 2-9 3 sats / 1 set subsystem costs	33
Table 2-10 Cost Model Assumptions	34
Table 2-11 Comparison with respect to Measures of Effectiveness	39
Table 3-1 Current Achievable Resolution with 10m Aperture	47
Table 3-2 Angular resolution of existing interferometers	50
Table 3-3 Baseline parameters	65
Table 3-4 Feasible Sparse Aperture Ground Resolution	68
Table 3-5 Achievable Sparse Aperture Angular Resolutions	68
Table 5-1. Scaling of 7cm CSU ion thruster ($\eta_{\text{e}}=0.7$)	96

This page intentionally left blank

Chapter 1

Introduction

1.1 BACKGROUND

This thesis addresses the issue of in-orbit propulsion for micro-satellites and distributed satellite systems from both a technical and policy perspective. The following questions will be answered:

- Are there satellite missions in which it makes sense, from a cost perspective, to distribute functionality across several smaller satellites? What preliminary design considerations should satellite manufacturers analyze to benefit from distribution?
- If a group of small satellites were to orbit in a local cluster, what are the propulsion requirements necessary to maintain that formation?
- Is it feasible to scale down a traditional ion engine so that it may be used to maintain cluster formation or as the main propulsion for a swarm of micro-satellites?

This chapter reviews work performed by others on these topics and provides background on the analysis carried out in this thesis.

1.1.1 Cost Modeling of Distributed Satellite Systems

There are currently two satellite systems operated by U.S. agencies to provide atmospheric data for weather forecasting - the DMSP system, operated by the Department of Defense, and the POES system, operated by the Department of Commerce. Both systems are approaching the end of their operational life, and

the two departments have issued a common Request for Proposal [1] for the development of the next generation weather satellite system. Its name is NPOESS (National Polar-Orbiting Operational Environmental Satellite System).

The mission of the NPOESS system is to measure and observe atmospheric and space environment data to provide accurate, reliable, and up-to-date Environmental Data Records (EDRs) to central ground stations and field users spread around the world. The NPOESS requirements specify that the instruments should fly in three sun-synchronous orbital planes with nodal crossing times of 5:30 am, 9:30 am and 1:30 pm.

The measurement of the EDRs specified in the RFP require twelve instruments on each orbital plane, three of which are considered critical. A satellite carrying a primary instrument must be, by definition, replaced if that instrument fails. Distributing the primary instruments across several smaller satellites may increase the reliability of the satellites and thus the system. This increased reliability may reduce the number of spares required thereby reducing the cost of the system. The three primary instruments and the distribution configurations examined in this thesis are shown in Figure 1-1.

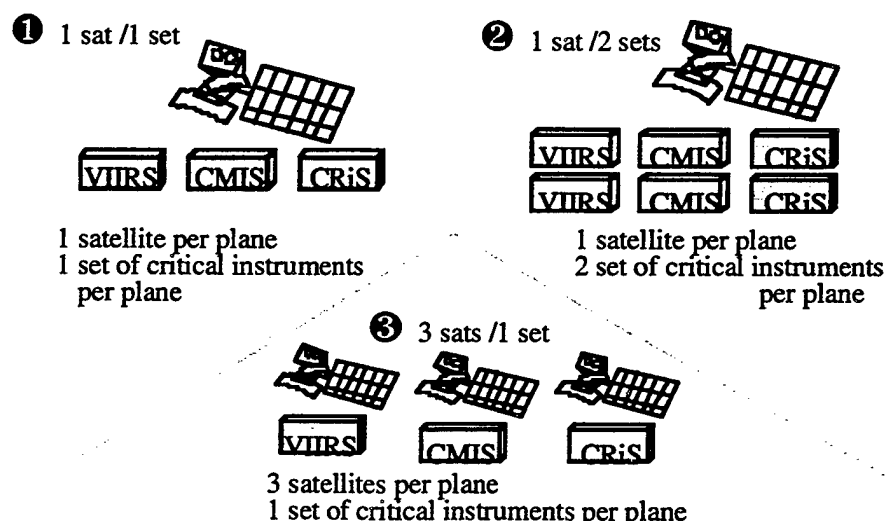


Figure 1-1 Cluster Configurations Analyzed

1.1.2 Analysis of Cluster Missions

Future satellite missions may be composed of several satellites flying in formation rather than a single larger satellite. Clusters of satellites may be employed to increase the reliability of the system, form a large sparse aperture, or simply to provide greater coverage of an area. In each case, a propulsion system will be required to maintain the formation in addition to normal station-keeping.

Jansen [2] reviewed the accelerations experienced by satellites orbiting in a formation. In particular, he examined phase control at all altitudes, creation of "designer" orbits for electrically propelled vehicles as well as formation flying of local satellite clusters. Figure 1-2 depicts a cluster of satellites forming a sparse aperture for high resolution imaging.

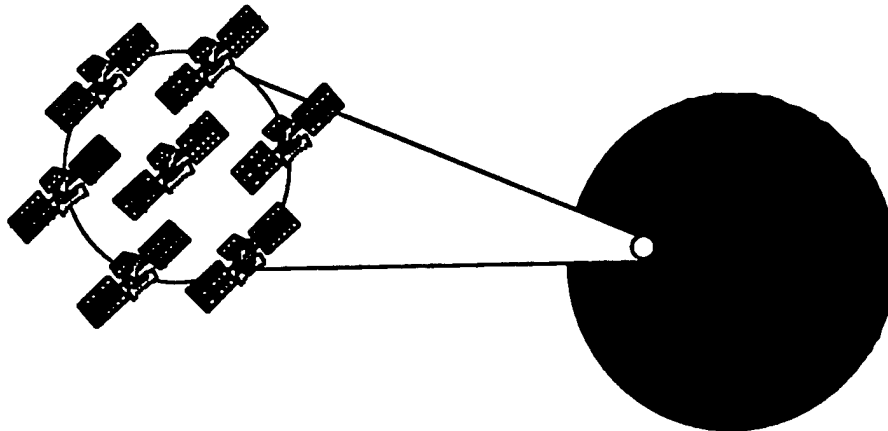


Figure 1-2. Satellite Cluster Formation

Future spacecraft may employ microthrusters for missions requiring precise, low-thrust firings. These missions may include precision station-keeping of separated spacecraft forming a large sparse aperture, control of large flexible structures such as deployable antennas or solar arrays, or as the main propulsion system for microsatellites. These missions indicate a need to greatly reduce thrust, size and power from those of current engines and associated

hardware. Additionally, new manufacturability and materials problems associated with the very small scales must be overcome.

1.1.3 Modeling Performance of Micro Ion Engines

Before detailing the models used to predict the performance of ion engines, it would be helpful to review the operation of the thruster. As shown in Figure 1-3, ion engines are cylindrical chambers with diameters typically ranging from 5 - 30 cm. Ring magnets are placed so as to create an appropriately shaped magnetic field within the chamber. A neutral gas, such as xenon, is fed into the discharge chamber. Electrons are injected from a cathode and travel within the chamber until they collide with a neutral atom to create an ion or until they reach an anode. The electrons tend to spiral around the field lines increasing the likelihood that a collision does occur. At the chamber exit, a grid system is used to set up a potential difference. Any ions in the neighborhood of the grids will be accelerated across the potential difference forming an ion beam and thus thrust. The ion beam is neutralized by an exactly opposite charge of electrons collected by the anode.

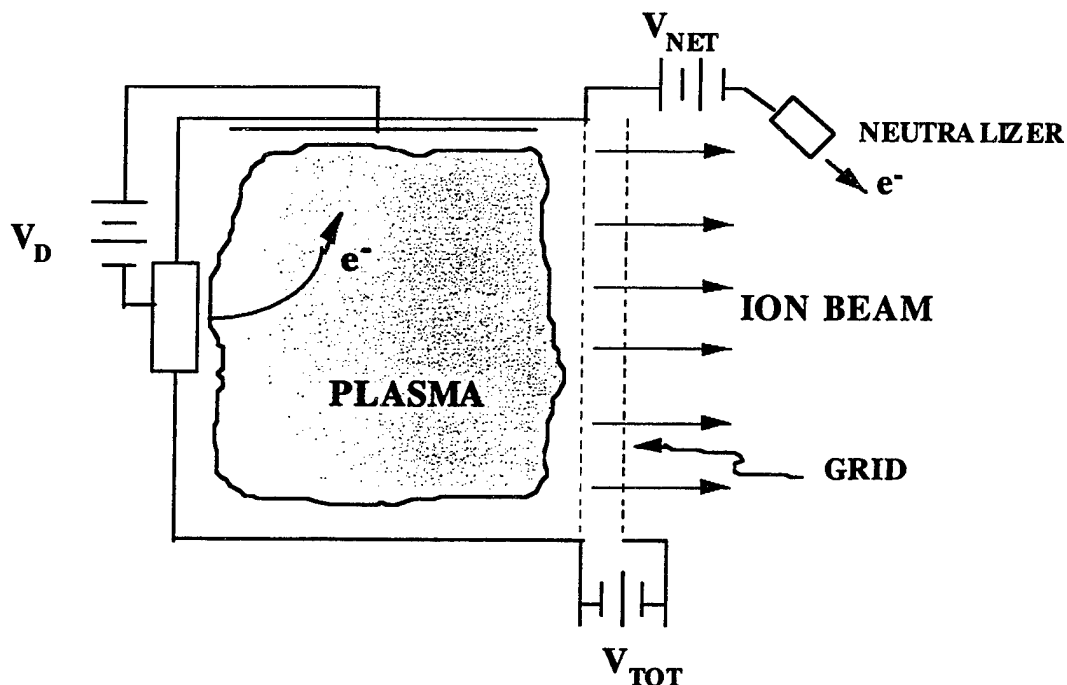


Figure 1-3. Operation of Ion Engines

Brophy and Wilbur [3] developed a model to predict the performance of ring cusp ion thrusters. The model is based on conservation of mass, charge, and energy. The result is a single algebraic equation formulated in terms of the average energy expended in producing ions in the discharge plasma and the fraction of these ions extracted in the beam. The average plasma ion energy can be found as a function of propellant utilization given geometric design parameters of the thruster and the type of propellant.

Although Brophy's model is very simple, determining the energy expended in producing ions and the fraction of these ions that reach the beam is not as simple. Arakawa [4] developed a computer algorithm to calculate those parameters. The algorithm calculates the magnetic field in the discharge chamber, follows the path of electrons along the field lines, determines the distribution of ions, and then inputs this information into Brophy's algebraic equation to determine thruster performance.

The ability to predict ion engine performance is important for two reasons. First, it allows one to examine how performance changes as the size of the chamber is scaled down several orders of magnitude. It also allows one to predict the performance of new concepts. One concept is for a micro-machined ion propulsion system put forth by members of the Jet Propulsion Laboratory [5]. The thruster, shown in Figure 1-4, consists of several linear discharge chambers situated parallel to each other. Each discharge chamber has dimensions of approximately $100\mu\text{m} \times 300\mu\text{m} \times 10\text{ cm}$. The walls separating the discharge chambers are built up from alternating layers of conducting and insulating materials. Contained within these walls is the ion accelerator system which includes the screen grid, and the ion accelerator grid.

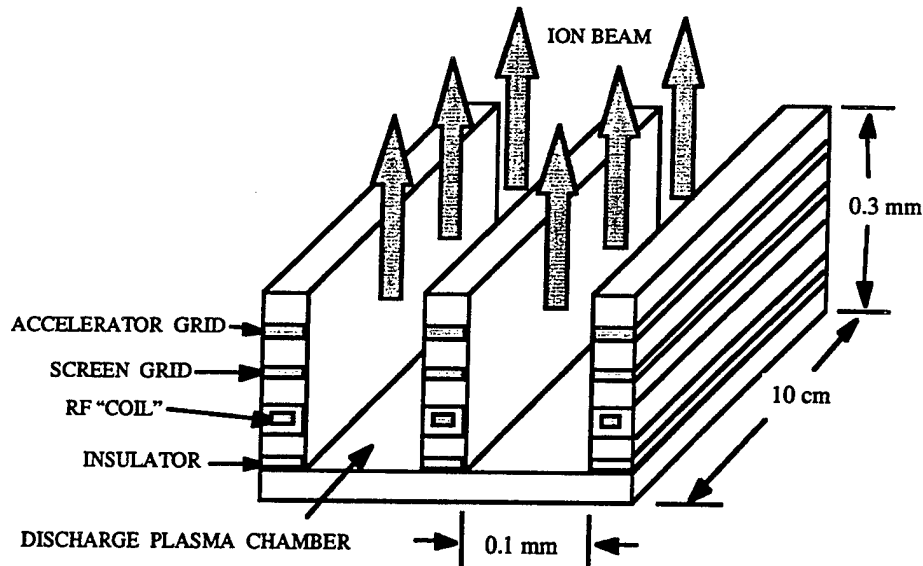


Figure 1-4. Linear Ion Microthruster Concept

1.2 PREVIEW OF CHAPTERS

- Chapter 2 - Cost and reliability models are developed to analyze the effects of distribution on the National Polar Orbiting Environmental Satellite System (NPOESS). Life cycle costs are calculated for three instrument distribution configurations. Critical technologies necessary for deploying distributed satellite systems are identified. Considerations satellite manufacturers would need to follow in preliminary design trades between traditional large satellites and distributed satellites are presented.
- Chapter 3 - An analysis of the station-keeping requirements of a distributed satellite formation known as a local cluster is carried out. First, a determination of the tolerances to which the individual spacecraft must maintain relative position is made. Next, these tolerances are related to the required thrust level, specific impulse, efficiency, etc., of the station-keeping thruster. Having examined the characteristics of thrusters required by distributed satellite systems, the rest of this thesis examines the performance of ion microthrusters.
- Chapter 4 - The derivation of the model used to predict the performance of ion thrusters is laid out. Brophy's model is derived from conservation of mass, energy, and charge principles. Fundamentals of Arakawa's algorithm, the computer code which implements Brophy's model, are described.

- Chapter 5 - Arakawa's algorithm is used to examine the effect on performance of scaling a traditional 7cm cylindrical ion engine down three orders of magnitude. Simulations with no magnetic field, a constant magnetic field, and a magnetic field varying inversely proportional with chamber size are run. Factors influencing performance as scale is reduced are identified.
- Chapter 6 - Arakawa's algorithm is modified to analyze a linear ion microthruster concept. The linear concept's design is optimized with respect to the number of chambers and chamber geometry.
- Chapter 7 - The questions addressed and answers provided by this thesis are summarized. Conclusions from both a policy and technical perspective are identified.

1.3 SUMMARY

The purpose of this chapter has been two- fold. 1) To provide an introduction to the questions addressed in this thesis and 2) to outline the procedure for how these questions will be answered. Background information on the NPOESS mission, satellite cluster propulsion requirements, and models used to predict ion engine performance was discussed. The topics of the chapters in this thesis were also previewed.

References

1. Request For Proposal #F04701-95-R-0032. NPOESS program office, Feb. 1996
2. S.W. Janson, "The On-Orbit Role of Electric Propulsion." AIAA 93-2220, 29th Joint Propulsion Conference and Exhibit, June 28-30, 1993, Monterey, CA.
3. Brophy, J.R., Wilbur, P.J., "Simple Performance Model for Ring and Line Cusp Ion Thrusters" AIAA Journal pp. 1731-1736, 23 No. 11, Nov. 1985.
4. Arakawa, Y., Ishihara, K., "A Numerical Code for Cusped Ion Thrusters." IEPC-91-118, 22nd International Electric Propulsion Conference, Oct. 14-17, 1991, Viareggio, Italy.
5. Brophy, J.R. et al. "Ion Thruster-On-A Chip for Microspacecraft" unpublished white paper. Jet Propulsion Lab. April 26, 1995.

This page intentionally left blank

Chapter 2

To Distribute or Not To Distribute: A Policy Analysis

The previous chapter provided background on the topics to be discussed in this thesis. This chapter presents a policy analysis of the NPOESS mission deployed as a distributed satellite system. A model is developed to compare the costs of deploying a satellite mission as a distributed system versus a traditional single satellite. It also details the considerations satellite manufacturers must take into account when deciding whether to deploy satellites in a distributed system. For the total design of the NPOESS mission as a distributed system, see the MIT design report [1]. A greatly extended review of tradeoffs and considerations regarding distributed satellite systems can be found in the book chapter by Shaw and Yashko [2].

2.1 INTRODUCTION TO DISTRIBUTED SYSTEMS

There are many reasons why a distributed architecture is well suited to some space applications. Unfortunately the arguments for or against distribution are fraught with subjectivity and firmly entrenched opinions. It currently seems that most of the satellite design houses in the country are internally split between the proponents and opponents of distribution. Each camp supports one side of the debate vehemently and can find a seemingly endless stream of supporting arguments to back their claims. The “radicals” claim that the development of

large constellations of small satellites leads to economies of scale in manufacture and launch, reducing the initial operating costs. They also expound that the system becomes inherently more survivable due to the in-built redundancy. Conversely, the "traditionalists" debunk these arguments, reminding everyone that you can't escape the need for power and aperture on orbit, and that building even 100 satellites does not imply significant bulk-manufacturing savings. They assert that the lifetime operating costs for large constellations will far outweigh the savings incurred during construction and launch.

In fact, most of the statements made by both sides are true, but only when taken in context. Clearly a distributed architecture is not the panacea for all space applications. It is tempting to get carried away with the wave of support that the proponents of distributed systems currently enjoy. Care must be taken to curb this blind faith. Also best avoided is the naive, but commonplace application of largely irrelevant metaphors supporting the adoption of distributed systems; the unerring truth that ants achieve remarkable success as a collective is really not an issue in satellite system engineering!

2.2 CONSIDERATIONS FOR IMPLEMENTING DISTRIBUTED SATELLITE SYSTEMS

There are some factors that are critical to the design of a distributed architecture that were irrelevant to the design of traditional systems. Depending on the application, these issues may be minor hurdles, or could be so prohibitive that the adoption of a distributed architecture is unsuitable or impossible. Some of the important considerations, characteristic of all distributed architectures, and particular to small- and microsatellite designs are presented here.

The distribution of system functionality among separate satellites means that the system is essentially transformed into a *modular* information processing

network. One beneficial aspect of modularization comes from an improved fault-tolerance. System reliability is by nature hierarchical in that the correct functioning of the total system depends on the availability of each of the subsystems and modules of which the system is composed. Early reliability studies [3] showed that the overall system reliability was increased both by applying protective redundancy at as low a level in the system hierarchy as was economically and technically feasible, and by the functional separation of subsystems into modules with well-defined interfaces at which malfunctions can be readily detected and contained. Clearly, subdividing the system into low-level redundant modules leads to a multiplication of hardware resources and associated costs. However, the impact of improved reliability over the lifetime of the system can outweigh these extra initial costs.

There are additional factors supporting modularization that are specific to satellite systems. The baseline costs associated with a system of small satellites may be smaller than for a larger satellite design. Of even greater impact is the lower replacement costs required to compensate for failure. A modular system benefits not only because a smaller replacement component has to be constructed, but also because of the huge savings in its deployment.

All of these factors suggest that a system should be separated into modules that are as small as possible. However, there are some distinct disadvantages of low-level modularization that must be considered. The most important of these are the costs and low reliability associated with complexity.

2.2.1 Complexity

The complexity of a system is well-understood to drive the development costs and can significantly impact system reliability. In many cases, complexity leads to poor reliability as a direct result of the increased difficulty of system analyses; failure modes were missed or unappreciated during the design process. For a

system with a high degree of modularity, these problems can offset all of benefits discussed above.

Although each satellite in a distributed system might be less complex, being smaller and having lower functionality, the overall complexity of the system is greatly increased. The actual level of complexity exhibited by a system is difficult to quantify. Generally, however, it is accepted that the complexity is directly related to the number of interfaces between the components of the system. Although the actual number of interfaces in any system is architecture specific, it is certainly true that a distributed system of many satellites has more interfaces than a single satellite design. Network connectivity constraints mean that the number of interfaces can increase geometrically with the number of satellites in a distributed architecture. This is an upper bound; systems featuring satellites operating in parallel with no inter-satellite communication (defined as collaborative systems) exhibit linear increases in interfaces with satellites. The complexity of a distributed system is therefore very sensitive to the number and connectivity of the separate modules.

2.3 MODELING DISTRIBUTED SATELLITE SYSTEMS

In 1996, a request for proposals (RFP) was issued for the next generation National Polar Orbiting Environmental Satellite System (NPOESS) [4]. This provided an opportunity to examine the merits of deploying NPOESS with functionality distributed across several smaller satellites. The nodal crossing time requirements of the RFP dictate that the NPOESS space segment consist of three orbital planes. There is no a priori reason, other than co-registration requirements, that all sensors in the plane must be located on a single satellite. In fact, locating all sensors on a single satellite reduces the reliability of the satellite since failure of any of the several primary sensors would require replacement of the entire satellite. It may be possible then, to increase the reliability and reduce the lifetime cost of the NPOESS space segment by

distributing the sensors across several smaller satellites orbiting as a cluster. This chapter describes the model developed to examine several candidate cluster configurations to determine the effect that distributing the primary sensors has on total lifetime costs.

2.3.1 Model Overview

The methodology of the reliability / cost model is shown in Figure 2-1. The number of satellites in each plane along with the types of sensors on each satellite are chosen as primary inputs to the model. In addition, the bus design life, bus reliability, sensor reliability, mission life, learning curve percent, and a term known as the level of similarity (LOS) must be included. For configurations where instruments are distributed across several spacecraft, the buses would be similar but not identical. The level of similarity, ranging from 0 to 1, is a measure of how similar the buses are so that costs may be shared where appropriate. Probability of bus failure is assumed to be 100% at the end of the bus design life due to exhaustion of expendables, failure of batteries, or insufficient power due to solar array degradation.

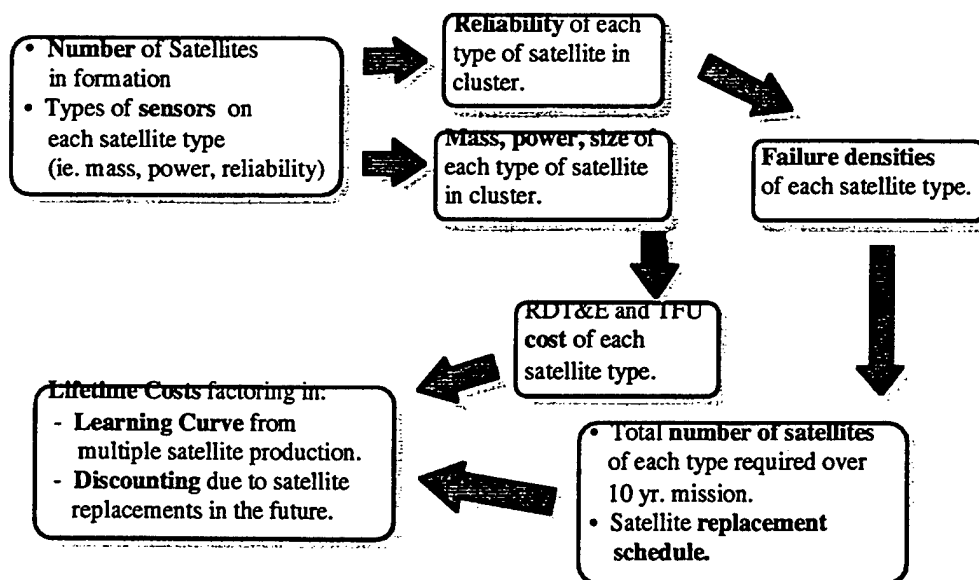


Figure 2-1 Cost Model Methodology

Bus subsystem characteristics are estimated from payload mass and power using estimates based on a regression of data from 15 previous Department of Defense communication, navigation, and remote sensing missions. With the bus and payload information, the reliability of each spacecraft type can be calculated. Failure rates, and therefore an expected deployment schedule, for each satellite type follow from the spacecraft reliability. Parametric costs models can then be used to estimate the cost of the sensors and the spacecraft bus based upon the estimated subsystem mass and power requirements. Knowing the number of satellites deployed and their expected launch date, the total cost over the system's mission life can be calculated factoring in learning curve effects and discounting to current year dollars. The details of this model are described in subsequent sections of this chapter.

2.3.2 Payload Cost Model

An estimate of the cost of each sensor was calculated using the Goddard Space Flight Center (GSFC) Multi-Variable Instrument Cost Model. The GSFC instrument cost model generates a cost estimate to develop and produce the first unit from a regression of sensor type, mass, power and data rate for 186 existing instruments. An additional factor is included to account for the level of technology in the year the instrument was developed. The cost to procure the sensor is assumed to be 50% of the prototype cost. The parametric relationship used to estimate the prototype cost of the instrument (FY97\$M) is

$$COST = 0.576 \left((0.453 MASS)^{0.421} \right) \left(PWR^{0.177} \right) \left((YR - 1960)^{-0.113} \right) \left(DRT^{0.048} \right) \left(FAM^{1.028} \right) \left(CLS^{0.928} \right) \quad (2-1)$$

where MASS= instrument mass (kg)
PWR = instrument power (W)
DRT = instrument data rate (kbps)
YR = year launched
FAM = mission family
CLS = instrument class

Valid ranges for instrument mass, power, data rate and launch year are 2.2 to 6847.5 kg, 0.6 to 2000 W, 0.008 to 85000 kbps, and 1965 to 1989 respectively.

In general, it is not advisable to extrapolate more than 25% beyond a parameter's range [5]. It should be mentioned that the NPOESS sensors, which were assumed to consist of 1997 technology, represent an extrapolation of 29% beyond the range. Values for the instrument class, CLS, and mission family, FAM, are listed in Table 2-1. All sensors used onboard NPOESS satellites were assigned a Mission Family designation of "Normal (Earth resource sat)". Table 2-2 lists the Instrument Class and designation of each of the sensors. For suites consisting of sensors belonging to more than one instrument class, an average CLS value was used. GPSOS and S&R, which do not specifically belong to one of the GFSC model instrument classes were assigned to an RF class with a CLS value of 1.

Table 2-1 GSFC Cost Model CLS and FAM values

Instrument Class	CLS	Mission Family	FAM
Plasma Probe	1.030	Shuttle	0.440
Magnetometer	1.065	Explorer (Small Free Flier)	1.125
Passive Microwave	1.182	Normal (Earth resource sat)	1.720
Spectrometer	1.221	Planetary	2.282
Mass Measurement	1.270	Manned (non-shuttle)	2.380
Electric Field	1.290		
Active Microwave	1.291		
Interferometer	1.309		
Charge Detection	1.317		
Photometer	1.490		
Laser	1.630		
Radiometer	1.645		
Telescope	2.300		
High Res. Mapper	4.890		

Table 2-2 GSFC Cost Model Instrument Class and Designation

Sensor Name	Instrument Class	Designation
VIIRS	High Resolution Mapper, Radiometer	primary
CRIS	Radiometer	primary
CMIS	Passive Microwave, Active Microwave	primary
GPSOS	RF	secondary
S&R	RF	secondary
SOBEDS	Magnetometer, Plasma Probe, Charge detector	secondary
NCERES	Radiometer	secondary
TOMS	Spectrometer	secondary
Altimeter	Radiometer	secondary
DIDM	Electric Field Measurement, Mass Measurement, Charge Detector	secondary

NACRIM	Radiometer	secondary
ABIS	Radiometer	secondary
SUVPHO	Photometer	secondary
ARGOS	Radiometer	secondary

2.3.3 Satellite Bus Cost Model

Space segment costs were estimated using the U.S. Air Force (USAF) Unmanned Spacecraft Cost Model v5 [6]. This model utilizes parametric cost estimating relationships (CER) derived from past satellite programs based on major subsystem characteristics such as mass, power, and data rate. These subsystem parameters were estimated using average values, listed in Table 2-3, of 15 previous Department of Defense communications, navigation, and remote sensing satellite missions. Payload mass and power are known given the sensors required to measure the environmental data records. The dry mass of the spacecraft bus along with the individual subsystem masses can then be estimated.

Table 2-3 Estimates of subsystem masses

Subsystem	% of spacecraft dry mass
Payload	28.0
Structures	21.0
Thermal	4.5
Power	30.0
Telem, Tracking, Control	4.5
Attitude Control	6.0
Propulsion	6.0

In addition, the average spacecraft power and required array power can be estimated from the total payload power (Watts) as follows.

$$P_{avg} = \frac{P_{payload}}{0.3} \quad (2-2)$$

$$P_{array} = 1.33P_{avg} \quad (2-3)$$

The subsystems' mass and power can be used to estimate the subsystems' research, development, test and evaluation (RDT&E) and theoretical first unit (TFU) cost according to the CER's shown in Table 2-4.

Table 2-4 USAF Unmanned Spacecraft RDT&E and TFU CERs

Cost Component	Parameter, X	Applicable Range	RDT&E CER (FY97\$k)	TFU CER (FY97\$k)
Structure/Thermal	Mass (kg)	7 - 428	$3102 + 488.8X^{0.66}$	$0.0 + 101X^{0.65}$
TT&C	Mass (kg)	4 - 112	$2297 + 234X$	$109 + 193X^{0.93}$
Attitude & Reaction Control	Dry Mass (kg)	25 - 170	$1099 + 3913X$	$-428 + 219X^{0.73}$
Power *	EPS Mass x BOL Pwr (kgW)		$2734 + 0.0417X$	$1985 + 0.0213X$
Software	kLOC	N/A	$664 \times \text{kLOC}$	N/A
Aerospace Ground Equipment	RDT&E + TFU Hardware Costs (\$k)	23531 - 285576	$0.0 + 0.13X$	N/A
Program Level	Satellite Hardware Cost (\$k)	34012 - 267347	$0.0 + 0.36X$	$0.0 + 0.39X$
Launch Ops & Orbital Support	Wet Mass (kg)	210 - 1345	N/A	$0.0 + 2.95X$

* from USAF Unmanned Spacecraft Cost Model v.6

The space segment was assumed to have a minimum impact on existing ground stations regardless of the number of satellites in the configuration. Communications subsystems and satellite configuration were designed to accommodate existing ground stations and field user capabilities. Major ground stations should need to utilize two or three of their existing antennas to communicate with the space segment. Moreover, the duration of satellite data transmission should not excessively burden ground stations. The deployed field users require only a single standard issue antenna for any of the proposed configurations. Based upon these assumptions and because costs vary widely, the cost of ground stations was not considered in the configuration trade.

The cost to launch each satellite was determined by examining the vehicles capable of being launched from Vandenberg Air Force Base (VAFB) listed in Table 2-5. The wet masses of the satellites were compared to the launch capacities of the available vehicles. For the scenario in which each plane contains a cluster of more than one satellite type, as many satellites as possible

were placed on a launch vehicle during initial deployment of the system. It must be kept in mind that the final launch into a plane may not need to carry as many satellites as the previous launches. For example, if a plane contains a cluster of three small satellites and the launch vehicle is capable of carrying two satellites at once, then the second launch of the initial deployment into that plane would carry only one satellite. Thus, the final initial deployment launch into a plane and any launch to replace a failed satellite may occur on a different launch vehicle. The chosen launch vehicle is the one that minimizes launch costs given the wet masses of the satellites.

Table 2-5 Launch Vehicle Costs and Capacities

Launch Vehicle	Capacity to SSPO (kg)	Cost / Launch (97 M\$)
LMLV II	1210	21
Taurus XL	1150	38
Titan II S	3028	36
Delta II 7925	3175	60
Titan IV	13364	300

2.3.4 Similarity Factor

The RDT&E cost for each satellite type can be calculated using the USAF unmanned spacecraft cost model described in Section B-2. In the case where there is more than one satellite type, a separate RDT&E cost would be calculated for each type. Because there are some similarities between the buses, each satellite type would not have to bear the full development cost of a stand alone program. The level of similarity, LOS, ranging from 0 to 1 indicates the commonality among the different bus types. A LOS equal to 1 represents identical buses. A LOS equal to 0 indicates that no RDT&E costs are shared among the different bus types. A similarity factor, SF, by which the stand-alone RDT&E cost of satellite bus type *b* is multiplied to reflect its true RDT&E cost in conjunction with other similar buses under development, is given by:

$$SF_b = 1 - \left[1 - \frac{RDTE_{avg}}{(RDTE_b)(numbus)} \right] LOS \quad (2-4)$$

where numbus= number of different bus types

$RDTE_{avg}$ = average stand-alone RDT&E cost of all bus types

$RDTE_b$ = stand-alone RDT&E cost of bus type b

2.3.5 Learning Curve And Discounting

Two additional considerations must be taken into account when determining the costs over the system's life. The learning curve is a method to account for the productivity improvements as a larger number of satellites are produced. Included in this concept are cost reductions due to economies of scale, set-up time, and human learning as the number of satellites produced increases. The cost to produce the next unit of satellite type b is given by

$$p \text{ cost}_b = TFU_b [N_b + (N_{tot} - N_b)LOS]^D - TFU_b [(N_b - 1) + (N_{tot} - N_b)LOS]^D \quad (2-5)$$

where N_b = number of satellite bus type b produced including current unit

N_{tot} = total number of all bus types produced including current unit

$$D = 1 - \frac{\ln(100\% / S)}{\ln 2}$$

S = slope of the learning curve (%)

TFU = theoretical first unit cost

The LOS term is included to allow for reductions in the production cost of a bus type due to the production of other similar, yet not identical, bus types. The learning curve slope, S , represents the percentage reduction in cumulative average production cost when the number of satellites produced is doubled. A 95% learning curve slope was applied to production of satellite buses. When calculating the expected replacement costs, the next unit is represented by the probability of needing to build a satellite bus in order to maintain required number of spares.

The year each satellite is launched can be determined from the deployment schedule discussed in the next section. The production cost of each satellite is assumed to be distributed over a three year period prior to the launch date. 20%

of the cost is incurred two years before launch, 30% is incurred the year before, and 50% is incurred during the year of the launch [7]. Furthermore, the cost is discounted to constant 1997 dollars by multiplying the cost in each year by the factor

$$PV = \frac{1}{(1+d)^{n-1}} \quad (2-6)$$

where n = the year the cost is incurred (relative to the constant dollar year)
 d = discount rate

2.3.6 Replacement Model

The failure of the spacecraft, and therefore its replacement schedule, is a function of the reliability of the spacecraft. Because a spacecraft must be replaced if any of its primary instruments fail, this model assumes that the reliability of the spacecraft is related to the reliability of the bus and primary sensors as follows:

$$R_{s/c} = R_{bus} \left[\prod_{i=1}^{types} 1 - (1 - R_i)^{N_i} \right] \quad (2-7)$$

where $R_{s/c}$ = reliability of spacecraft
 R_{bus} = reliability of bus
 R_i = reliability of primary instrument i
 N_i = number of primary instruments of type i on spacecraft
 $types$ = number of different types of primary instruments on spacecraft

It is required that a 99% confidence of achieving 95% availability be met. A Monte Carlo simulation of the mission was used to calculate failure densities at a given time. These failure densities are then used to determine the number of spares required to meet the confidence and availability requirements. For example, if the probability of three satellites failing in the time it would take to build another satellite was greater than 1%, then three spares would be required.

2.4 RESULTS OF CLUSTER CONFIGURATION ANALYSIS

The reliability/cost model is used to determine satellite configurations which best meet the measures of effectiveness. Figure 2-2 shows the three candidate cluster configurations that were analyzed. Three primary instruments, VIIRS, CMIS, and CrIS, are required for the mission. Details of these instruments are discussed in reference 1. Two cluster configurations examined consisted of the three instruments placed either all on a single satellite (configuration 1) or each on one of three smaller satellites (configuration 3). Another configuration, in which an additional primary sensor is added to the single satellite for redundancy (configuration 2), was also examined.

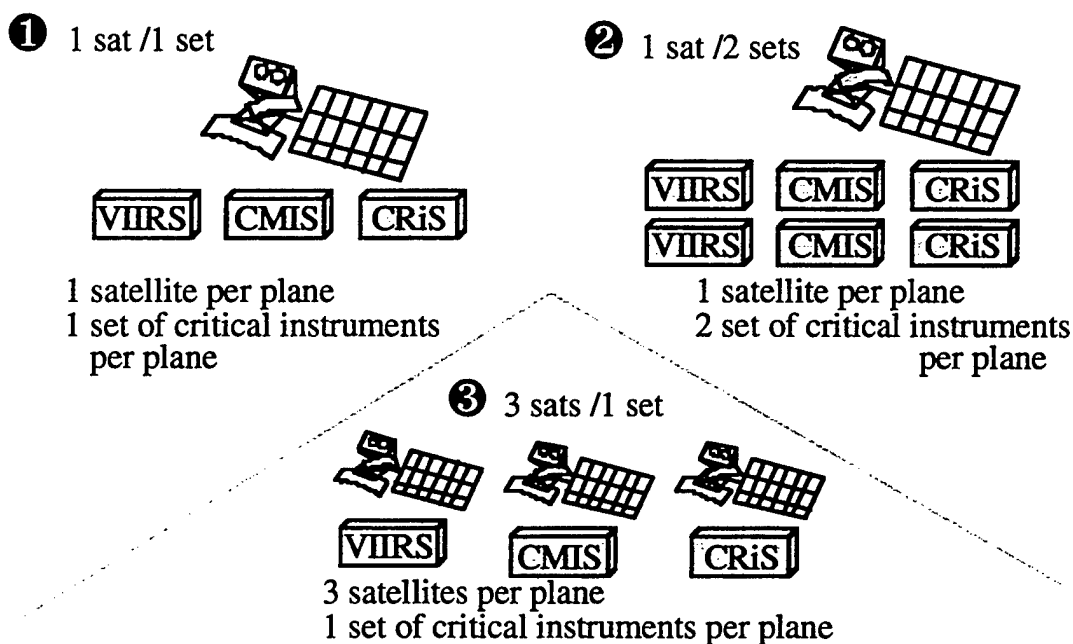


Figure 2-2 Cluster Configurations Analyzed

For configurations consisting of more than one satellite, the secondary instruments were distributed among the satellites in such a way as to balance payload mass and power requirements. This implies a fairly standard design and a high level of similarity amongst the buses. Table 2-6 lists the sensors

along with their respective mass, power and cost characteristics for each configuration shown in Figure 2-2.

2.4.1 Cost Breakdown for Cluster Configurations

Using these payload values, the spacecraft mass and power characteristics can be found using the relationships described in Table 2-3 and Equations (2-2) through (2-3). These spacecraft mass and power values are listed in Table 2-7 for each configuration.

Table 2-8 and Table 2-9 list the subsystem costs for the 1 sat / 1 set, 1 sat / 2 set and 3 sats / 1 set configurations. These values were estimated using the CER's in Table 2-4. The total RDT&E cost for the 3 sats / 1 set configuration must be multiplied by the similarity factor as calculated by equation (2-4).

Table 2-6 Distribution of sensors for cluster configurations

Sensor Name	Mass (kg)	Power (W)	Cost (\$M)	1 sat / 1 set	1 sat / 2 set	3 sats / 1 set		
						sat 1	sat 2	sat 3
VIIRS	132	215	22.4	✓	✓✓	✓		
CMIS	178	208	8.7	✓	✓✓		✓	
CrIS	68	82	7.1	✓	✓✓			✓
GPSOS	9	13	1.2	✓	✓	✓	✓	✓
S&R	82	88.8	3.5	✓	✓	✓		
SOBEDS	5	5.6	1.1	✓	✓	✓	✓	✓
NCERES	40	35	3.8	✓	✓	✓		
TOMS	33	25	2.9	✓	✓			✓
Altimeter	53	113	5.3	✓	✓			✓
NACRIM	39	35	3.4	✓	✓			✓
ABIS	15	7	1.8	✓	✓			✓
SUVPHO	8	10	1.4	✓	✓			✓
ARGOS	71	62.4	5.0	✓	✓		✓	
Payload Mass (kg)				733	1110	268	263	230
Payload Power (W)				900	900	358	289	290
Payload Cost (FY97\$M)				68	106	32	16	24

Table 2-7 Spacecraft mass and power characteristics

Characteristic	1 sat / 1 set	1 sat / 2 sets	3 sats / 1 set		
			sat 1	sat 2	sat 3
Dry mass (kg)	2617	3967	955	940	821
Wet mass (kg)	2647	3997	985	970	851
Avg. Power (W)	2999	2999	1191	963	969
Peak Power (W)	3989	3989	1584	1281	1288
BOL Power (W)	5186	5186	2060	1666	1675

Table 2-8 1 sat / 1 set and 1 sat / 2 sets subsystem costs

Configuration Cost Component	1 sat / 1 set		1 sat / 2 sets	
	RDT&E (FY97\$M)	TFU (FY97\$M)	RDT&E (FY97\$M)	TFU (FY97\$M)
Payload	N/A	68	N/A	105.9
Structure/Thermal	38.8	6.9	50.1	9.1
TT&C	29.8	16.4	44.0	24.0
Attitude Determ.	40.1	10.5	48.5	12.4
Reaction Control	29.3	8.3	43.9	11.4
Power	25.8	21.3	33.4	31.3
Software	4.4	N/A	4.4	N/A
Aeros Gmd Equip	38.1	N/A	53.5	N/A
Program Level	69.3	50.8	93.1	75.3
Launch Ops & Orbital Support	N/A	4.6	N/A	6.8

Table 2-9 3 sats / 1 set subsystem costs
(RDT&E costs must be multiplied by similarity factor)

Cost Component	Satellite 1		Satellite 2		Satellite 3	
	RDT&E (FY97\$M)	TFU (FY97\$M)	RDT&E (FY97\$M)	TFU (FY97\$M)	RDT&E (FY97\$M)	TFU (FY97\$M)
Payload	N/A	32.0	N/A	16.0	N/A	24.2
Structure/Thermal	21.5	3.6	21.3	3.6	19.7	3.3
TT&C	12.3	6.5	12.2	6.4	10.9	5.6
Attitude Determination	25.2	7.1	25.0	7.0	23.5	6.7
Reaction Control	11.4	3.8	11.2	3.7	10.0	3.3
Power*	15.8	8.2	14.8	6.9	14.3	6.3
Software	4.4	N/A	4.4	N/A	4.4	N/A
Aerospace Ground Equipment	19.1	N/A	19.1	N/A	19.1	N/A
Program Level	36.5	23.7	35.7	16.9	33.2	18.3
Launch Ops & Orbital Support	N/A	1.7	N/A	1.7	N/A	1.5

Table 2-10 lists important assumptions inputted to the reliability/cost model.

Table 2-10 Cost Model Assumptions

Sensor Reliability	0.86 over 7 years
Mission Life	10 years
Bus Reliability	0.90
Launch Vehicle Reliability	0.98
Bus Level of Similarity (LOS)	0.66
Discount Rate	6%
Year of Initial Deployment	2004

2.4.2 Total Mission Costs

The total costs over a 10 year mission life were calculated for each of the three cluster configurations. As shown in Figure 2-3, the costs over the 10 year period are broken up into four categories; namely RDT&E, initial deployment, required spares, and expected replacements. RDT&E cost for the 3 sats / 1 set configuration are those listed in Table 2-9 multiplied by the similarity factor. Initial deployment includes the development, production, and launch costs for each orbital plane's original complement of spacecraft. The number of required bus, payload, and launch vehicle spares is derived from the operations model so as to meet required mission availability (95%) with the desired confidence (99%). Expected replacements also flow from the operations model and indicate the number of bus, payload, and launch vehicle units which must be produced during the mission to maintain the required number of spares.

Figure 2-3 shows that the initial deployment cost is least expensive for the 1 sat / 1 set configuration. Adding a redundant sensor to the single satellite configuration greatly increases initial deployment cost in terms of larger bus size, additional instruments, and more expensive launch vehicles. The 3 sat / 1 set configuration, although being launched on a less expensive vehicle, is slightly more expensive than the 1 sat / 1 set configuration due to the duplication of bus subsystems (e.g. power, attitude control, propulsion etc.) and some sensors (e.g. GPSOS) in each orbital plane.

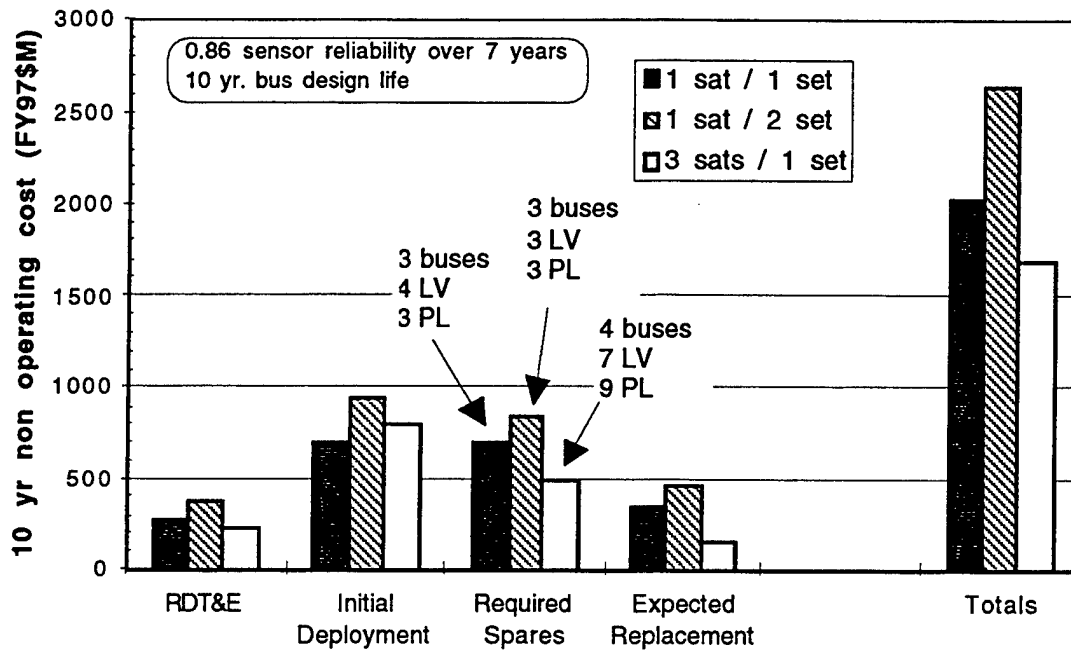


Figure 2-3 Total costs over 10 year mission life

Figure 2-3 also shows that adding a redundant sensor increases the cost as compared to configurations with a single primary instrument. The slight decrease in the failure densities as a result of redundancy does not make up for the expense of additional sensors. It is assumed that periods of one year and two years are necessary to produce a new spacecraft and to procure a new launch vehicle respectively. For the 1 sat / 1 set configuration, there is a 2.9% probability of three failures occurring within one year of each other. Thus three spares and three sets of instruments are required at the beginning of the mission to ensure achievement of mission availability requirements with 99% confidence. Adding redundant instruments to the single satellite lowers this probability of three failures within the year to 1.1%. Therefore the 1 sat / 2 set configuration also requires three spare spacecraft at the beginning of the mission.

Only three launch vehicle spares are required for the 1 sat / 2 set configuration since the probability of four failures within the two years necessary to procure a new launch vehicle drops below 1% with the addition of redundant sensors. The cost savings from needing one less spare launch vehicle is not enough to offset the additional cost of the redundant sensors.

With a full on-orbit complement of nine smaller satellites, the 3 sat / 1 set configuration requires only four spare buses and three spare sets of instruments. This results in a large decrease in the cost of the spacecraft spares as compared to the single satellites configurations. Because there are nine satellites, seven launch vehicle spares must be available to ensure confidence of achieving mission availability. These launch vehicles, LMLV IIs, cost \$21 million compared with the \$60 million cost to procure spare Delta IIs for the single satellite configuration. Overall , the cost to provide necessary spares is lowest for the 3 sat / 1 set configuration.

Distributing the primary instruments among three satellites significantly increases the reliability of each individual satellite. While this effect was apparent in the number of spares required it also influences the cost of expected replacements procured during the mission life. Higher satellite reliability and lower launch costs to replace the satellites that do fail results in the 3 sat / 1 set configuration having the lowest expected replacement cost. Once again the slight increase in reliability gained from adding redundant primary instruments for the 3 sat / 2 set configuration is outweighed by the higher bus, payload, and, launch costs.

The combined effect of these three categories of cost is shown by the total ten year non-operations costs data in Figure 2-3. The 3 sat / 1 set configuration appears less expensive than the 1 sat / 1 set configuration.

Figure 2-4 displays the same data as in Figure 2-3 although broken down into RDT&E, payload, bus, and launch costs, expended during the 10 year mission.

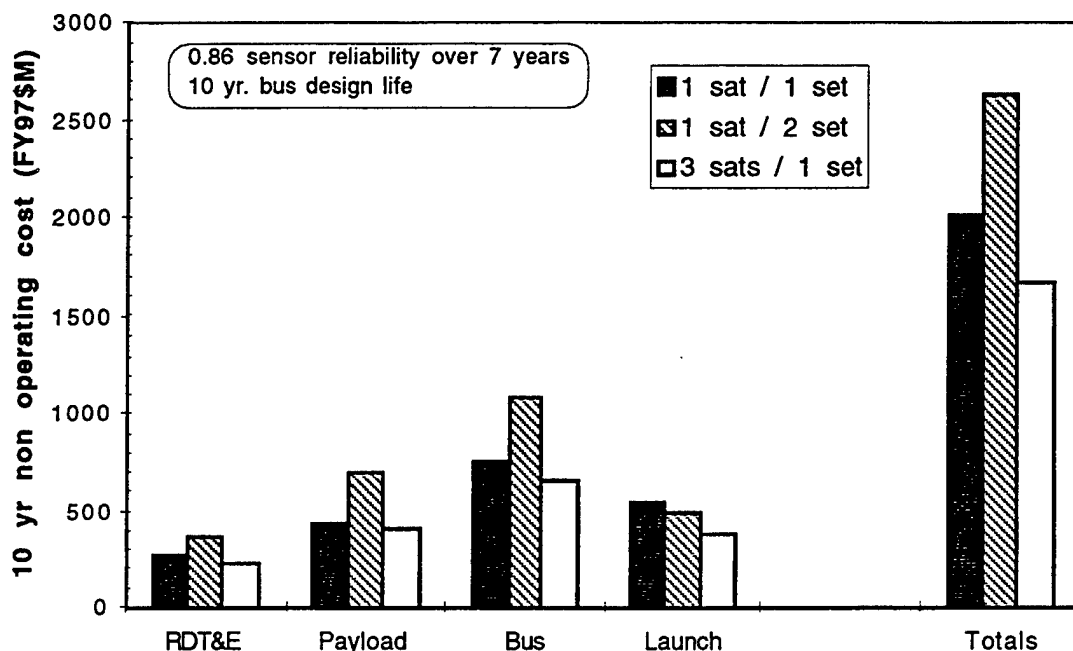


Figure 2-4 Breakdown of costs over 10 year mission life

2.4.3 Sensitivity of Costs to Instrument Reliability

The sensitivity of the 10 year mission cost to sensor reliability also indicates the best choice. The previous analysis assumed a sensor reliability of 0.86 over 7 years. If, however, the reliability of the sensors were to fall short of the stated goal; for example 0.70 over seven years, the 10 year mission cost for the 3 sat / 1 set and 1 sat / 1 set configurations would be as shown in Figure 2-5. Because the primary instruments are distributed across three satellites, a decrease in their reliability results in only a relatively small increase in cost for the 3 sat / 1 set configuration. Because all of the primary sensors are on a single satellite in the 1 sat / 1 set configuration, a decrease in sensor reliability significantly reduces the overall reliability of that satellite leading to a jump of over \$500 million in the 10 year mission cost. The more prudent choice to hedge against

the risk of a large cost increase due to lower than expected sensor reliability is the 3 sat / 1 set configuration.

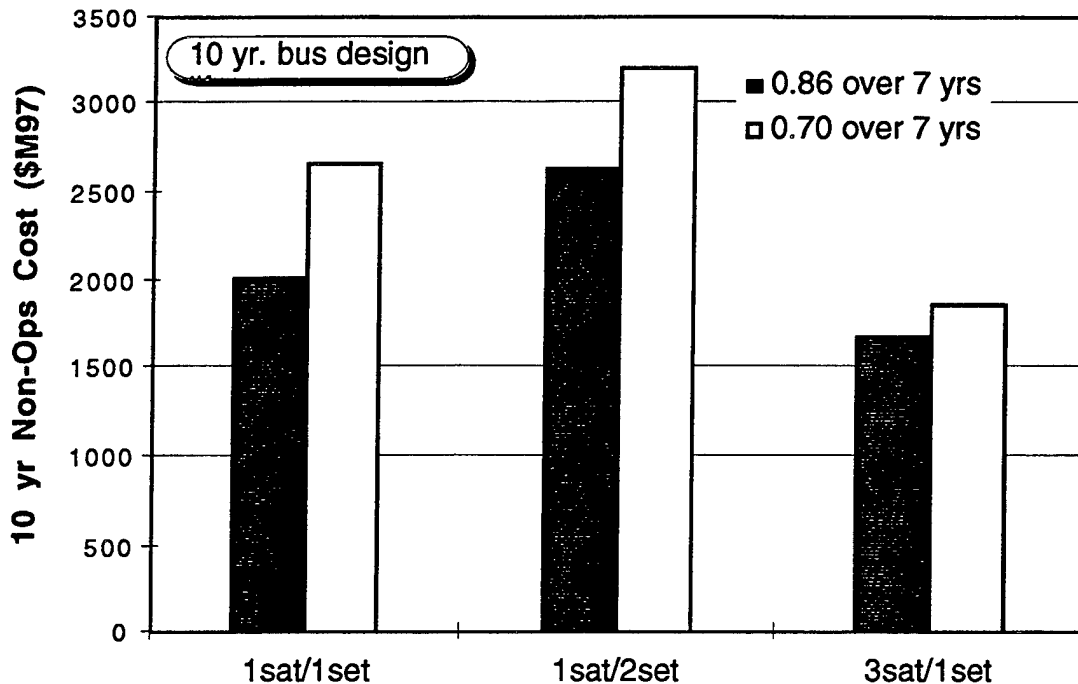


Figure 2-5 10 year mission cost versus sensor reliability

Distribution of sensors among several satellites is appropriate when the savings from increased reliability outweigh the increased cost to deploy the distributed system. For satellites designed to a short life (e.g. 3 years), it is more likely that the bus will reach the end of its propellant supply or battery life than for a sensor to fail. Thus, any gains in reliability from distribution are irrelevant and the distributed system costs more over the mission life. Further, distribution is less advantageous for systems with high sensor reliability. As sensor reliability increases, the overall reliability of the 1 sat / 1 set configuration quickly approaches that of the 3 sat / 1 set configuration. The high initial deployment costs of the 3 sat / 1 set configuration can no longer be justified when replacement costs for the 1 sat / 1 set configuration are on par with those of the 3 sat / 1 set configuration.

It should be mentioned that no attempt was made to account for a decrease in the procurement cost for lower reliability sensors. Figure 2-5 indicates that only a small increase in the 3 sat / 1 set mission cost takes place when sensors having a reliability of 0.7 over 7 years are used. Had the decrease in sensor procurement cost also been factored in, this small increase may have been further reduced.

Table 2-11 summarizes the four candidate cluster configurations' influence on the measures of effectiveness. Each of the four configurations provide an opportunity for the system to measure required environmental data with necessary co-registration requirements. Because increased schedule risk is due primarily to the use of unproven technologies, the choice of how the sensors are distributed neither significantly increases nor decreases the risk of the schedule slipping. The configurations with the redundant set of instruments were shown to greatly increase cost while minimum cost was achieved by the configurations with only a single set of instruments. Only the 3 sats / 1 set configuration, however, protects against a large increase in cost due to lower than expected sensor reliability.

Table 2-11 Comparison with respect to Measures of Effectiveness

	Weight Factor	1 Sat 1 Set	1 Sat 2 Sets	3 Sats 1 Set
Minimize Cost	4	*	*	✓
Minimize Cost Risk	3	*	✓	✓
Minimize Schedule Risk	1	•	•	•
Provide Opportunity To Meet Schedule Reqs.	8	✓	✓	✓

• - Neutral ✓ - Allows MOE * - Prevents MOE

2.5 OTHER IMPLEMENTATION CONSIDERATIONS

Current levels of automation in satellite systems reflect an incremental evolution that is based on a high level of human involvement. Historically, this has been a result of the desire to reduce risk and due to limited technological capabilities. Due to the dependence on humans to perform tasks, operations costs can make

up a significant portion of the life cycle costs for a satellite system [8]. In addition, human error continues to be a major cause of spacecraft anomalies and failures. With the introduction of large constellations or clusters of satellites, some automation of operations will be required to reduce costs while maintaining availability (the probability of meeting system requirements at a given time) [9], [10], [11]. Despite recognition of the need, there is reluctance to automate. The large investments and high risks involved in space ventures has lead to a conservative industry. In addition, the desire to reduce cycle times for new programs also favors significant re-use of proven technologies and thus, low levels of automation.

Figure 2-6 qualitatively represents the cost and availability characteristics of a hypothetical satellite system with respect to an increasing level of automation. As low levels of automation are introduced into the system, the operating costs decrease, principally due to a decrease in the number of human operators (Figure 2-6A). At some point, however, the increases in design and development costs due to software development outweigh the decrease in operation costs.

As shown in Figure 2-6B, availability may decrease, increase, or be unaffected by the level of automation. For tasks that are simple, well understood, or periodic (such as routine station-keeping on a geostationary satellite), availability may increase with increasing automation (Task A). This is true in the cases when human errors are more likely than software errors, or when the impact of unanticipated situations is negligible. For complex, rare, or unexpected functions, availability may decrease as humans are removed from the loop (Task C). This can occur when the automation is unable to resolve problems that could have been resolved by a human or when the automation fails to accurately inform the human of the situation. There may be some

functions for which the availability is nearly independent of the level of automation (Task B).

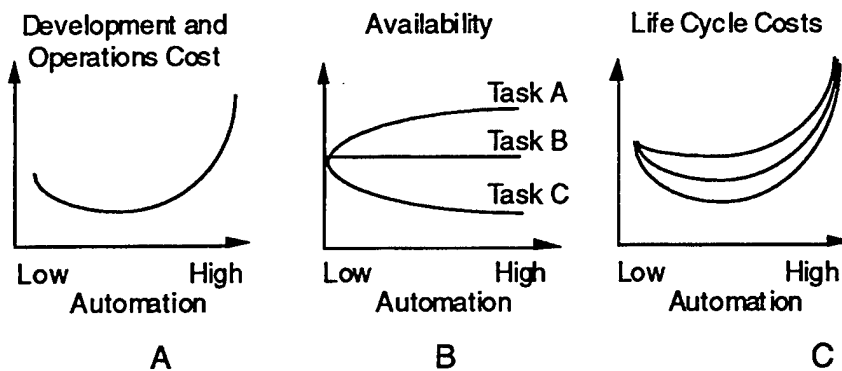


Figure 2-6: Effect of Automation on Cost and Availability

An increase in system availability translates into an increase in revenues for a commercial system, or an increased ability to perform an objective for science or military systems. Thus, the potential for failure can be represented by an opportunity cost which represents revenues forgone as a result of increased system down-time. For commercial systems, the opportunity cost can be added to the development and operations costs to form the life cycle cost. Determination of opportunity costs requires additional data such as the relationship between a particular function and revenue. For science or military applications, the definition of an opportunity cost may be difficult. In such cases, the development and operations cost would be compared against the availability without attempting to define the life cycle cost. The combination of the two curves Figure 2-6A and Figure 2-6B are represented in Figure 2-6C, showing the overall life cycle cost which is defined as the sum of development, operations, and opportunity costs.

In the example of Figure 2-6, there exists an optimum level of automation at which life cycle cost is minimized. Due to the complexity of the satellite system, a methodology is needed that can model the effect that automation has on costs and system availability. Such tools would enable system engineers to identify those functions that should be automated.

Constellations of satellites introduce a twist in the automation trade since automation is usually associated with high non-recurring costs. As the level of automation increases, operations costs are expected to decrease, and development costs are expected to increase. As the number of satellites increases for a given level of automation, the operations costs will increase linearly. Development costs, however, will lag a linear relationship due in part to a learning curve, and in part to the much lower recurring costs of automation relative to the non-recurring cost. Thus, functions which are not suitable for automation for a single satellite may be desirable for a constellation. In fact, crossover points can be identified which define constellation sizes over which certain levels of automation are optimal.

Constellations of microsatellites will likely contain a very large number of satellites in order to perform a useful mission. As discussed above, for a given level of automation, as the constellation size increases, operations costs will scale linearly while development costs will take advantage of economies of scale. Therefore, the operations costs for these large constellations will dominate the life cycle costs, and high levels of automation will be required for many functions.

2.6 SUMMARY AND CONCLUSIONS

A distributed architecture makes sense if it can offer reduced cost or improved performance. Functional requirements specify minimum levels of acceptable performance, and include resolution, rate, integrity and availability requirements. Viable systems must satisfy these requirements throughout their lifetime. Compensation must be made following failures that cause a violation of requirements. "Improved Performance" thus relates to the ability of the system to satisfy requirements with a higher probability. "Reduced Cost" corresponds to lower lifetime costs that include the expected failure compensation costs.

Because the performance requirements, and the associated probability of satisfying them, are embedded in its calculation, lifetime cost is a useful metric for architecture analysis.

Distribution can offer improvements in isolation (resolution), rate, integrity and availability. The improvements are not all-encompassing, and in many cases are application specific. Nevertheless, it appears that adopting a distributed architecture can result in substantial gains compared to traditional deployments. Some of the more important advantages that distribution may offer are:

- Improved resolution corresponding to the large baselines that are possible with widely separated antennas on separate spacecraft within a cluster.
- Higher net rate of information transfer, achieved by combining the capacities of several satellites in order to satisfy the local and global demand.
- Improved availability through redundancy and path diversity. Frequently, the cost of adding a given level of redundancy is less for a distributed architecture.
- Lower failure compensation costs due to the separation of important system components among many satellites; only those components that break need replacement.

There are some problems, specific to distributed systems of small satellites, that must be solved before the potential of distributed architectures can be fully exploited. The most notable of these problems are:

- An increase of system complexity, leading to long development time and high costs
- Inadequacy of the data storage capacity that can be supported by the modest small satellite bus resources
- Difficulty of maintaining signal coherence among the apertures of separated spacecraft arrays, especially when the resolution requirements are high, or the target is highly-dynamic.

The resolution of these issues, and the proliferation of microtechnology, could lead toward a drastic change in the satellite industry. It seems clear that distribution offers a viable and attractive alternative for some missions. Large constellations of hundreds or thousands of small- and micro-satellites could feasibly perform almost all of the missions currently being carried out by

traditional satellites. For some of those missions, the utility and suitability of distributed systems looks very promising. More analysis is warranted in order to completely answer the question of where and when distribution is best applied, but the potential prospects of huge cost savings and improvements in performance are impossible to ignore. It therefore seems inevitable that massively distributed satellite systems will be developed in both the commercial and military sectors. We are living in a time of great changes, and the space industry has not escaped. Over the last few years, "faster, cheaper, better" has been the battle cry of those engineers and administrators trying to instigate changes to improve the industry. "Smaller, modular, distributed" may be their next verse.

References

1. "Foresight" Final Report from MIT 16.89 Space Systems Engineering class, Massachusetts Institute of Technology, Cambridge, MA, May, 1997.
2. Shaw, G., Yashko, G., Schwarz, R., Wickert, D. and Hastings, D. "Analysis Tools and Architecture Issues for Distributed Satellite Systems" in Microengineering for Aerospace Systems H. Helvijn (ed), Aerospace Press, El Segundo, CA (1997).
3. Infotech Report, *System Reliability and Integrity*, Infotech International Limited, 1978
4. Request For Proposal #F04701-95-R-0032. NPOESS program office, Feb. 1996.
5. Larson, Wiley J. and Wertz, James R. Space Mission Analysis and Design 2nd ed., Microcosm, Inc. and Kluwer Academic, Torrance, California, 1992
6. Larson and Wertz. Space Mission Analysis and Design, Microcosm Press, 1994.
7. Greenberg, Joel. AIAA Paper 96-1112-CP, 1996.
8. Congor, Robert *Microcosm Autonomous Navigation System (MANS)*. Presentation, August, 1995.

9. Tandler, John. "Automating the Operations of the ORBCOMM Constellation", 10th Annual AIAA/USU Conference on Small Satellites, Utah, September 1996
10. Hornstein, Rhoda Shalter. "On-Board Autonomous Systems: Cost Remedy for Small Satellites or Sacred Cow?" 46th International Astronautical Congress, Oslo, Norway, Oct. 2-6, 1995.
11. Collins, John T, Simon Dawson, & James R. Wertz. "Autonomous Constellation Maintenance System." 10th Annual AIAA/USU Conference on Small Satellites, 1996.

This page intentionally left blank

Chapter 3

Thruster Requirements for Local Satellite Clusters

This chapter examines the propulsive requirements necessary to maintain the relative positions of satellites orbiting in a local cluster. Formation of these large baseline arrays could allow high resolution imaging of terrestrial or astronomical targets using techniques similar to those used for decades in radio interferometry. A key factor in the image quality is the relative positions of the individual apertures in the sparse array. The relative positions of satellites in a cluster are altered by “tidal” accelerations which are a function of the cluster baseline and orbit altitude. These accelerations must be counteracted by continuous thrusting to maintain the relative positions of the satellites.

3.1 INTRODUCTION TO CLUSTER MISSIONS

Interferometry has been used for decades to produce images of astronomical objects in radio wavelengths with resolutions rivaling that of ground-based optical systems [1]. This technique, when deployed across a cluster of satellites, may be used to produce high resolution remote sensing images of terrestrial targets from space or provide a platform above the atmosphere for space-based viewing of astronomical objects.

3.1.1 Synthetic Apertures

The diffraction limited ground resolution of typical filled apertures is given by [2]

$$r_a \approx \frac{\lambda R_s}{b} \quad (3-1)$$

where b = typical aperture dimension and R_s = slant range to target.

Equation (3-1) indicates that increasing the aperture size improves the resolving power of the instrument. Aperture size is limited, however, by size and weight constraints of the launch vehicles which place the satellites in orbit. Synthetic Aperture Radar (SAR) can improve resolution at RF wavelengths from Low Earth Orbit (LEO) by utilizing the Doppler shifting of signals to "synthesize" an aperture much larger than the satellite's filled aperture. Resolutions of SAR systems are given by

$$r_a = \frac{b}{2} \quad (3-2)$$

where b is again a characteristic dimension of the filled aperture. Contrary to intuition, equation (3-2) indicates that reducing the filled aperture size improves the resolving power of the radar. At some point, however, aperture temperature, power output, and gain limitations preclude the use of smaller apertures. Table 3-1 lists allowable resolutions for a typical 10 m filled aperture sensing in the optical, infrared (IR), or radio frequency (RF) wavelengths at several altitudes.

Table 3-1 Current Achievable Resolution with 10m Aperture

Altitude	Optical $\lambda=0.5\mu\text{m}$	Infrared (IR) $\lambda=10\mu\text{m}$	Radio (RF) $\lambda=3\text{ cm}$
1,000 km	5 cm	1 m	5 m (SAR)
10,000 km	50 cm	10 m	30 km
35,768 km	1.8 m	18 m	107 km

3.1.2 Interferometry / Sparse Arrays

Another method to increase resolution is interferometry. Interferometers use separate apertures spaced some distance apart to create a sparse aperture as sketched in Figure 3-1

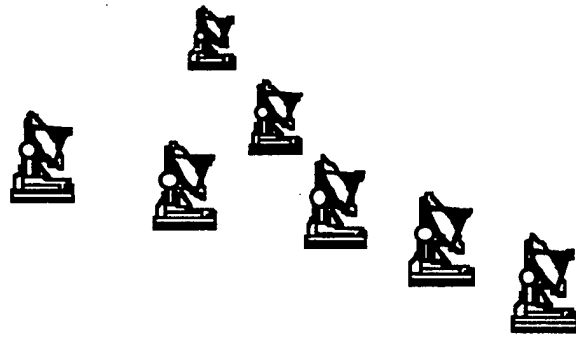


Figure 3-1 Ground-based Radio Interferometer

Interferometers were originally used in radio astronomy to distinguish discrete radio sources from the diffuse background. Synthesis is obtained by observing separately all the interferometer pairs that exist within a large aperture. A chessboard with only two chess pieces may be used as an analogy. All combinations of the pieces on the board must be sampled to recreate a uniform aperture. To accomplish this, the receiving elements are designed to be mobile across the so-called $u-v$ plane. As baselines increased, the rotation of the earth was used to sweep a range of spacings with fixed antennae. Very large baselines composed of widely separated antennae soon made sampling the entire $u-v$ plane impractical. Computer calibration techniques are now commonly used for sparse aperture synthesis.

The position and spacing of the elements is key to the quality of the image produced. The paths traced out by the electro-magnetic waves must be carefully controlled so that the signals may be coherently combined. This tolerance is typically $\lambda/20$. For a regularly spaced array, a positional error of a few wavelengths can cause significant sidelobes, even if the faulty positions are known exactly so that each element can be correctly phased [3]. In cases where the relative positions of the element are not known (such as with random arrays), calibrations can be carried out to improve the quality of the images providing the relative positions do not change from one image to the next. Although routine at RF wavelengths, sparse aperture formation at IR and visible wavelengths is still experimental.

The achievable angular resolution is diffraction limited in accordance with the Rayleigh criterion (Eq. 3-1). The size of the aperture, however, is the maximum linear distance between the individual elements. This distance is known as the baseline, B, so that [4]

$$\theta_r = \frac{\lambda}{B} \quad (3-3)$$

Table 3-2 lists the angular resolution versus sampled wavelengths for four existing interferometers along with the baseline of each system. Although aperture synthesis is well established in the radio spectrum, imaging of astronomical sources with multi-aperture interferometers is just beginning with the construction of the Infrared-Optical Telescope Array (IOTA) at the F.L. Whipple Observatory on Mount Hopkins, AZ. [5]

Table 3-2 Angular resolution of existing interferometers

Interferometer	Baseline	λ	Ang. Resol.
VLBI	8,500 km	1cm-1m	1e-4" to 1e-2"
VLA	35 km	1cm-5m	0.1" to 20"
Westerbrook	3.2km	10cm-1m	5" to 100"
Merlin	135 km	10cm-1m	0.1" to 1"

Source: Wohllenben [6] , Pg 17

3.1.3 Local Satellite Clusters

Forming space-based sparse apertures could be accomplished through the use of a local satellite cluster. Satellites in a local cluster orbit in formations such as those shown in Figure 3-2 and Figure 3-3. Although one or more reference satellites will be in standard Keplerian (ie. inertial) orbits, maintaining the formation will require the other satellites to orbit in planes parallel to the reference orbits. These non-inertial orbits are characterized by either a focus which is not located at the Earth's center of mass (Figure 3-2), or orbital velocities which do not provide the proper centripetal acceleration to offset gravity at that altitude (Figure 3-3). As expected, the Earth's

gravitation will act to move these satellites into Keplerian orbits. It will be shown that continuous low-level thrusting is required to maintain each satellite's position.

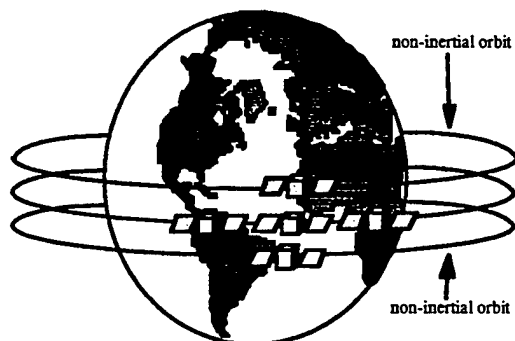


Figure 3-2 Cluster Formation Normal to Reference Orbit Plane

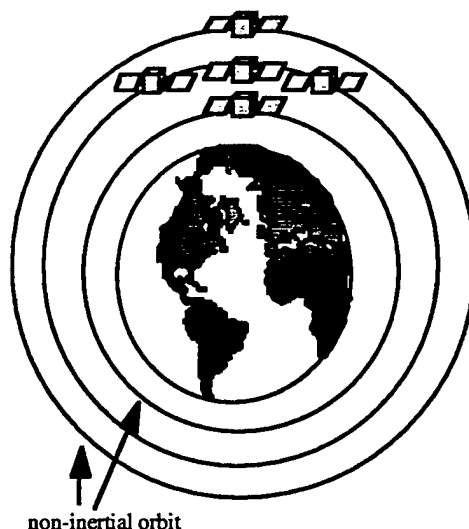


Figure 3-3 Cluster Formation in Plane of Reference Orbit

By coherently adding the signals received by several satellites, the cluster would, in effect, create a sparse aperture many times the size of a real aperture. The sparse aperture's large size could vastly increase the level of resolution possible. There are several possible advantages of creating a sparse array cluster. For example:

- 1) Extensive earth coverage could be achieved at GEO with a resolution similar to that of current satellites in LEO.

- 2) By turning satellites within the cluster “on and off” it may be possible to alter the dimensions of the sparse aperture and thus zoom in on a target detected in a broad, coarse field of view.

The gravitational forces which act on the satellites in non-inertial orbits will now be examined in more detail.

3.2 ORBITAL DYNAMICS OF SATELLITE CLUSTERS

3.2.1 Tidal Forces

Figure 3-4 shows the coordinate system for a simple two satellite cluster. Satellite 1 is in an inertial reference orbit at a distance, R , from the center of the Earth. Satellite 2's position relative to satellite 1 is \hat{r} .

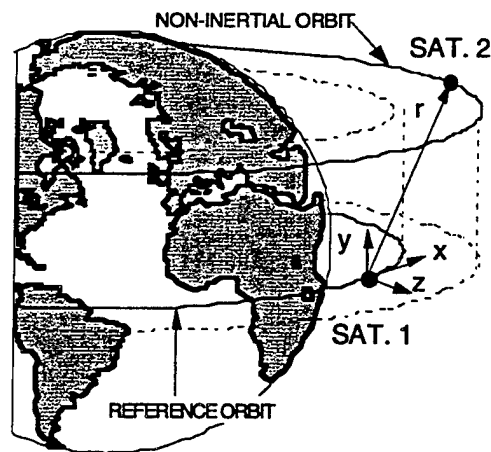


Figure 3-4 Satellite Cluster Coordinate System.

The motion satellite 2 with respect to 1 can be found using the linearized equations of relative motion for a circular reference orbit. These equations, known as the Clohessey-Wiltshire equations [7], are

$$\begin{aligned}
\Gamma_x &= \ddot{x} + 2\Omega\dot{z} \\
\Gamma_y &= \ddot{y} + \Omega^2 y \\
\Gamma_z &= \ddot{z} + 2\Omega\dot{x} - 3\Omega^2 z
\end{aligned} \tag{3-4}$$

where $\Omega = \sqrt{\mu/R^3}$.

One would intuitively expect a Γ_z term due to displacements along \hat{y} . It is eliminated by the linearization process in the derivation of equation (3-4) although it does appear in the full length equations.

$$\vec{\Gamma} = \begin{pmatrix} \ddot{x} + 2\Omega\dot{z} \\ \ddot{y} + \Omega^2 y \\ \ddot{z} - 2\Omega\dot{x} \end{pmatrix} - \begin{pmatrix} \Omega^2 x \\ \Omega^2 y \\ \Omega^2(R+z) \end{pmatrix} \left(1 - \frac{1}{C^{3/2}}\right) \tag{3-5}$$

where $C = \left(1 + \frac{2z}{R} + \frac{x^2 + y^2 + z^2}{R^2}\right)$.

Section 3 identifies the maximum displacements from the reference orbit that are feasible due spacecraft mass, power, and volume constraints. For those size clusters, this extra Γ_z term is negligible.

Equation (3-4) when multiplied by the $m_{s/c}$, describes the required on-board thrusting necessary to produce desired accelerations and velocities relative to some reference satellite in an inertial orbit. Notice that for $x = y = z = \dot{x} = \dot{y} = \dot{z} = \ddot{x} = \ddot{y} = \ddot{z} = 0$, (3-4) reduces to the case of a satellite in a inertial orbit where no thrusting is necessary to maintain its orbit under two-body orbit assumptions.

Even with $\dot{x} = \dot{y} = \dot{z} = \ddot{x} = \ddot{y} = \ddot{z} = 0$, y and z displacements create “tidal” forces which will tend to move the satellite into an inertial orbit as described by Janson [8]. These tidal forces need to be counteracted by thrusting in order to maintain the cluster. Tidal forces arise from displacements along \hat{z} because the cluster satellite is constrained to orbit with the same velocity as the reference satellite yet at a different altitude. Thus,

unlike the reference satellite, the gravitational attraction of the Earth is not exactly offset by the centripetal acceleration due to the satellite's circular motion. Displacements along \hat{y} force the satellite to orbit in a plane parallel to reference satellite. In that case, only a component of the gravity vector lies in the plane of the orbit. Once again, the centripetal acceleration is not offset by Earth's gravity. A displacement along \hat{x} can be considered a displacement along \hat{z} occurring at a point further ahead in the reference orbit.

3.2.2 Impulsive vs. Continuous Thrusting

To remain within the allowable relative position tolerances discussed previously, the cluster of satellites could use either a series of impulsive thruster firings at regular intervals or apply a lower, continuous thrust.

Consider the case of a satellite displaced along \hat{y} as shown in Figure 3-5. If no thrust were applied in the y direction, the displaced satellite would oscillate around the reference orbit completing one oscillation every orbit. In essence, it would be in an inertial orbit inclined with respect to the reference orbit. This motion relative to the reference orbit would temporarily move the satellite beyond the allowed tolerance for elements of a sparse array. Therefore, the thruster will need to fire an impulse bit which keeps the satellite within the tolerance region.

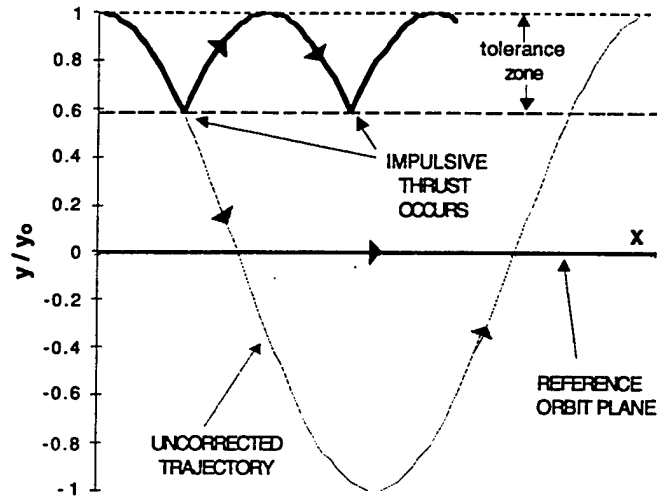


Figure 3-5 Impulsive Thrusting Procedure

At time $t=0$, halfway between impulse firings, $x = z = \dot{x} = \dot{z} = \ddot{x} = \ddot{z} = \Gamma_x = \Gamma_y = \Gamma_z = 0$.

Equation (3-4) then reduces to

$$\ddot{y} + \Omega^2 y = 0 \quad (3-6)$$

This undamped linear oscillator has the solution

$$y(t) = y_0 \cos(\Omega t) \quad (3-7)$$

$$\dot{y}(t) = -y_0 \Omega \sin(\Omega t) \quad (3-8)$$

$$\ddot{y}(t) = -y_0 \Omega^2 \cos(\Omega t) \quad (3-9)$$

Then, from equation (3-7) the time at which the satellite would drift beyond the tolerance limit is

$$t = \frac{1}{\Omega} \cos^{-1} \left(\frac{y_0 - \text{tol}}{y_0} \right) \quad (3-10)$$

Figure 3-6 shows the plot of equation (3-10) at several altitudes. It can be seen from the figure that, at all altitudes, as the required relative position tolerance decreases the time the satellite is able to drift before firing an impulse decreases. The largest value

of tolerance/displacement will be for RF sensing sparse apertures in LEO. For an RF cluster satellite sensing at $\lambda = .05\text{m}$, tolerances will be on the order of 2.5 mm. At 1000 km altitude and displaced 25m, this tolerance/displacement is $1\text{e-}4$. Figure 3-6 indicates that the satellite could drift for 14 seconds. In the optical region, however, allowable drift time is approximately 0.05 seconds.

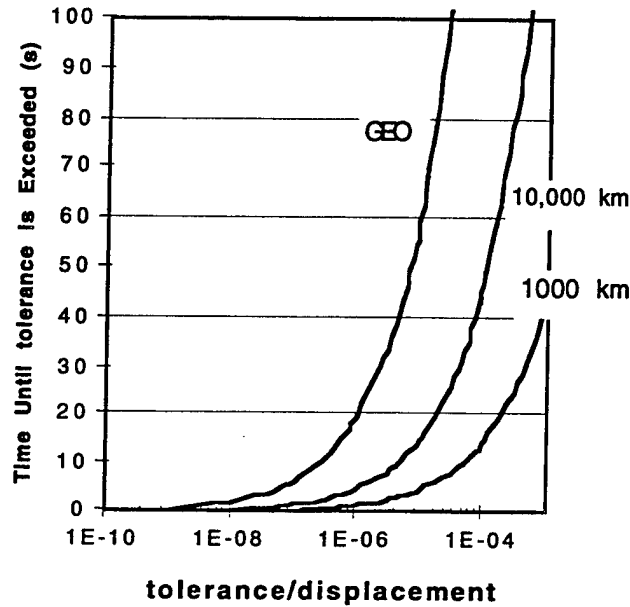


Figure 3-6 Time Until Tolerance is Exceeded

Assuming that the satellite's y velocity after the impulse is exactly negative that before the impulse, and that the tidal forces and impulse thrust are constant during the time the impulse is applied, then

$$\frac{I_B}{m_{s/c}} = 2y_o\Omega\sin(\Omega t) + [y_o\Omega^2\cos(\Omega t)](\Delta t) \quad (3-11)$$

where t is found from equation (3-10) and Δt is the thruster firing time.

The total impulsive firings during the mission life is then

$$N_f = \frac{\text{life}}{2t + \Delta t} \quad (3-12)$$

Calculating the total impulsive ΔV expended over the mission life,

$$\Delta V = N_f \frac{I_B}{m_s/c} \quad (3-13)$$

Figure 3-7 compares the ΔV expended for continuous thrusting to that of impulsive thrusting. The figure shows that for a given displacement, as the tolerance region in which the satellite can drift increases, only negligible amounts of ΔV can be saved by using impulsive thrusts. As the tolerances tighten (and the time between impulsive thrusts shortens), the ΔV expended for a impulsive thrust approaches that expended by continuous thrusting.

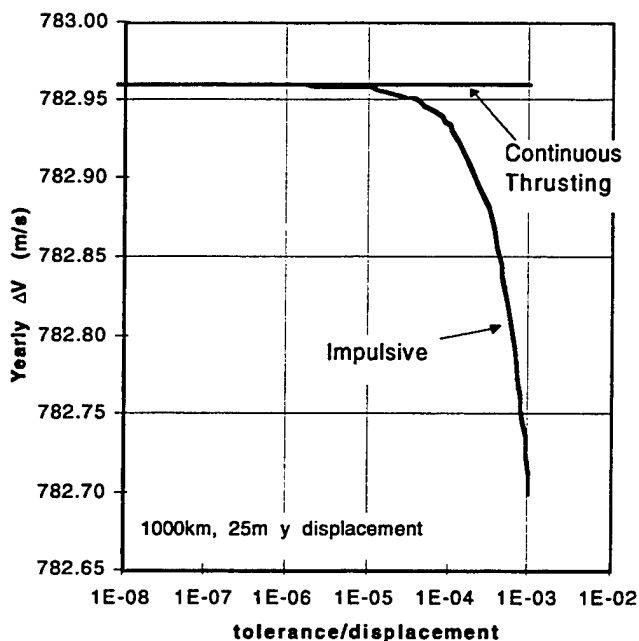


Figure 3-7 Propellant Savings from Impulsive Thrusting.

The previous analysis would indicated that, at the broadest relative position tolerance levels, the maximum time between required impulsive thrusts is on the order of seconds. For optical and infrared wavelengths, this time is on the order of tenths of a second. Further, at these short thrusting intervals, only minimal amounts of propellant

savings result from impulsive thrusting. Therefore, continuous thrusting will be assumed for the rest of this analysis.

3.2.3 Dynamic Clusters

For the situation where satellite positions are fixed relative to each other, the total ΔV expended during the satellite's mission life is

$$\Delta \dot{V} = (\dot{\Gamma}) \text{life} \quad (3-14)$$

where $\dot{\Gamma}$ is the acceleration produced continuously by an on-board propulsive system to counteract tidal forces. Equation (3-4) indicates that the required thrust per unit of spacecraft mass is larger for a satellite stationed at a greater distance from the reference orbit. From equation (3-14) for a given mission life, a satellite stationed far from the reference orbit will consume more fuel than a satellite stationed closer. It may be desirable, therefore, to rotate the positions of the satellites during their life as a means of distributing the fuel consumption amongst all the satellites in the cluster.

Consider the case, illustrated in Figure 3-8, where the satellites in a cluster continually rotate in a circular pattern relative to the reference satellite. Figure 3-8 shows only two of the many satellites comprising the cluster. This is one of many possible methods by which satellites in a cluster change position, but it serves well as an example of a "dynamic cluster".

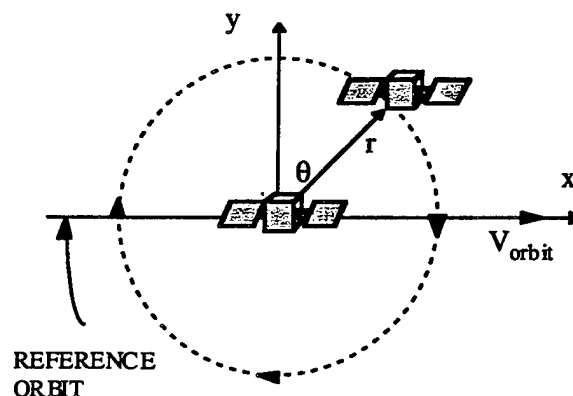


Figure 3-8 Dynamic Cluster Formation

For this situation,

$$\begin{aligned} x &= r \sin(\theta) \\ y &= r \cos(\theta) \\ z &= 0 \end{aligned} \quad (3-15)$$

By substituting the relations from equation (3-15), equation (3-4) becomes

$$\begin{aligned} \Gamma_x &= -r\dot{\theta}^2 \sin \theta \\ \Gamma_y &= -r \cos \theta (\Omega^2 + \dot{\theta}^2) \\ \Gamma_z &= 2r(\cos \theta) \Omega \dot{\theta} \end{aligned} \quad (3-16)$$

where $\Omega = \sqrt{\mu/R^3}$.

It can be seen from equation (3-16) that the required thrust levels of a satellite in a dynamic cluster are a function of the cluster radius, r , the cluster's reference altitude, the position of the satellite, θ , as well as the rate at which the satellite rotates about the reference satellite, $\dot{\theta}$. Figure 3-9 shows ΔV expended by all satellites in the example dynamic cluster can be as low as 54% that expended by a satellite at the far edge of a static, non-rotating cluster.

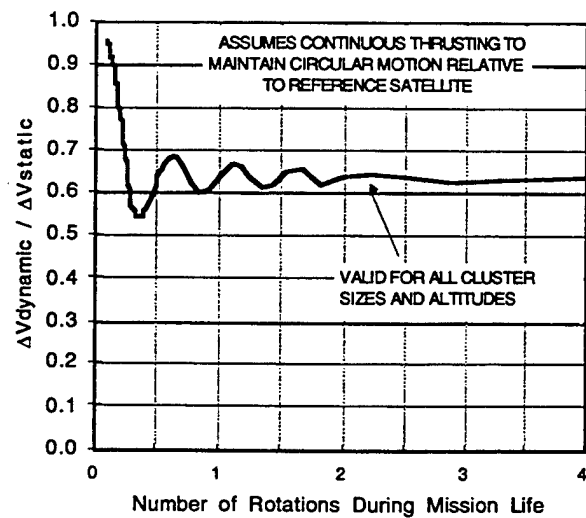


Figure 3-9 Reduction in Cluster Maintenance ΔV

As the number of rotations about the reference satellite increases beyond about 1/3, the ΔV ratio begins to increase again because the satellite is spending more time displaced further from the reference orbit along $-\hat{y}$. At a rate of 1 rotation during the mission, the ΔV expended is about 65% that of the worst case satellite in a static cluster. The ΔV ratio levels off at this value for more than 5 rotations during the mission. Although not shown in Figure 3-9, as the rotation rate is increased further, the ΔV required just to maintain the circular motion around the reference satellite begins to dominate. At rate of a few hundred rotations during the mission, the ΔV ratio increases above unity indicating it is no longer beneficial to rotate the cluster satellites.

It should be stated that a sparse aperture might be formed using a constellation of satellites rather than a local cluster, depending on whether the positional tolerance problem could be solved. For that situation, all satellites would orbit in inertial orbits and the sparse aperture would be formed using whatever satellites are available as they fly over the region of interest. The ΔV for maintaining that "sparse aperture" would be zero. The analysis throughout the rest of this paper, however, is focused only on the requirements of maintaining a local static cluster.

3.3 PROPULSION SYSTEM REQUIREMENTS

Based on the acceleration levels presented in section 2, the propulsion system requirements to maintain a local satellite cluster can be calculated. The feasible range of specific impulse and efficiency, constrained spacecraft mass, volume and power considerations, is the primary characteristic to be determined.

3.3.1 Current Thruster Characteristics

Two classes of propulsion, chemical and electric, are currently used as station-keeping thrusters on-board spacecraft. These two classes along with ranges of

specific impulse and efficiency can be displayed graphically as shown in Figure 3-10. These ranges reflect some technology extrapolations appropriate for the next 5 to 10 years. For example PPT efficiencies are currently around 10% but work is under way which aims to extend them beyond 20%. This format will be used as a template for a comparison of current thruster capabilities to those required for maintaining cluster formations. It is important to point out that Figure 3-10 simply shows the range of I_{sp} vs. η . If a local cluster formation requires a combination of I_{sp} and η which falls within the shaded box, there is no guarantee a thruster with those characteristics exists. However, if the cluster satellite needs a combination of I_{sp} and η which does not fall within a shaded box, then it can be said that no current thruster exists which is able to meet those requirements.

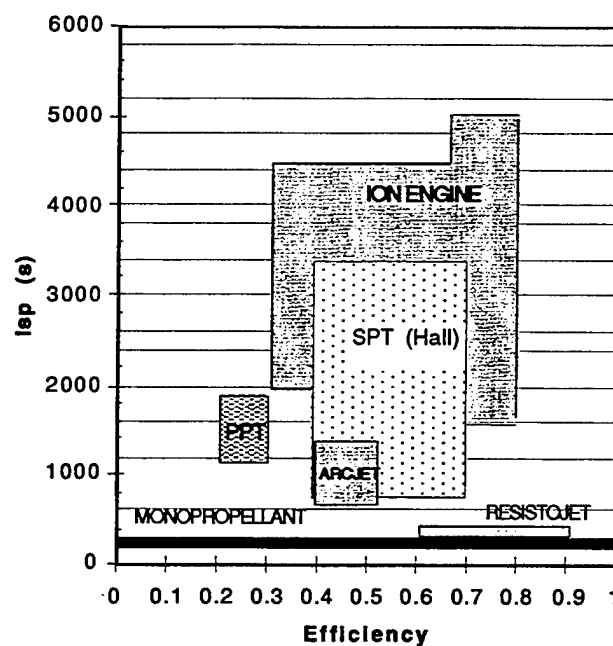


Figure 3-10 Current Thruster Capabilities [9], [10]

3.3.2 Methodology

In determining the feasible range of thruster I_{sp} and η necessary to maintain a local satellite cluster, the following assumptions were made:

- The satellites operate as a static cluster maintaining a fixed displacement normal to the reference orbit.
- I_{sp} and η are the same for all thrusters used in cluster maintenance and station-keeping
- Thrust levels of each thruster are constant during the life of the mission.
- Any cluster maintenance and station-keeping maneuvers are performed continuously.
- The spacecraft and propellant tanks are spherical.
- Spacecraft total mass is constant throughout the life of the mission.
- An additional 50m/s of propellant per year is allocated for traditional station-keeping requirements.

A spacecraft displaced a given distance from the reference orbit using a thruster operating at a given η and I_{sp} must satisfy the following three design constraints.

$$\begin{aligned}
 \frac{D_{\text{tank}}}{D_{s/c}} &< \left(\frac{D_{\text{tank}}}{D_{s/c}} \right)_{\text{max}} \\
 \frac{m_p + m_{pp}}{m_{s/c}} &< \left(\frac{m_p + m_{pp}}{m_{s/c}} \right)_{\text{max}} \\
 \frac{P_{in}}{P_{s/c}} &< \left(\frac{P_{in}}{P_{s/c}} \right)_{\text{max}}
 \end{aligned} \tag{3-17}$$

where

m_p = mass of propellant

m_{pp} = mass of power plant

The values for the maximum ratios allow margin for the satellite to accomplish tasks other than simply operating the thrusters. Specifically, the three statements gauge whether or not there is, once station-keeping requirements have been met, sufficient volume, mass, and power available on board the satellite to perform mission operations such as payload, communications, etc. If the answer to one or more of

these criteria is no, then it is concluded that a satellite of mass, $m_{s/c}$, and propellant mass fraction, $m_p/m_{s/c}$ is *unable* to adequately maintain its position, \hat{r} , from the reference orbit at an altitude, h , for a mission time, $life$, using a thrusters with specific impulse, I_{sp} and efficiency η .

The values for the three constraints listed above can be found as follows:

1. For a given cluster size and altitude, the accelerations along \hat{y} can be found by evaluating equation (3-4)
2. The corresponding thrust to counteract those accelerations is given by

$$\dot{\vec{F}}_{tot} = m_{s/c} \dot{\vec{\Gamma}} \quad (3-18)$$

3. Knowing the acceleration and assuming continuous thrusting, the total ΔV required is

$$\Delta V_{tot} = (|\Gamma_x| + |\Gamma_y| + |\Gamma_z|)(life) \quad (3-19)$$

4. The total propellant used during the life of the mission is simply

$$m_p = \left(1 - e^{-\Delta V / I_{sp} g_0}\right) m_{s/c} \quad (3-20)$$

5. The diameter of the spacecraft is

$$D_{s/c} = \left(\frac{6 m_{s/c}}{\pi \rho_{s/c}}\right)^{\frac{1}{3}} \quad (3-21)$$

6. Using m_p , the diameter of the propellant tank is

$$D_{tank} = \left(\frac{6 m_p}{\pi \rho_p}\right)^{\frac{1}{3}} \quad (3-22)$$

7. The total power available to the spacecraft is

$$P_{s/c} = m_{s/c} \alpha_{s/c} \quad (3-23)$$

8. For electric propulsion, a power plant is required on-board the satellite to provide power to the thruster. Therefore, the maximum required input power to the thrusters, using the current value of I_{sp} being evaluated and thrust levels from step 2 is

$$P_{in} = \frac{I_{sp} g(F_{max})}{2\eta} \quad (3-24)$$

9. The mass of the power plant can be found using input power calculated in step 8 along with the specific power of the power plant

$$m_{pp} = \frac{P_{in}}{\alpha_{pp}} \quad (3-25)$$

Table 3-3 lists the maximum values chosen for these constraints as well as other input parameters.

Table 3-3 Baseline parameters

α_{pp}	10 W/kg
$\alpha_{s/c}$	2 W/kg
ρ_p	500 kg/m ³
$\rho_{s/c}$	79 kg/m ³
life	5 yrs
$m_{s/c}$	100 kg
$(m_p/m_{s/c})_{max}$	0.1
$(P_{in}/P_{s/c})_{max}$	0.20
$(D_{tank}/D_{s/c})_{max}$	0.33
$[(M_p + M_{pp})/M_{s/c}]_{max}$	0.30

3.3.3 Analysis of Cluster Missions

The methodology developed in the previous section can now be used to determine the range of thruster specific impulse and efficiency which can maintain the relative positions of a satellite in a cluster without exceeding the satellite design ratios. Figure 3-11 through Figure 3-13 illustrate the feasible regions of thruster specific impulse vs. efficiency for clusters orbiting at various altitudes. At specific impulses below the

feasible regions, the required propellant to maintain the cluster during the five year mission life exceeds the assumed 10% maximum initial propellant mass fraction. In actuality, the thruster must operate at an I_{sp} above this lower limit since propellant utilization, $\eta_u=1$, is assumed in this initial analysis. Combinations of specific impulse and efficiency above and to the left of the feasible regions result in thruster power requirements greater than the allowable 20% of spacecraft power. Because the thruster power is determined by equation (3-24) an increase in thruster efficiency allows for higher specific impulses without exceeding the power limitations.

As shown in Figure 3-11 a satellite in a cluster orbiting at 1000 km altitude with a 25 m baseline requires thrusters operating at a minimum specific impulse and efficiency of 2000s and 40% respectively. SPT's and ion engine technology can currently achieve these ranges. If the baseline is increase to 35 m, thruster requirements increase to 2700s specific impulse and 80% efficiency. Similar effects can be seen for clusters orbiting at 10,000 km (Figure 3-12) and at GEO (Figure 3-13). At 10,000 km, cluster baselines in the hundreds of meters can be achieved using SPT or ion engine technologies. These baselines increase to 4000-6000 m for clusters stationed at GEO. At no altitude can chemical propulsion maintain cluster formations for the 5 year life.

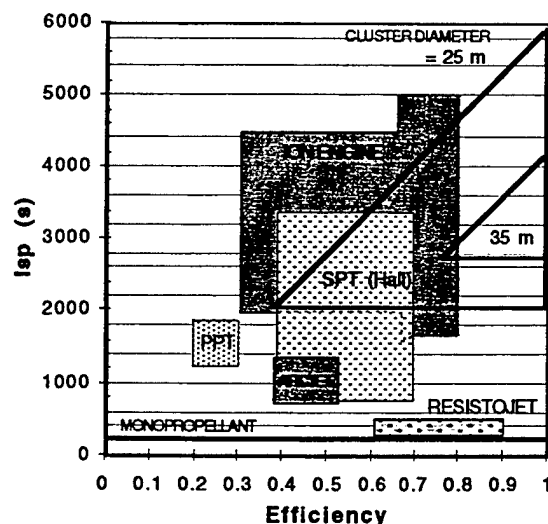


Figure 3-11 Feasible I_{sp} vs. η at 1,000 km

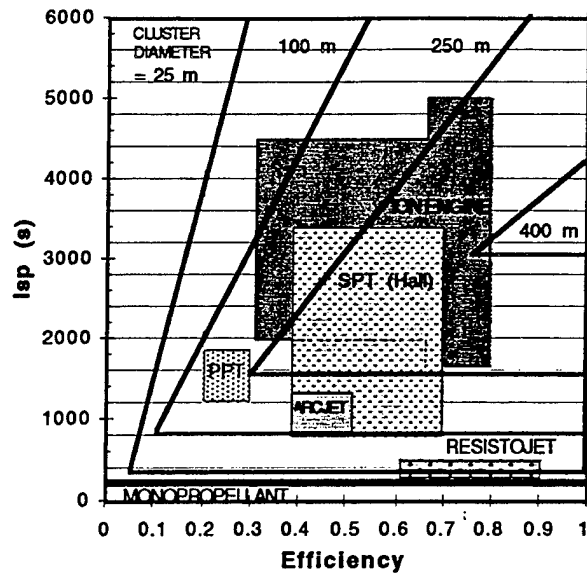


Figure 3-12 Feasible I_{sp} vs. η at 10,000 km

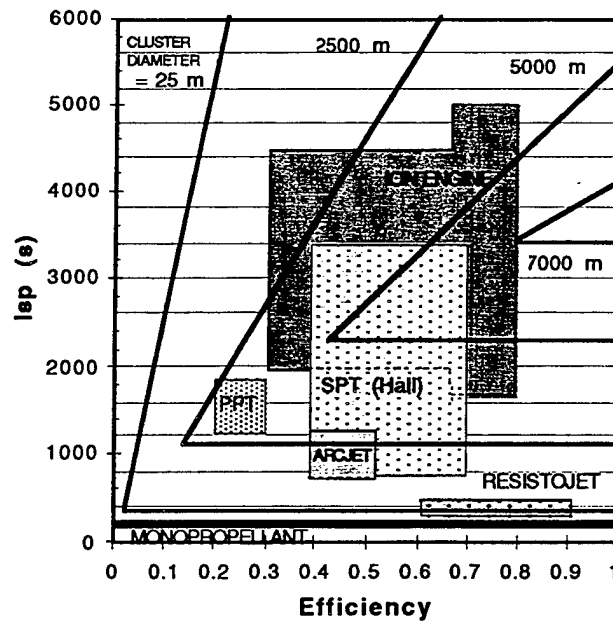


Figure 3-13 Feasible I_{sp} vs. η at GEO

Moving a cluster to higher orbits dramatically increases the allowable baselines for sparse apertures. However, due to the increased range to target from GEO, ground resolutions increase by only about a factor of 5 (see Table 3-4). The achievable

resolutions from the sparse aperture baselines shown in Figure 3-11 through Figure 3-13 are listed in Table 3-4 and Table 3-5.

The achievable resolutions from the sparse aperture baselines shown in Figure 3-11 through Figure 3-13 are listed in Table 3-4 and Table 3-5.

Table 3-4 Feasible Sparse Aperture Ground Resolution

ALTITUDE	CLUSTER BASELINE	VISIBLE (.5mm)	IR (10mm)	RF (5cm)
1000 km	25 m	20 mm	40 cm	2 km
	35 m	14 mm	29 cm	1.5 km
10,000 km	25 m	200 mm	400 cm	20 km
	100 m	50 mm	100 cm	5 km
	200 m	25 mm	50 cm	2.5 km
	400 m	13 mm	25 cm	1.3 km
35768 km	25 m	710 mm	15 m	72 km
	2000 m	9 mm	18 cm	900 m
	5000 m	4 mm	7 cm	350 m
	7000 m	3 mm	5 cm	250 m

For mission where angular resolution is the main concern (such as for imaging of astronomical objects), Table 3-5 shows that angular resolution can be increased by a factor of order 1000 if the cluster is positioned in GEO rather than LEO. These values can be compared with the angular resolutions given for terrestrial interferometers in Table 3-2.

Table 3-5 Achievable Sparse Aperture Angular Resolutions

ALTITUDE	CLUSTER BASELINE	VISIBLE (.5mm)	IR (10mm)	RF (5cm)
1000 km	25 m	$4 \times 10^{-3}''$	$82 \times 10^{-3}''$	412"
	35 m	$3 \times 10^{-3}''$	$59 \times 10^{-3}''$	294"
10,000 km	25 m	$4 \times 10^{-3}''$	$82 \times 10^{-3}''$	412"
	100 m	$1 \times 10^{-3}''$	$20 \times 10^{-3}''$	103"
	250 m	$412 \times 10^{-6}''$	$8 \times 10^{-3}''$	40"
	400 m	$258 \times 10^{-6}''$	$5 \times 10^{-3}''$	25"
35768 km	25 m	$4 \times 10^{-3}''$	$82 \times 10^{-3}''$	412"
	2000 m	$51 \times 10^{-6}''$	$1 \times 10^{-3}''$	5"
	5000 m	$20 \times 10^{-6}''$	$415 \times 10^{-6}''$	2"
	7000 m	$15 \times 10^{-6}''$	$294 \times 10^{-6}''$	1.5"

Figure 3-14 shows the thrust levels per unit of spacecraft mass required by a satellite displaced from the reference orbit by 15m, 150m, and 2750m (30 m, 300m, 5500m cluster baselines respectively). These values were found using the full length equation (3-5). Combinations of cluster baselines and altitudes which can be achieved with moderate propulsive requirements (Figure 3-11 through Figure 3-13) are all seen from Figure 15 to require thrust levels on the order of $15\mu\text{N}$ per kg of spacecraft mass along \hat{y} . Thrust/mass along \hat{z} is approximately 5 orders of magnitude smaller, justifying the use of the linearized equation (3-4). In addition, thrust levels along \hat{x} equal zero.

This is also apparent in Figure 3-15 which shows the required ΔV for a five year mission. The ΔV expended in \hat{z} is negligible compared to that expended in \hat{y} .

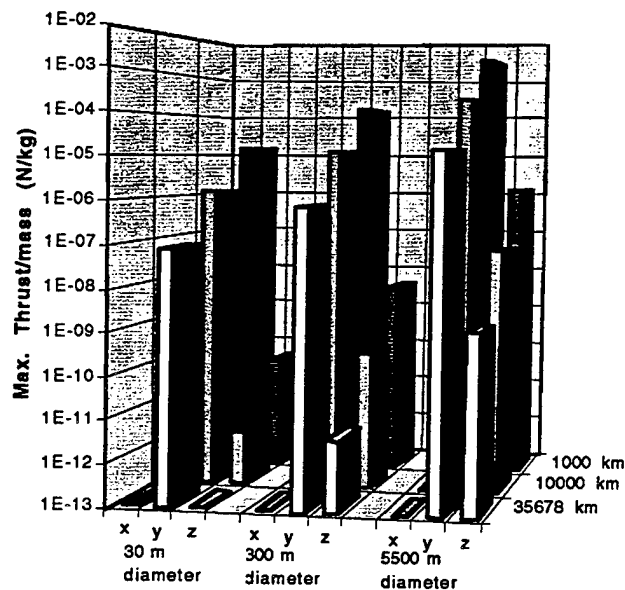


Figure 3-14 Thrust/mass Levels

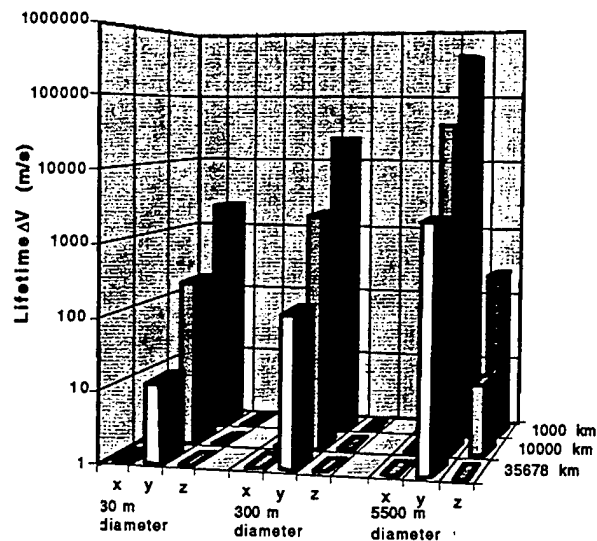


Figure 3-15 Required ΔV

3.4 SUMMARY AND CONCLUSIONS

This chapter has examined the propulsion system requirements for maintaining a local satellite cluster formation in Earth's orbit for the purpose of forming sparse aperture arrays. Near continuous thrusting by the propulsive system was found necessary to maintain the relative positions of the satellites within allowable tolerances. Satellite mass, volume, and power constraints limit reasonable cluster baselines to approximately 30 m, 300 m, and 5000 m at 1000 km, 10,000 km, and GEO altitudes respectively. To maintain these cluster baselines, the propulsive system must operate at minimum I_{sp} and efficiency equal to approximately 3000s and 65% respectively with a thrust/spacecraft mass ratio of approximately $15\mu\text{N/kg}$.

References

1. Swift, C. T. "Terrestrial Sensing with Synthetic Aperture Radiometers." IEEE MTT-S International Microwave Symposium Digest, vol. 1, p. 387-388, Boston MA, June 10-14, 1991.

2. Larson, W. J., Wertz, J. R. (editors), Space Mission Design and Analysis 2nd ed. Kluwer Academic Publishers, Boston, 1992.
3. Wall, J.V., Modern Technology and Its Influence on Astronomy. Cambridge University Press, Cambridge, 1990.
4. Heimiller, R.C., Belyea, J.E., Tomlinson, P.G., "Distributed Array Radar." IEEE Transactions on Aerospace and Electronic Systems vol. AES-19, No. 6, November 1983.
5. F. P. Schloerb, "Imaging Interferometry: Lesson from the Ground." SPIE Proceedings vol. 1947, pp 249-260, Orlando, FL. April 15-16, 1993.
6. R. Wohlleben, H. Mattes, T.H. Krichbaum, Interferometry in Radioastronomy and Radar Techniques. Kluwer Academic Publishers, Boston, 1991.
7. Prussing, J.E., Conway, B.A. Orbital Mechanics. Oxford University Press, New York, 1993.
8. S.W. Janson, "The On-Orbit Role of Electric Propulsion." AIAA 93-2220, 29th Joint Propulsion Conference and Exhibit, June 28-30, 1993, Monterey, CA.
9. Sutton, G.P., Rocket Propulsion Elements 6th ed., John Wiley & Sons, Inc., New York, 1992.
10. G. Malyshev et. al. "Comparative Analysis of the Propulsion System for the Small Satellite", IEPC-95-156, 24th International Electric Propulsion Conference, Moscow, Russia, Sept. 19-23, 1995.

Chapter 4

Modeling Ion Engine Performance

In Chapter 3, the propulsion requirements for maintaining the relative positions of satellites in a local cluster were determined. To maintain reasonably sized formations, it was found that station-keeping thrusters required specific impulse, thruster efficiency and thrust level characteristics similar to those of ion thrusters. The rest of this thesis examines the performance of micro ion engines. This chapter formulates an analytical model, known as Brophy's Theory, to predict the performance of cylindrical ring-cusped ion engines. In later chapters, Brophy's model will be used to predict the performance of cylindrical ion engines as they are scaled down in size three orders of magnitude and a linear ion microthruster concept.

4.1 OPERATION OF ION ENGINES

Figure 4-1 shows the cross section of a typical cylindrical ion engine. A neutral gas, such as Xenon or Argon, is fed into the discharge chamber. Electrons are injected into the chamber from a cathode emitter. On occasion, the electrons collide with the neutral atoms with sufficient energy to ionize one neutral resulting in a positively charged ion and one or more additional electrons. During steady state operation, the neutrals, ions and electrons form a quasi-neutral plasma. Ions in the vicinity of the grid are accelerated across a potential difference forming an ion beam exiting the chamber and producing thrust. In some configurations a third grid surface is added to control ion velocity (specific impulse) without affecting ion mass flow rate (thrust). Electrons in the chamber

eventually reach the anode where they either complete the circuit back to the cathode or are injected into the ion beam to neutralize it.

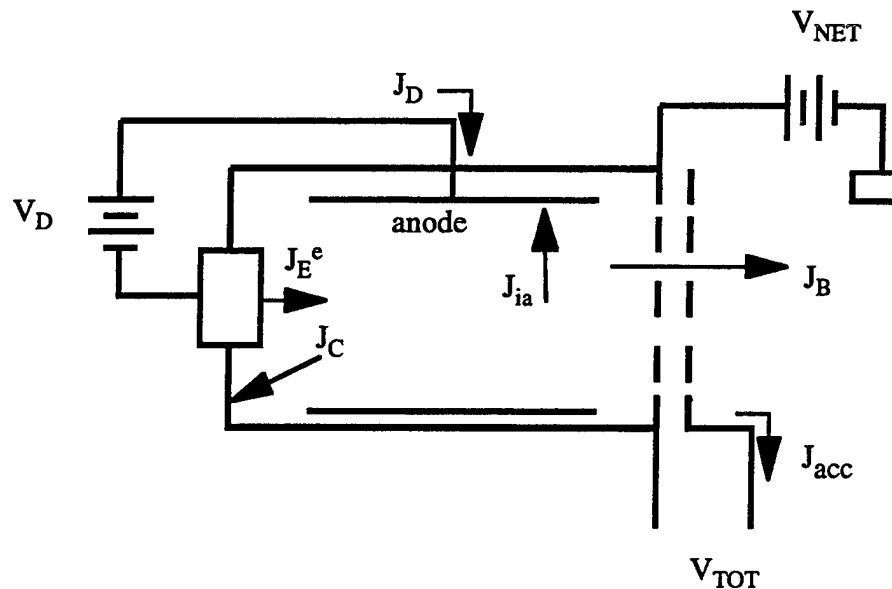


Figure 4-1 Current Balances in Ion Engines

The following is a list of definitions for the terms shown in Figure 4-1

- J_B = Beam ion (and neutralizer electron current)
- J_E = cathode emitted current
- J_C = ion current to cathode-potential surfaces
- J_D = current through discharge power supply
- J_P = total ion production rate
- J_{ia} = Ion current to anode
- J_{acc} = Ion current intercepted by accelerator grid
- V_D = Discharge potential (potential difference between cathode and plasma)
- V_{net} = Neutralizer potential (potential difference between plasma and ion beam)
- V_B = Acceleration grid potential

4.2 BROPHY'S MODEL

Brophy's model [1] uses the conservation equations for mass, charge, and energy to predict the beam ion production cost, ϵ_B . ϵ_B is the energy necessary to produce an ion which becomes part of the beam. The derivations in this chapter are a more annotated version of those found in reference [2].

4.2.1 Fundamental Equations

Beam ion production energy can be defined as the total energy expended per beam ion less the useful energy per beam ion. Equations (4-1) and (4-2) define useful power and total power respectively

$$\text{UsefulPower} = J_B (V_B + V_D) \quad (4-1)$$

$$\text{Total Power} = J_B V_B + J_D V_D + J_{\text{acc}} V_B + P_{\text{heaters}} \quad (4-2)$$

Using equations (4-1) and (4-2), ϵ_B can be found as shown in equation (4-3).

$$\epsilon_B = \frac{\text{TotalPower} - \text{UsefulPower}}{J_B} = \frac{(J_D - J_B)V_D + J_{\text{acc}}V_B + P_H}{J_B} \quad (4-3)$$

Examining Figure 4-1 the following current balance can be found

$$J_D - J_B = J_E + J_C + J_{\text{acc}} \quad (4-4)$$

Substituting equation (4-4) into equation(4-3) and expanding yields

$$\epsilon_B = \left(\frac{J_E V_D + P_H}{J_P} \right) \frac{J_P}{J_B} + \frac{J_C V_D + J_{\text{acc}}(V_B + V_D)}{J_B} \quad (4-5)$$

This can be rewritten as

$$\epsilon_B = \frac{\epsilon_P}{f_B} + \frac{f_C}{f_B} V_D + \frac{f_{\text{acc}}}{f_B} (V_B + V_D) \quad (4-6)$$

where

$$\epsilon_P = \frac{J_E V_D + P_H}{J_P} \quad (4-7)$$

$$\text{and } f_B = \frac{J_B}{J_P}, f_C = \frac{J_C}{J_P}, f_{\text{acc}} = \frac{J_{\text{acc}}}{J_P}$$

4.2.2 Discharge Energy Balance

Equation (4-6) defines in general terms the expression for beam ion production cost. The goal from here on is to express the terms in equation (4-6) as parameters which are known or can be measured. First, looking at the terms in the equation for ϵ_p an energy balance for the discharge chamber can be expressed as

$$U_+ + \sum_j J_j \frac{U_j}{J_P} + \frac{J_{LP} V_D}{J_P} + \epsilon_B \left(\frac{J_P + J_E - J_{ia} - J_{LP}}{J_P} \right) = \frac{J_E V_D}{J_P} = \epsilon_P - \frac{P_H}{J_P} \quad (4-8)$$

where

U_+ = ionization energy per ion

U_j = excitation energy of level j

J_j = excitation rate (to level j)

J_{LP} = loss rate of primary electrons

ϵ_m = mean energy of Maxwellian electron group

Because the first two terms in equation (4-8) are known constants specific to the type of propellant we can define

$$\epsilon_o = U_+ + \sum_j J_j \frac{U_j}{J_P} \quad (4-9)$$

Substituting equation (4-9) into equation (4-8) and expanding gives

$$\frac{J_E V_D}{J_P} = \epsilon_o + \epsilon_m + (V_D - \epsilon_m) \frac{J_{LP} J_E}{J_E J_P} - \frac{J_{ia}}{J_P} \epsilon_m + \epsilon_m \left(\frac{J_E}{J_P} \right) \quad (4-10)$$

Solving for $\frac{J_E V_D}{J_P}$ yields

$$\frac{J_E V_D}{J_P} = \frac{\epsilon_o + \epsilon_m \left(1 - \frac{J_{ia}}{J_P} \right)}{\left(1 - \frac{J_{LP}}{J_E} \right) \left(1 - \frac{\epsilon_m}{V_D} \right)} \quad (4-11)$$

Substituting equation (4-11) into (4-7) and writing $P_H = J_E V_C$, the equation for ϵ_p becomes

$$\epsilon_P = \frac{\epsilon_o + \epsilon_m \left(1 - \frac{J_{ia}}{J_P}\right)}{\left(1 - \frac{J_{LP}}{J_E}\right) \left(1 - \frac{\epsilon_m}{V_D}\right)} \left(1 + \frac{V_C}{V_D}\right) \quad (4-12)$$

We can define

$$\epsilon_P^* = \frac{\left[\epsilon_o + \epsilon_m (1 - f_{ia})\right] \left(1 + \frac{V_c}{V_D}\right)}{1 - \frac{\epsilon_m}{V_D}} \quad (4-13)$$

so that equation (4-12) becomes

$$\epsilon_P = \frac{\epsilon_P^*}{\left(1 - \frac{J_{LP}}{J_E}\right)} \quad (4-14)$$

ϵ_P^* is seen to be the energy per ion created if no primary electrons were to escape. The terms for ϵ_P^* in equation (4-13) will be related later in equation (4-32) to known or measurable parameters. Now, however, let us express J_{LP}/J_E in known or measurable parameters.

4.2.3 Survival Equation for Primary Electrons

$$J_{LP}/J_E = e^{-\sigma_{tot} n_n l_e} \quad (4-15)$$

where $\sigma_{tot} = (\sigma_+ + \sigma_{exc})_{primaries}$.

Also, l_e is the path for a primary electron before it would be captured by the anode, if it did not collide with a neutral before that. This path length is that of the electron's helical path around one of the magnetic lines of force created by the confinement magnets.

The neutral density in equation (4-15) is related to the flow rate by

$$n_n = \frac{\Gamma_n}{\frac{\bar{c}_n}{4} \phi_n} = \frac{\dot{m}}{m_i A_g} (1 - \eta_u) \frac{4}{\bar{c}_n \phi_n} \quad (4-16)$$

where ϕ_n = grid system transparency for neutrals
 η_u = utilization efficiency)

This expression for neutral density can be substituted into equation (4-15) to give

$$\frac{J_{LP}}{J_E} = \exp \left[-\frac{4\dot{m}(1 - \eta_u)\sigma_{tot}l_e}{m_i A_g \bar{c}_n \phi} \right] \quad (4-17)$$

Continuing then, equation (4-17) can be substituted into equation (4-14) resulting in

$$\epsilon_p = \frac{\epsilon_p^*}{1 - \exp[-C_o \dot{m}(1 - \eta_u)]} \quad (4-18)$$

where $C_o = \frac{4\sigma_{tot}l_e}{m_i A_g \bar{c}_n \phi}$

The quantity C_o is a measure of the confinement effectiveness for primary electrons (better for long electron path l_e , small grid open area $A_g \phi_n$). If $C_o \rightarrow \infty$, the energy cost per ion, ϵ_p , tends to the limit ϵ_p^* , which then represents the cost per ion with no primary losses.

Keep in mind that the ultimate goal is to find ϵ_p , equation (4-6), in terms of known or measurable parameters. Up to this point, we have been working to express ϵ_p in such terms. Equation (4-18) represents the progress thus far, but it still remains to express ϵ_p^* in such terms. This is the focus of the next section.

4.2.4 Calculation of Primary / Secondary Population Ratio

Primary electrons are endowed initially with an energy V_D , and, if they did not escape, would all thermalize eventually, to an energy ϵ_m . The energy transferred to the neutrals by each primary is $(V_D - \epsilon_m)$. In steady state operation, this energy loss by the primaries must exactly balance the energy gained by the neutral propellant. Transfer of energy from the primary electrons is assumed to occur in four ways; 1) ionization of atoms by primaries, 2) excitation of atoms by primaries, 3) ionization of atoms by secondaries (Maxwellian), 4) excitation of atoms by secondaries. Thus the balance of energy rate per unit volume is ,

$$\dot{E}_{\text{into}} = \dot{E}_{\text{pi}} + \dot{E}_{\text{pe}} + \dot{E}_{\text{si}} + \dot{E}_{\text{se}} \quad (4-19)$$

The rate at which primaries disappear (i.e. thermalize to secondaries) is simply the rate of ionization or excitation by primaries (a primary is assumed to become a secondary-Maxwellian after one ionization or one excitation). So, the net energy input rate per unit volume due to injection of primaries is (assuming the primaries do not leave the chamber without ionizing or exciting a neutral)

$$\dot{E}_{\text{into}} = n_n n_p v_p \sigma_{\text{tot}} (V_D) (V_D - \epsilon_m) \quad (4-20)$$

where $\sigma_{\text{tot}} = (\sigma_+ + \sigma_{\text{exc}})$

As indicated in equation (4-19), this energy is used by the primaries and their secondary "progeny" to

(1) Produce ionization by the primaries. Per ionization event, this uses $U^+ + \epsilon_m$, since the new electron created has energy ϵ_m . The net energy input rate per unit volume due to ionization by primaries

$$\dot{E}_{\text{p},+} = n_n n_p v_p \sigma_+ (V_D) (U^+ + \epsilon_m) \quad (4-21)$$

(2) Excite atoms by primaries. Total energy rate per unit volume is

$$\dot{E}_{\text{p,exc}} = n_n n_p v_p \sigma_{\text{exc}} (V_D) U_{\text{exc}} \quad (4-22)$$

(a shorthand for $n_n n_p v_p \sum_j \sigma_j U_j$)

(3) Produce ionization by secondaries (Maxwellian). The rate per unit volume is

$$\dot{E}_{si} = n_n \int_0^{\infty} f_m(c) c \sigma_+(c) 4\pi c^2 dc \equiv n_n \bar{c}_e n_m \bar{\sigma}_+ \quad (4-23)$$

where $\bar{\sigma}_+ = \frac{1}{\bar{c}_e n_m} \int_0^{\infty} f_m(c) c \sigma_+(c) 4\pi c^2 dc$

and $\bar{c}_e = \sqrt{\frac{8 k T_e}{\pi m_e}}$, $n_m = \int_0^{\infty} f_m 4\pi c^2 dc$

The ionization cross-section $\sigma_+(c)$ is zero below $c^+ = \sqrt{2eU^+/m_e}$. Using a Maxwellian form for $f_m(c)$, we find

$$\bar{\sigma}_{tot} = \int_{u^+}^{\infty} e^{-u} u \sigma_+(u) du \quad (4-24)$$

where $\left(u = \frac{E}{k T_e} \right)$

and the energy spent by secondaries in ionization (per unit time and volume) is then

$$\dot{E}_{m,+} = n_n n_m \bar{c}_e \bar{\sigma}_+ (U^+ + \epsilon_m) \quad (4-25)$$

Similarly, the energy spent in excitation is

$$\dot{E}_{m,exc} = n_n n_m \bar{c}_e \bar{\sigma}_{exc} U_{exc} \quad (4-26)$$

$$n_p v_p \sigma_{\text{tot}}(V_D - \varepsilon_m) = n_p v_p \left[\sigma_+(V_D)(U^+ + \varepsilon_m) + \sigma_{\text{exc}}(V_D)U_{\text{exc}} \right] + n_m \bar{c}_e \left[\bar{\sigma}_+(U^+ + \varepsilon_m) + \bar{\sigma}_{\text{exc}}U_{\text{exc}} \right]$$

This can be solved for $\frac{n_p}{n_m}$:

$$\frac{n_p}{n_m} = \frac{\bar{c}_e}{v_p (V_D - \varepsilon_m)} \frac{U^+ + \varepsilon_m + U_{\text{exc}} \frac{\bar{\sigma}_{\text{exc}}}{\bar{\sigma}_+}}{\frac{\sigma_{\text{tot}}(V_D)}{\bar{\sigma}_+} - \frac{\sigma_+(V_D)}{\bar{\sigma}_+}(U^+ + \varepsilon_m) - \frac{\sigma_{\text{exc}}(V_D)}{\bar{\sigma}_+}} \quad (4-27)$$

Equation (4-27) is important because it expresses the ratio of primary to secondary electrons in the chamber in terms of known or measurable parameters. Note that it is a function of T_e for a fixed V_D .

Before continuing on with the derivation of ε_p , we must return to the expression for ε_o , equation (4-9). Recalling the shorthand used in equation (4-22) to represent the sum of energy levels, equation (4-9) can be written as

$$\varepsilon_o = U_+ + \frac{J_{\text{exc}}}{J_p} U_{\text{exc}} \quad (4-28)$$

Utilizing the rate per unit time and volume terms from equations (4-21), (4-22), (4-25), and (4-26), the quantity J_{exc}/J_p in equation (4-28) is

$$\frac{J_{\text{exc}}}{J_p} = \frac{J_{p,\text{exc}} + J_{m,\text{exc}}}{J_{p,+} + J_{m,+}} = \frac{n_p v_p \sigma_{\text{exc}}(V_D) + n_m \bar{c}_e \bar{\sigma}_{\text{exc}}}{n_p v_p \sigma_+(V_D) + n_m \bar{c}_e \bar{\sigma}_+} \quad (4-29)$$

Do not confuse the terminology used here. J_p represents the current of ions produced (through ionization by either by primary or secondary electrons) while $J_{p,+}$ represents the part of J_p produced by primary electrons.

Substituting equation (4-29) into equation (4-28) yields

$$\varepsilon_o = U^+ + U_{\text{exc}} \frac{n_p v_p \sigma_{\text{exc}}(V_D) + n_m \bar{c}_e \bar{\sigma}_{\text{exc}}}{n_p v_p \sigma_+(V_D) + n_m \bar{c}_e \bar{\sigma}_+} \quad (4-30)$$

and this does depend on T_e and $\frac{n_p}{n_m}(T_e)$. Substituting equation (4-27) for $\frac{n_p}{n_m}$ puts ϵ_o in terms of known or measurable parameters.

Having found an expression for ϵ_o , we can continue with determining ϵ_p^* . The expression for ϵ_p^* , equation (4-13), can be simplified by neglecting ion capture by the screen, $f_{ia}=0$, and heating power, $V_e=0$ so that

$$\epsilon_p^* = \frac{\epsilon_o + \epsilon_m}{1 - \frac{\epsilon_m}{V_D}} \quad (4-31)$$

The expression for ϵ_o , equation (4-30), can be substituted into equation (4-31). utilizing the expression for $\frac{n_p}{n_m}$, equation (4-27), and simplifying, we obtain

$$\epsilon_p^* = V_D \sigma_+(V_D) \frac{\bar{\sigma}_+(U^+ + \epsilon_m) + \bar{\sigma}_{exc} U_{exc}}{[\bar{\sigma}_{exc} \sigma_+(V_D) - \sigma_{exc}(V_D) \bar{\sigma}_+] U_{exc} + \bar{\sigma}_+ \sigma_{tot}(V_D)(V_D - \epsilon_m)} \quad (4-32)$$

NOTE: An intermediate expression for ϵ_p^* (still containing $\frac{n_p}{n_m}$), which will be useful later, is

$$\epsilon_p^* = \frac{V_D \left(\frac{\sigma_{tot}}{\sigma_+} \right) V_D}{1 + \frac{n_m}{n_p} \frac{\bar{c}_e}{v_p} \frac{\bar{\sigma}_+}{\sigma_+(V_D)}} \quad (4-33)$$

At this point we have found an expression for ϵ_p^* in terms of measurable parameters for use in defining the expression for ϵ_p , equation (4-18). The expression for ϵ_p is to be used for defining ϵ_B , equation (4-6). What remains to be found, however, is an expression for propellant utilization, η_u , present in equation (4-18).

4.2.5 Calculation of Utilization Efficiency

The derivation of the expression for propellant utilization, η_u , begins with a balance of the rate ions are produced. Specifically, the number of ions produced per second equals the rate at which primaries create ions plus the rate at which secondaries create ions. Using the ionization rates per unit volume from equations (4-21) and (4-25), this balance becomes

$$\frac{J_p}{e} = (\text{vol}) \left(n_p v_p \sigma_+ (V_D) + n_m \bar{c}_e \bar{\sigma}_+ \right) n_n \quad (4-34)$$

where $n_n = \dot{m} (1 - \eta_u) \frac{4}{\bar{c}_n \phi_n A_g m_i}$

Noticing that

$$J_B = f_B J_p = \frac{e}{m_i} \eta_u \dot{m} \quad (4-35)$$

expands equation (4-34) to

$$(\text{vol}) \left(n_p v_p \sigma_+ (V_D) + n_m \bar{c}_e \bar{\sigma}_+ \right) \frac{4(1 - \eta_u)}{\bar{c}_n \phi_n A_g} = \frac{\eta_u}{f_B} \quad (4-36)$$

But also $n_+ = n_m + n_p$ and $J_B = (0.61) e n_+ v_B A_g \phi_i$ so

$$n_m + n_p = \frac{J_B}{(0.61) e v_B A_g \phi_i} \quad (4-37)$$

Dividing the left hand side of equation (4-36) by the left hand side of equation (4-37) and the right hand side of equation (4-36) by the right hand side of equation (4-37) and simplifying yields

$$(\text{vol}) \bar{c}_e \bar{\sigma}_+ \frac{1 + \frac{n_p}{n_m} \frac{v_p (V_D) \sigma_+ (V_D)}{\bar{c}_e \bar{\sigma}_+}}{1 + \frac{n_p}{n_m}} \frac{4(1 - \eta_u)}{\bar{c}_n \phi_n A_g} = \frac{(0.61) e v_B A_g \phi_i}{J_B f_B} \eta_u \quad (4-38)$$

Equation (4-38) can be rearranged so that

$$\frac{1-\eta_u}{\eta_u} = \frac{(0.61)ev_B A_g^2 \phi_n \phi_i \bar{c}_n \left(1 + \frac{n_p}{n_m}\right)}{4(\text{vol})J_B f_B \bar{c}_e \bar{\sigma}_+ \left(1 + \frac{n_p}{n_m} \frac{v_p(V_D)}{\bar{c}_e} \frac{\sigma_+(V_D)}{\bar{\sigma}_+}\right)} \quad (4-39)$$

Notice that the bracketed term in the denominator of equation (4-39) appears in equation (4-33). Swapping out that term results in

$$\frac{1-\eta_u}{\eta_u} = \frac{(0.61)ev_B A_g^2 \phi_n \phi_i \bar{c}_n \left(1 + \frac{n_p}{n_m}\right)}{4(\text{vol})J_B f_B \bar{c}_e \bar{\sigma}_+ \left(\frac{V_D}{\epsilon_p^*} \frac{\sigma_{\text{tot}}(V_D)}{\bar{\sigma}_+} \frac{n_p}{n_m} \frac{v_p}{\bar{c}_e}\right)} \quad (4-40)$$

We can solve equation (4-40) for η_u so that

$$\eta_u = \frac{1}{1+y} \quad (4-41)$$

$$\text{where } y = \frac{0.61}{4} \frac{\epsilon_p^* ev_B A_g^2 \phi_n \phi_i \bar{c}_n \left(1 + \frac{n_p}{n_m}\right)}{(\text{vol})J_B f_B \sigma_{\text{tot}}(V_D) \left(\frac{n_p}{n_m}\right)}$$

Figure 4-2 summarizes the procedure for using Brophy's model.

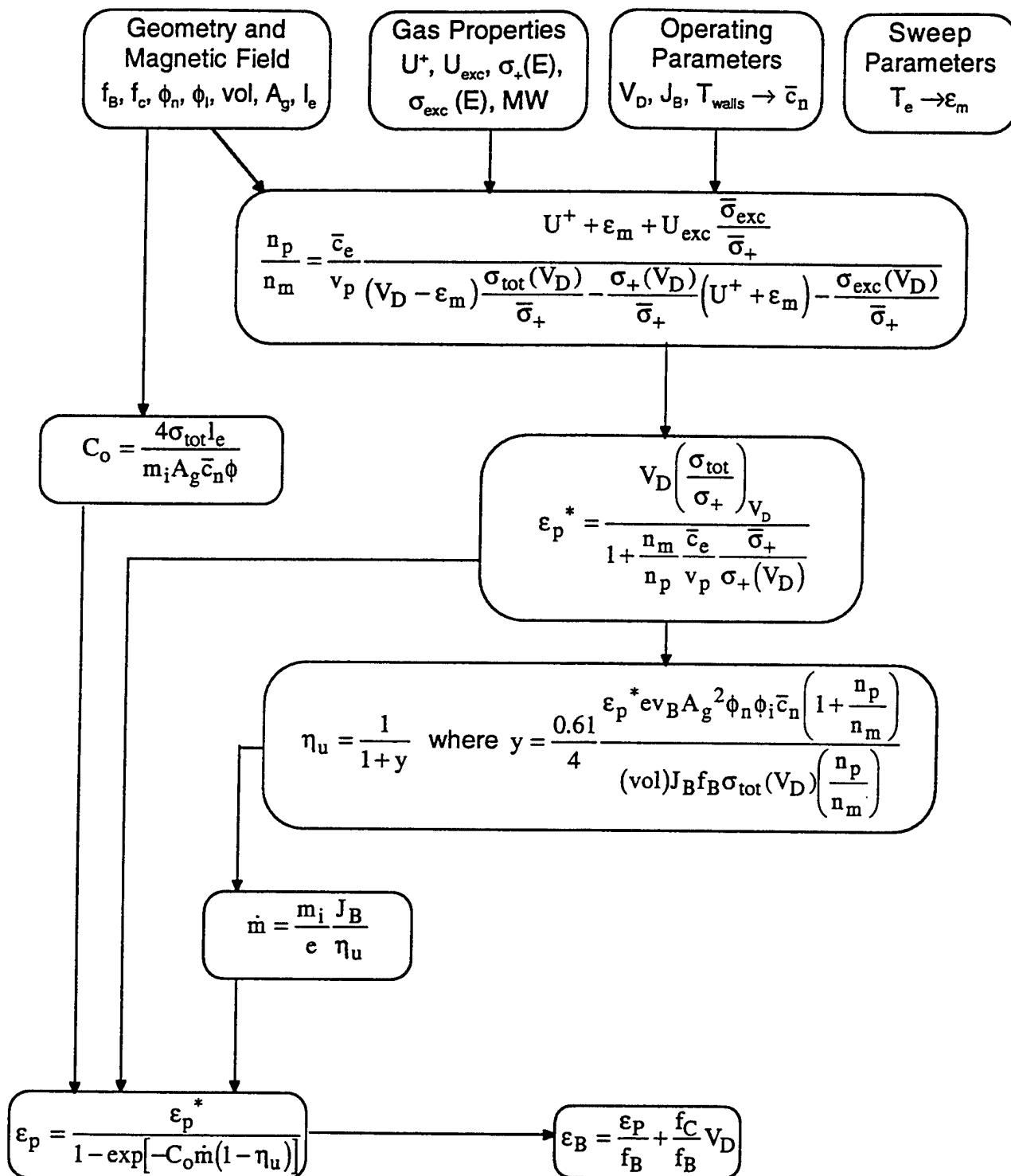


Figure 4-2 Summary of Brophy's Model

4.3 ARAKAWA ALGORITHM

In the previous section, Brophy's model was derived allowing the energy costs per beam ion, ϵ_b , to be calculated from a simple algebraic equation. Although gas properties, chamber geometry, and operating conditions are known or easily found, several important parameters must still be determined. Specifically, the pathlength of an electron, l_e , is dependent on the magnetic field within the chamber. Also, the fraction of ions reaching the beam and cathode potential surfaces, f_b and f_c respectively, are dependent on the plasma density at the surfaces. Plasma density, in turn, is partially dependent on diffusion of electrons across and along magnetic field lines. Arakawa's algorithm [3] was developed to calculate the magnetic field in the chamber and implement Brophy's model.

4.3.1 Magnetic Field Analysis

From Ampere's law we know that

$$\nabla \times \bar{B} = \mu_0 \bar{J} \quad (4-43)$$

which for the case of no current source, J , this can be expanded to

$$\nabla \times \bar{B} = \nabla \times (\nabla \times \bar{A}) = \nabla (\nabla \cdot \bar{A}) - \nabla^2 \bar{A} = 0 \quad (4-44)$$

where \bar{A} is of the magnetic potential vector. Given that the magnetic potential is divergenceless (i.e. $\nabla \cdot \bar{A} = 0$), this reduces to

$$\nabla^2 \bar{A} = 0 \quad (4-45)$$

The location and direction (N-S) of each magnet in the chamber is specified in an input file to the magnetic analysis code. The code divides the chamber into numerous triangular elements. The finite element method is applied to this grid in order to solve for the magnetic potential at each node. The magnetic field vector in cylindrical coordinates can be written as

$$\bar{B} = \nabla \times \bar{A} = \left(\frac{1}{r} \frac{\partial A_z}{\partial \theta} - \frac{\partial A_\theta}{\partial z} \right) \hat{r} + \left(\frac{\partial A_r}{\partial z} - \frac{\partial A_z}{\partial r} \right) \hat{\theta} + \frac{1}{r} \left(\frac{\partial}{\partial r} (r A_\theta) - \frac{\partial A_r}{\partial \theta} \right) \hat{z}$$

which, for the axisymmetric case, reduces to

$$\vec{B} = -\frac{\partial A_\theta}{\partial z} \hat{r} + \frac{1}{r} \left[\frac{\partial}{\partial r} (rA_\theta) \right] \hat{z} = -\frac{1}{r} \left[\frac{\partial}{\partial z} (rA_\theta) \right] \hat{r} + \frac{1}{r} \left[\frac{\partial}{\partial r} (rA_\theta) \right] \hat{z} \quad (4-46)$$

For convenience then, the magnetic analysis code outputs to a file the value of rA_θ at each node location.

4.3.2 Primary Electron Containment Length

Having calculated the value of rA_θ at each node, a Monte Carlo simulation of the electrons in the chamber is carried out. Starting from the cathode location, an electron is given an energy corresponding to the discharge voltage. Its position and velocity are surveyed as a function of time during its path through the magnetic field. Its trajectory is computed using the Runge Kutta method according to the following equations of motion while preserving angular momentum, M_θ .

$$m_e \frac{dv_z}{dt} = -ev_\theta \frac{1}{r} \frac{\partial(rA_\theta)}{\partial r} \quad (4-47)$$

$$m_e \frac{dv_r}{dt} = m_e \frac{v_\theta^2}{r} - ev_\theta \frac{1}{r} \frac{\partial(rA_\theta)}{\partial r} \quad (4-48)$$

$$M_\theta = m_e r v_\theta - e r A_\theta = \text{constant} \quad (4-49)$$

While in the chamber, a probability exists that the electron will have its trajectory altered either by an elastic collision with a neutral atom or by the "wave" of the oscillating plasma. These probabilities are calculated from the mean free paths of the respective phenomena. The electron continues until it reaches the anode location. The path lengths of the several thousand electrons simulated are averaged to yield the primary electron confinement length, l_e needed in Brophy's model. The time the electrons spend in each triangular grid element is totaled to provide the distribution of primary electrons within the chamber. Because the simulation is estimating the electron path length assuming ionization does not occur, no secondary electrons are created (see section 4.2.3).

4.3.3 Discharge Chamber Performance

Having found the electron densities, the Arakawa algorithm proceeds to determine the plasma distribution in the chamber. The governing equation for the particle balance within the chamber is

$$-\nabla \cdot ([\bar{D}][\nabla n]) = \dot{Q} \quad (4-50)$$

where \bar{D} describes the spatial variation of the diffusion coefficients parallel and normal to the magnetic field lines and \dot{Q} is the ion production rate per unit volume. Reference [3] provides a fuller development of those terms. The result is the differential equation

$$\frac{1}{r} \frac{\partial}{\partial r} \left(D_{22} r \frac{\partial n}{\partial r} + D_{21} r \frac{\partial n}{\partial z} \right) + \frac{\partial}{\partial z} \left(D_{12} \frac{\partial n}{\partial r} + D_{11} \frac{\partial n}{\partial z} \right) + \dot{Q} = 0 \quad (4-51)$$

where

$$D_{11} = D_P \cos^2 \theta + D_N \sin^2 \theta$$

$$D_{22} = D_P \sin^2 \theta + D_N \cos^2 \theta$$

$$D_{12} = D_{21} = (D_P - D_N) \sin \theta \cos \theta$$

and D_P and D_N are diffusion coefficients parallel and normal to magnetic field lines, respectively. Plasma density within the chamber is found by solving equation (4-51).

The ion flux to surfaces is assumed to be proportional to plasma density at that area. Knowing the plasma density along the exit and cathode potential surfaces, the fraction of ions to these regions, f_B and f_c respectively, can be calculated. The values for I_e , f_B , f_c are used together with other chosen or constant values in Brophy's model to calculate the energy cost per beam ion, ϵ_B .

Figure 4-3 summarizes Arakawa's algorithm.

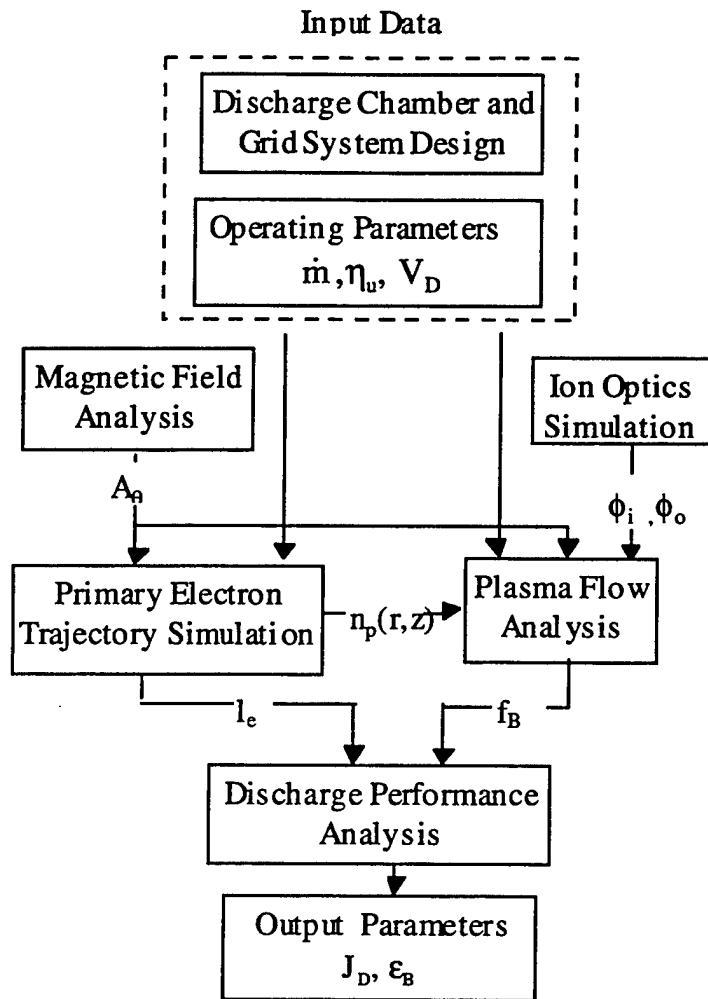


Figure 4-3 Summary of Arakawa Algorithm

4.4 SUMMARY

In this chapter, the model used to predict the performance of ring-cusped ion engines was derived. It was shown that energy cost per beam ion, ϵ_B , can be formulated as a simple algebraic equation known as Brophy's model. Most of the parameters in Brophy's model are known a priori given the choice of propellant gas, chamber geometry, and operating conditions. The remaining parameters can be determined using Arakawa's algorithm the fundamentals of which were also described in this chapter. The next chapter uses this model to

examine how performance of cylindrical ion engines changes as their scale is reduced several orders of magnitude.

References

1. Brophy, J.R., Wilbur, P.J., "Simple Performance Model for Ring and Line Cusp Ion Thrusters" AIAA Journal pp. 1731-1736, 23 No. 11, Nov. 1985.
2. Martinez-Sanchez, M., Course Handout: 16.522 Space Propulsion, Fall 1995, MIT.
3. Arakawa, Y., Ishihara, K., "A Numerical Code for Cusped Ion Thrusters." IEPC-91-118, 22nd International Electric Propulsion Conference, Oct. 14-17, 1991, Viareggio, Italy.

Chapter 5

Scaling of Cylindrical Ion Engines

The previous chapter formulated Brophy's model and outlined Arakawa's code which implements the model. The code is discussed first with an emphasis on the formulations used to simulate particle behavior within the chamber. This is important because of the assumption in subsequent analysis that the physics remain the same at smaller scales. Next, an argument is outlined as to how thruster parameters such as mass flow rate and discharge voltage should change as thruster size is scaled. The effect on performance of scaled cylindrical ion thrusters is then presented.

5.1 SCALING ARGUMENT

This section examines how each of the input parameters to the Arakawa code should scale in order to maintain the same discharge chamber performance as chamber size is reduced. As developed in Chapter 4, the average beam ion energy cost is given as

$$\epsilon_B = \frac{\epsilon_P^*}{f_B \{1 - \exp[-C_o \dot{m}(1 - \eta_u)]\}} + \frac{f_C}{f_B} V_D \quad (5-1)$$

where $C_o = 4\sigma_e l_e / ev_o A_g \phi_o$ and \dot{m} is the mass flow rate per chamber in Aeq/s. Equation (5-1) indicates that it is desirable to maximize the value of the primary electron containment length, l_e , in order to reduce the power needed to create beam ions. In other words, the longer an average primary electron remains in the chamber before being lost to the anode, the more effective ionizer it is and the more efficient the

thruster will be. Ring and line cusped ion engines increase I_e by employing magnets which cause the electrons to spiral around magnetic field lines.

Equation (5-1) also indicates that it is desirable to maximize the fraction of ions reaching the beam, f_b , and minimize the fraction of ions reaching cathode potential surfaces, f_c . In a well-designed chamber, the presence of a magnetic field tends to contain the primary electrons near the center of the chamber. Because a higher percentage of ionizations occur near the chamber center and the ion's ability to diffuse across field lines is hindered, f_b increases and f_c decreases yielding improved performance.

As the size of the thruster is decreased, the chamber exit area will scale as $A_g \sim L^2$ where L is a characteristic length. To maintain the same energy cost per beam ion as chamber size is scaled, equation (5-2) suggests that the primary electron confinement length and mass flow rate should scale as $l_e \sim L$ and $\dot{m} \sim L$.

Maintaining I_e proportional to a characteristic chamber length should be a matter of keeping the same "degree of particle interaction" between the electrons, neutrals, and ions. Ideally this would be accomplished by altering the magnetic field strength and particle densities so that the Larmor radius and mean free paths scale as L . Magnetic field strength, B , and Larmor radius are related by

$$B = \frac{m_e v_p}{er_L} \quad (5-2)$$

Equation (5-2) implies that $B \sim 1/L$ since m_e and e are constants and v_p is proportional to $\sqrt{V_D}$ which is assumed invariant. The mean free paths for elastic collisions of electrons with neutrals and ions, inelastic ionizing collisions with neutrals, and electron-wave interactions due to plasma oscillations are, respectively

$$\lambda_{e-n} = \frac{1}{n_o \sigma_{e-n}} \quad (5-3)$$

$$\lambda_{e-i} = \frac{4.5 \times 10^{16} V_D^2}{n_+} \quad (5-4)$$

$$\lambda_{ion} = \frac{1}{n_o \sigma_+} \quad (5-5)$$

$$\lambda_{anom} = 2\pi \left(\frac{2\epsilon_o}{e} \frac{V_D}{n_+} \right)^{1/2} = 2\pi \lambda_d \quad (5-6)$$

where $n_+ = n_p + n_m$ since a primary electron is assumed to become a secondary electron after colliding with a neutral to form an ion. For the mean free paths to scale as L , equations (5-3) through (5-5) require that the neutral and ion densities scale as $n_o \sim 1/L$ and $n_+ \sim 1/L$. With $n_+ \sim 1/L$ equation (5-6) indicates that λ_{anom} does not scale as L but as \sqrt{L} with the result being that electron-wave interactions occur less frequently as size is reduced. Although equation (5-6) represents the anomalous mean free path used in Arakawa's primary electron trajectory simulation, it may not be appropriate under the assumption under Bohm diffusion. In such a case, $\lambda_{anom} \sim r_{Larmor} = m_e c / eB$ so that $\lambda_{anom} \sim L$, not \sqrt{L} . In this analysis however, equation (5-6) is used.

We see that $n_o \sim 1/L$ is consistent with $\dot{m} \sim L$ since

$$n_o = \frac{4\dot{m}(1-\eta_u)}{m_i v_n A_g \phi_o} \quad (5-7)$$

That $n_+ \sim 1/L$ is consistent with $\dot{m} \sim L$ since

$$J_B = \dot{m} \eta_u = 0.61 (n_+ v_B A_g \phi_i) \quad (5-8)$$

where $A_g \sim L^2$ and v_B is proportional to $\sqrt{T_e}$ which is assumed invariant. It is also desired that the propellant utilization, η_u , remain invariant. Propellant utilization can be represented as formulated in Chapter 4

$$\eta_u = 1 / \left(1 + \frac{0.15 e \epsilon_p^* v_B A_g^2 \phi_i \phi_o \bar{c}_n \left(1 + \frac{n_p}{n_m} \right)}{J_B f_B V_D v_p (Vol) \sigma_T \left(\frac{n_p}{n_m} \right)} \right) \quad (5-9)$$

where $v_p \sim \sqrt{V_D}$, $\bar{c}_e \sim \sqrt{T_e}$ and $v_B \sim \sqrt{T_e}$ and so remain invariant given the assumptions that T_e and V_D are invariant. Additionally, $A_g \sim L^2$, $J_B \sim L$ and $Vol \sim L^3$. η_u , then, will remain invariant only if the ratio of primary to secondary electrons, n_p/n_m , and baseline energy cost per ion, ϵ_p^* , are invariant. n_p/n_m and ϵ_p^* can be calculated, respectively, as

$$\frac{n_p}{n_m} = \left(\frac{\bar{c}_e}{v_p} \right) \left(\frac{U^+ + \epsilon_m + U_{exc} \left(\frac{\bar{\sigma}_{exc}}{\bar{\sigma}_+} \right)}{(V_D - \epsilon_m) \left(\frac{\sigma_T}{\bar{\sigma}_+} \right) - \left(\frac{\sigma_+}{\bar{\sigma}_+} \right) (U^+ + \epsilon_m) - \frac{\sigma_{exc}}{\bar{\sigma}_+}} \right) \quad (5-10)$$

and

$$\epsilon_p^* = \frac{V_D \left(\frac{\sigma_T}{\bar{\sigma}_+} \right)}{1 + \frac{n_m}{n_p} \frac{\bar{c}_e}{v_p} \frac{\bar{\sigma}_+}{\sigma_+}} \quad (5-11)$$

Therefore, n_p/n_m and ϵ_p will remain invariant if \bar{c}_e is invariant. \bar{c}_e is given by

$$\bar{c}_e = \sqrt{\frac{8}{\pi} \frac{e}{m_e} T_e} \quad (5-12)$$

indicating that it is consistent for η_u and T_e to simultaneously remain invariant as thruster scale is reduced. A more general scaling argument for electric thrusters is given by Khayms in reference [1].

A 10 cm diameter ion thruster typically utilizes permanent magnets which produce a 0.1 T magnetic field near the magnet face. Scaling the thruster to a diameter of approximately 1 cm requires a 1 T magnetic field which may be achieved using rare-earth ceramic magnets. Achieving the 10 T field strength necessary for a 1 mm size microthruster would presumably require superconducting wire solenoids to avoid ohmic losses (and subsequent thermal issues) in the wires.

5.2 SCALING OF CYLINDRICAL CHAMBERS

The analytic code described in Chapter 4 was used to determine the effect that scaling has on discharge chamber performance. The magnetic analysis part of the code was found to produce erroneous results. In accordance with Gauss's Law, the magnetic flux through a closed surface should equal zero,

$$\oint \vec{B} \cdot d\vec{A} = 0 \quad (5-13)$$

However, performing this check with the field generated by Arakawa's magnetic field program yielded integrations differing significantly from zero. This indicates a flaw in the calculation of the magnetic potential. Therefore, a commercial package known as MAGNETO [2] was used in its place.

A 7cm ion thruster developed at Colorado State University was chosen as a baseline because it has undergone experimental testing and numerical simulation [3]. The chamber geometry with corresponding field lines and flux density contours calculated by MAGNETO are shown in Figure 5-1 and

Figure 5-2 respectively. Magnetic flux density was held at 1200 G at the magnet surfaces (representative of SmCo magnets) for all cases.

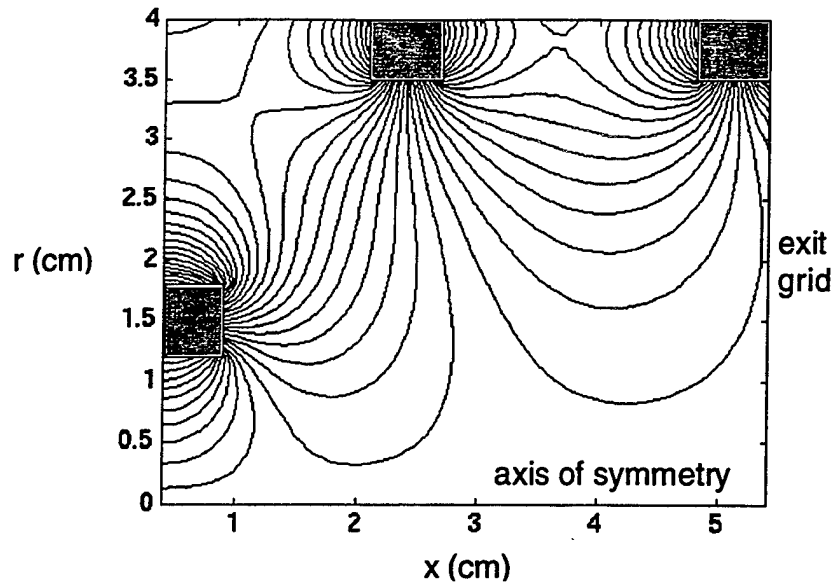


Figure 5-1. 7cm CSU magnetic potential contours.

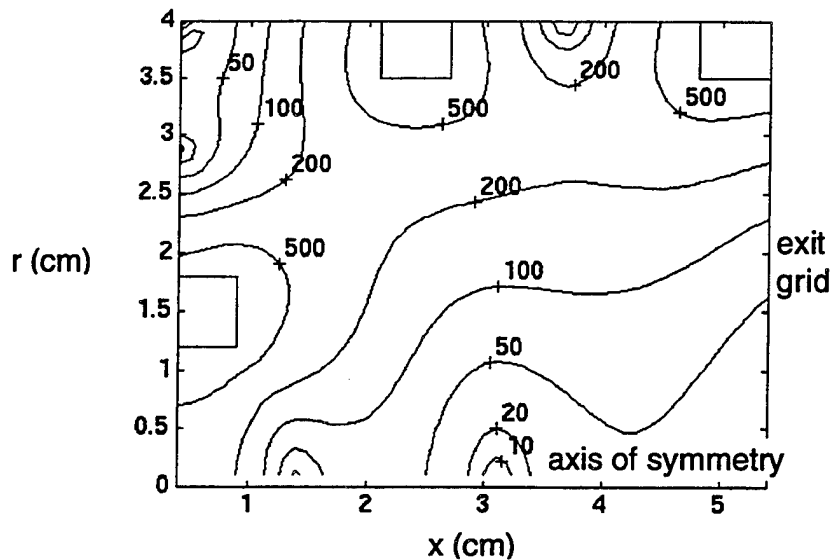


Figure 5-2. 7cm CSU flux density contours (Gauss units).

The structural, material, and power resources required to produce magnetic field strengths of several Tesla in the chamber of an ion microthruster are not yet available. Therefore, the effect of scaling a chamber while holding the permanent magnet surface strength constant at that of the 7cm chamber was investigated. Many of the

relationships presented in the previous section will not hold since the magnetic flux density will not scale proportional to $1/L$.

Figure 5-3 shows beam ion production cost, ϵ_B , as a function of propellant utilization for cylindrical chamber diameters ranging from 7cm to 0.07cm. Despite best efforts, the values for the 7cm case differ significantly from those obtained in reference [4]. The higher ϵ_B calculated for this paper are due to a lower fraction of ions reaching the beam ($f_B=0.21$ vs. 0.29 in Ref. [3]). This discrepancy is probably due to differences in the magnetic field as generated by MAGNETO and Arakawa's magnetic field analysis program. Arakawa's program overstates the strength of the magnetic field resulting in a higher concentration of ions near the chamber center. Consequently, Arakawa's program predicts a larger fraction of these ions reaching the beam. Although the values of ϵ_B in this analysis do not agree with experimental data, it is still possible to identify the factors influencing ϵ_B as chamber size is scaled.

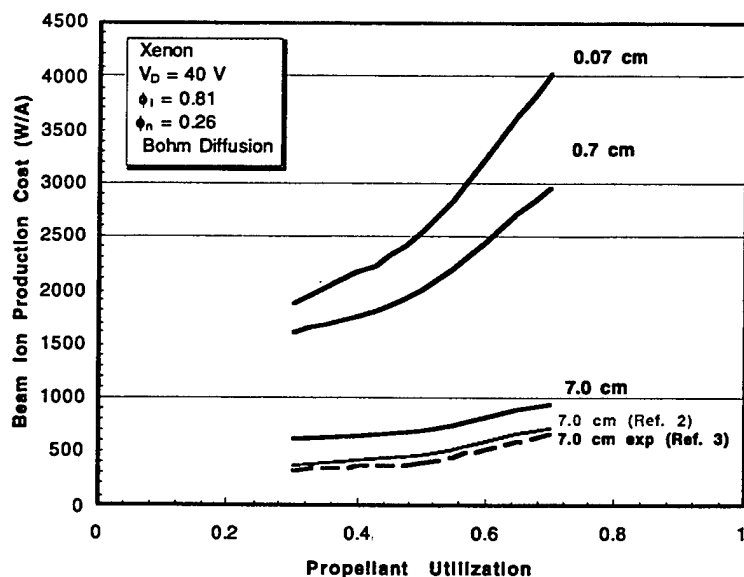


Figure 5-3. ϵ_B vs. η_U .

The results of scaling the 7cm CSU ion thruster as generated by the Arakawa code are listed in Table 5-1. Mass flow rate was initially set at 0.15 Aeq consistent with it's

operation at CSU. The neutral density scales as $1/L$ as expected due to the scaling of mass flow rate as L . Due to the lack of a magnetic field the primary electron confinement length scales greater than L . This results in proportionately less ionization so that ion density scales less than proportional to $1/L$. The equilibrium temperature does not, therefore, remain invariant but increases slightly as the thruster is scaled down.

Figure 5-4 shows the distribution of primary electrons in the 7cm chamber. The peak electron density occurs at the position of the cathode. As shown in the figure, the magnetic field tends to contain the primary electrons near the chamber center. Ionizations will then also tend to occur near the chamber center resulting in a plasma density distribution as shown in Figure 5-5. A large fraction of ions, f_B , reaches the beam tending to improve performance. Note the sharp increase in ϵ_B as L decreases indication larger wall losses.

Table 5-1. Scaling of 7cm CSU ion thruster ($\eta_u=0.7$)

	units	L	0.1L	0.01L	Scales as
d_B	m	0.07	0.007	0.0007	L
\dot{m}	$(Aeq)^{-1}$	0.15	0.015	0.0015	L
$\min r_i$	m	$1.8e-4$	$1.8e-4$	$1.8e-4$	1
λ_{e-n}	m	1.01	0.101	0.0101	L
λ_{e-i}	m	334.0	34.1	3.44	$\approx L^{0.99}$
λ_{ion}	m	4.7	0.47	0.047	L
λ_{anom}	mm	$9.0e-4$	$2.8e-4$	$9.1e-5$	\sqrt{L}
I_e	m	2.09	0.076	0.00629	$\approx L^{1.26}$
C_n	$(Aeq)^{-1}$	12.5	46.4	376.0	$\approx L^{-0.73}$
n_0	$10^{18}/m^3$	4.76	47.6	476.0	$1/L$
n_+	$10^{18}/m^3$	0.130	1.25	12.7	$\approx L^{-0.99}$
n_0	$10^{18}/m^3$	0.0206	0.310	3.53	$\approx L^{-1.11}$
f_B	unitless	0.21	0.14	0.12	$\approx L^{0.12}$
f_C	unitless	0.79	0.86	0.88	$\approx L^{-0.02}$
T_e	eV	3.61	3.78	3.82	$\approx L^{-0.01}$
ϵ_n	W	70.4	72.5	73.1	$\approx L^{-0.01}$
ϵ_B	W	940	2963	4029	$\approx L^{-0.31}$

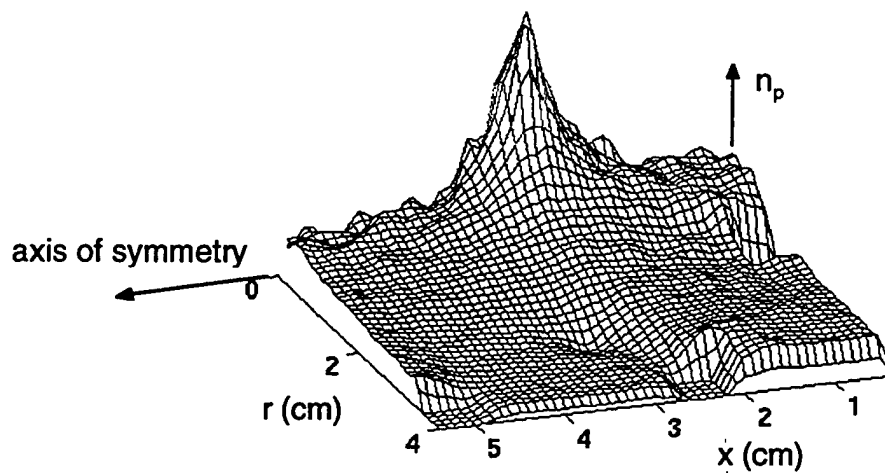


Figure 5-4. Primary electron densities for 7cm chamber.

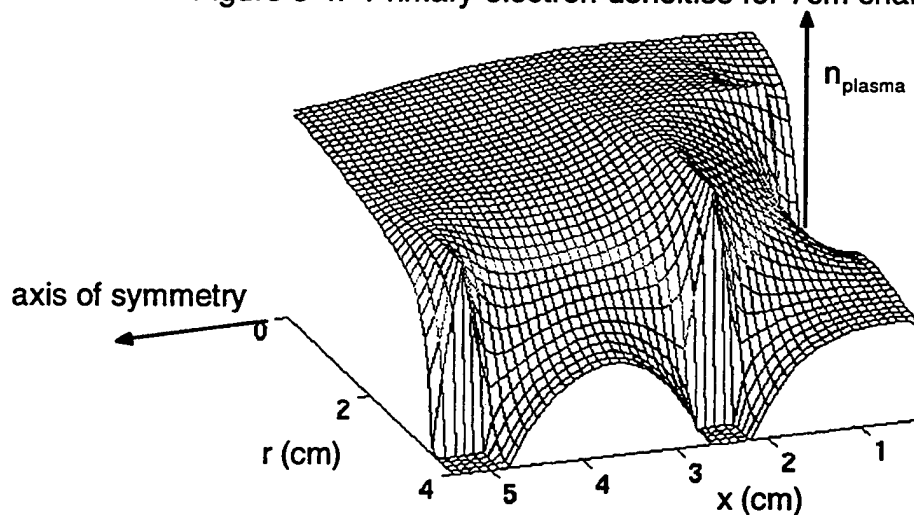


Figure 5-5. Plasma densities for 7cm chamber.

Because the strength of the magnetic field can not be increased as chamber size is scaled down, the Larmor radius increases relative to the size of the chamber. The primary electrons can easily cross field lines reaching all regions of the chamber. For the 0.7cm and 0.07cm cases then, ionization occurs more uniformly. The resulting plasma density distributions are shown in Figure 5-6 and Figure 5-7. A lower fraction of ions reach the beam leading to decreased performance as compared to the 7cm case.

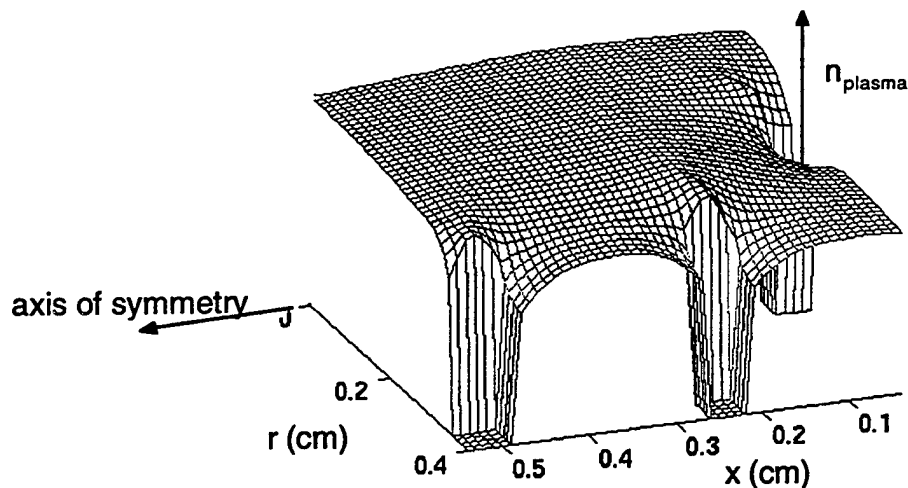


Figure 5-6. Plasma densities for 0.7cm chamber.

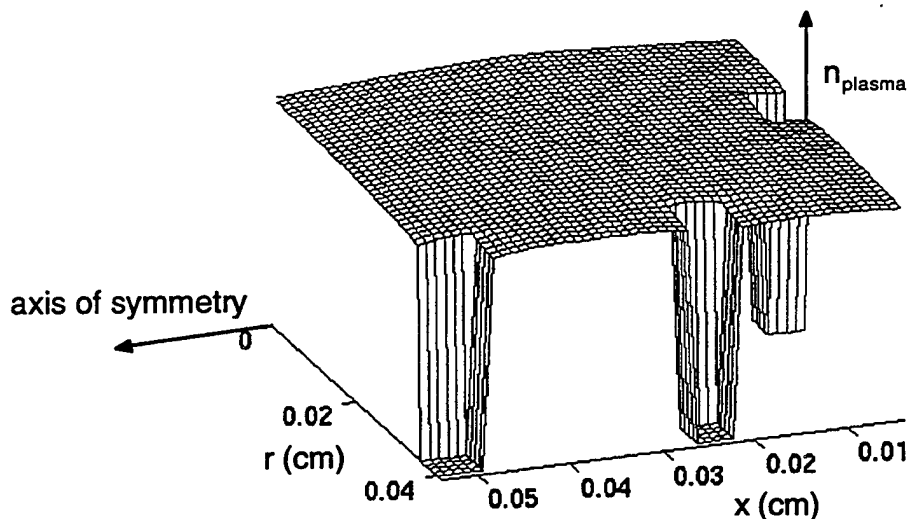


Figure 5-7. Plasma densities for 0.07cm chamber.

For the cylindrical geometry analyzed here the ratio of exit area to total chamber surface area is 0.11. It is clear from Table 5-1 that as chamber size is scaled down the fraction of ions reaching the beam approaches the 0.11 value. This indicates that the magnetic field does not significantly confine the electrons or ions at the smallest scales.

5.3 SUMMARY AND CONCLUSIONS

This chapter examined possible design considerations for ion microthrusters. It was shown that, although desirable, magnetic fields can not be scaled inversely

proportional to the chamber scale. Even the best practical permanent magnets provide little electron or ion containment below chamber sizes of ~ 1 mm. At those scales the fraction of ions which reach the beam is essentially the ratio of the chamber exit area to the total chamber area. The next chapter applies these findings to the concept of a linear ion microthruster.

References

1. Khayms, Vadim, "Design of a Miniaturized Hall Thruster for Microsatellites." M.S. Thesis, Massachusetts Institute of Technology, May 1997.
2. MAGNETO by Integrated Engineering Software Inc. 46-1313 Border Place Winnipeg, Manitoba, Canada R3H0X4, <http://www.integrated.mb.ca/ies>
3. Vaughn, J.A., and Wilbur, P.J., "Ring Cusp/ Hollow Cathode Discharge Chamber Performance Studies." IEPC-88-064, 20th International Electric Propulsion Conference, Garmisch-Partenkirchen, W. Germany, Oct. 3-6, 1988.
4. Arakawa, Y., Ishihara, K., "A Numerical Code for Cusped Ion Thrusters." IEPC-91-118, 22nd International Electric Propulsion Conference, Oct. 14-17, 1991, Viareggio, Italy.

This page intentionally left blank

Chapter 6

Design Considerations for the Linear Ion Microthruster

In the previous chapter, the performance of cylindrical ion engines as they are scaled down three orders of magnitude was examined. It was found that magnetic field strengths typical of permanent magnets had no effect on electron or ion containment below diameters of 0.1mm. This resulted in the fraction of ions reaching the beam and cathode potential surfaces equaling the respective surface area fractions. This result will be exploited to forego consideration of magnetic fields in analysis of the linear ion microthruster concept.

6.1 INTRODUCTION TO THE LINEAR ION MICROTHRUSTER

The linear ion microthruster, shown in Figure 6-1, is a concept for a micro-machined ion propulsion system proposed by members of the Jet Propulsion Laboratory [1]. The ends of the chamber are not pictured in Figure 6-1 in order to provide an unobstructed view of the inside. The thruster consists of several linear discharge chambers situated parallel to each other. Each discharge chamber has dimensions of approximately $100\mu\text{m} \times 300\mu\text{m} \times 10\text{cm}$ although these sizes are only conceptual. The walls separating the discharge chambers are built up from alternating layers of conducting and insulating materials. Contained within these walls is the ion accelerator system which includes the ion accelerator grid and the ion decelerator grid separated by layers of spray coated aluminum oxide of sufficient thickness to stand off the high voltages applied between the layers. Electrons stripped from the propellant in the

ionization process are collected by the anode and injected into the ion beam by an external neutralizer. The linear ion microthruster concept, as currently conceived, does not contain an exit grid. Design of the ion acceleration region is currently ongoing at the Jet Propulsion Lab. Consequently, the transparency of the exit region to ions and neutrals is not known with certainty. In this chapter then, analysis is first performed assuming transparencies typical of traditional ion engines (i.e. $\phi_i=0.86$ and $\phi_o=0.26$, ref. [2]). Next, the analysis is repeated with ions and neutrals treated as though they can pass unhindered through the exit (i.e. $\phi_i=1$ and $\phi_o=1$).

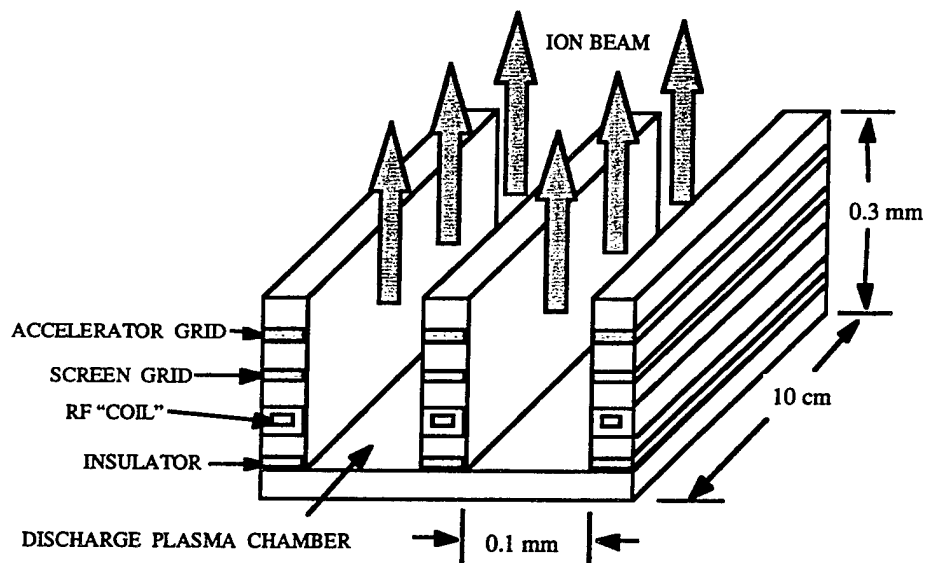


Figure 6-1. Linear Ion Microthruster

Brophy's model, as formulated in Chapter 4, will be applied in the analysis of this concept. The performance of an ion thruster is gauged by the power required to produce, but not accelerate, an ion which eventually becomes part of the beam. The average energy cost to produce a single beam ion, ϵ_B , is a key parameter in the measure of the thruster's performance. To produce a more efficient thruster, it is necessary to reduce the value of ϵ_B while striving to maintain a high propellant utilization.

6.2 PERFORMANCE OF LINEAR GEOMETRY

The results of the previous chapter demonstrated that as size is scaled down several orders of magnitude the plasma density becomes uniform. Therefore, the problem of finding the fraction of ions reaching the beam and cathode potential surfaces, f_b and f_c respectively, is a simple one to solve. Their values correspond to the surface area ratios of the beam and walls. What does remain to be found, however, is the primary electron confinement length, l_e .

6.2.1 Determination of Electron Confinement Length

Arakawa's primary electron trajectory simulator was modified to accommodate rectilinear geometries. Electron trajectories were simulated over a range of chamber height, width, and lengths to determine electron confinement lengths for each case. Cathode position was assumed to be located at the center of the chamber floor. For a given chamber width to height ratio, w_c/h_c , confinement length was found to be independent of chamber length, L_c . Although contrary to intuition, the reason for this can be seen in Figure 6-2 which shows an electron trajectory for a linear chamber. If the anode is located in the sidewall along the length of the chamber, then the path of the electron (dotted line) before it reaches the anode will be the same regardless of chamber length, L_c .

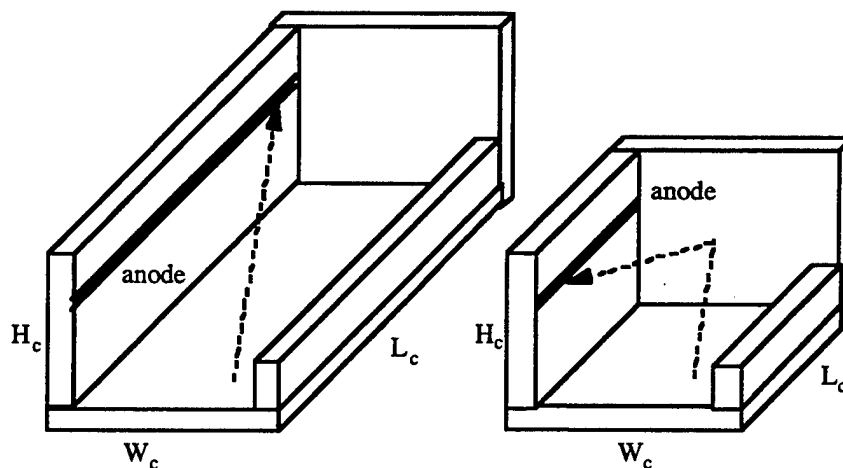


Figure 6-2. Sample Electron Trajectories in Linear Chamber

The anode was positioned halfway up the wall with a constant width of $10\mu\text{m}$. All electrons are assumed to reflect specularly off the electrostatic sheaths surrounding the chamber surfaces and be captured upon reaching the anode. Arakawa's electron trajectory simulation showed confinement length varying with chamber width to height ratio as shown in Figure 6-3.

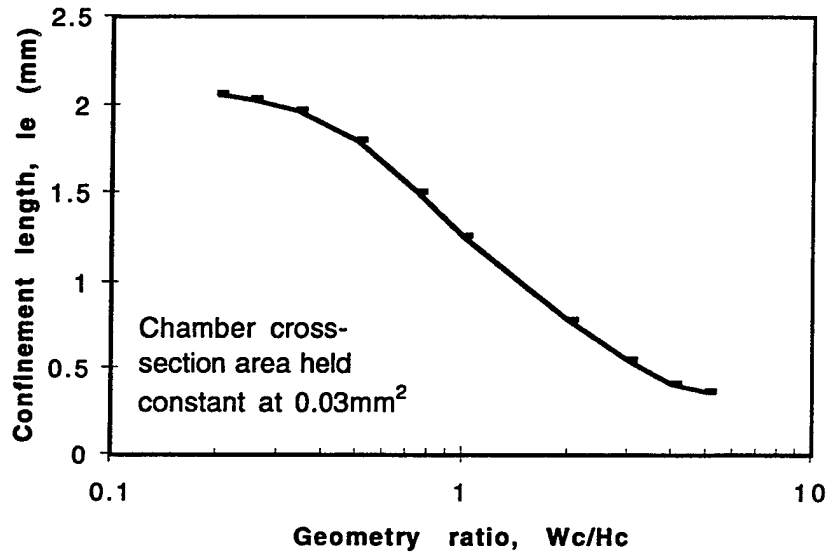


Figure 6-3. Variation of Electron Confinement Lengths with w_c/h_c

From Figure 6-3 it can be seen that the confinement length is several times the chamber dimensions due to reflection off the walls prior to being captured by the anode. Further the confinement length decreases as chamber width to height ratio increases. Because the anode is located halfway up the wall, electrons in tall, narrow (i.e. low w_c/h_c) chambers tend to bounce from sidewall to sidewall many times before reaching the anode. The optimal confinement length of 2.1mm appears to occur at a geometry ratio of 0.2. This corresponds to chamber height and width equal to 0.387mm and 0.077mm, respectively.

6.2.2 Energy Costs per Beam Ion

The value of l_e , found in the previous section is now used in Brophy's model to optimize the linear microthruster geometry in terms of height, width, length, and

number of chambers. Operating parameters were assumed to be consistent with those necessary for a 5 kg microspacecraft orbiting as part of a distributed satellite system. In Chapter 3, it was found that the maximum tidal accelerations encountered by such a "swarm" of spacecraft would be on the order of 0.001 m/s². Further it was shown that the specific impulses required are typical of those generated by ion engines.

Figure 6-4 presents the methodology used to analyze the performance of the linear configuration. Assuming a total thrust, F_{tot} , of 5 mN and a specific impulse of 3300s, the total mass flow rate is 0.162 A-eq. Knowing the chamber width, length and grid spacing, the allowable mass flow rate per chamber can be calculated from the Child-Langmuir 1-D space charge limit (SCL)

$$\dot{m}_{ion} = \frac{F_{tot}}{I_{sp}g} = \frac{4}{9}\epsilon_o \left(\frac{2m_{ion}}{e} \right)^{1/2} \left(\frac{V_{tot}^{3/2}}{s_{grid}^2} \right) (A_c N_c) \quad (6-1)$$

where A_c and N_c are the chamber exit area and number of chambers, respectively. Then s_{grid} is the gap spacing across which the ion beam is accelerated. The value of s_{grid} for the linear ion microthruster is ambiguous since no grid physically exists at the exit. As mentioned earlier, the design of the ion acceleration region is currently under development. Therefore, for this analysis, it will be assumed that the electric potential which accelerates the ions, V_{tot} , is distributed uniformly between the side walls across a gap measuring s_{grid} . Allowable mass flow per chamber can be divided into the total mass flow for the thruster yielding the required number of chambers. Values of T_e and ϵ_p^* were determined through an iterative process based on the energy equilibrium in the discharge chamber.

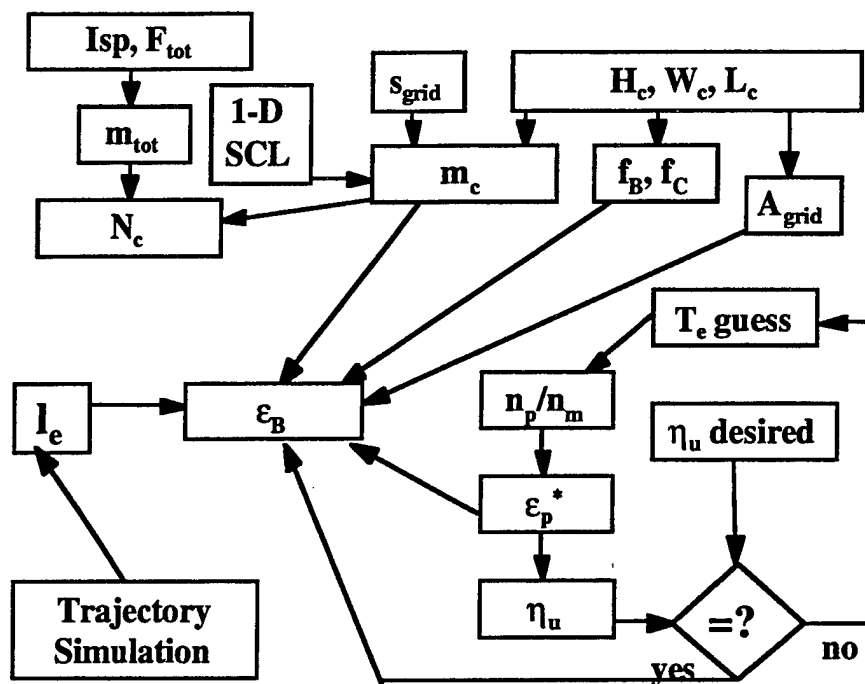


Figure 6-4. Linear analysis methodology.

Figure 6-5 shows the variation of beam ion production cost with chamber length for the case where transparencies to ions and neutrals are chosen to be 0.81 and 0.26, respectively. The ion acceleration region was limited to values greater than 10 microns. The height and width of all chambers remained constant at 0.39 mm and 0.077 mm, respectively. At a chamber length of 0.70 mm, 15 chambers were required to satisfy space charge limitations. As length increased, fewer chambers were required to provide the necessary mass flow rate. Beam ion production costs tends to decrease as the number chambers decreases. For a given number of chambers, however, beam ion production cost increases as length increases. This is due to an increase in exit area with no increase in mass flow rate per chamber. The trend of a slightly decreasing beam ion cost reverses dramatically once less than three chambers are needed. For that situation, beam ion cost jumps from 1000 to 5000 W/A as the length of the chamber increases. For relatively short chambers (on the order of chamber height and width), edge effects will become significant. In this analysis, however, no attempt was made to model the effect.

The beam ion production costs in the range of 1100 to 5000 W/A shown in Figure 6-5 are several times higher than typical large ion engines. This is due, in part, to a confinement length approximately eight times chamber dimensions. This value encompasses the ability of the electron to reflect off walls while still retaining enough energy to ionize neutrals. However, such confinement lengths are well below those of large ion engines (typically 20-40 times chamber dimensions)

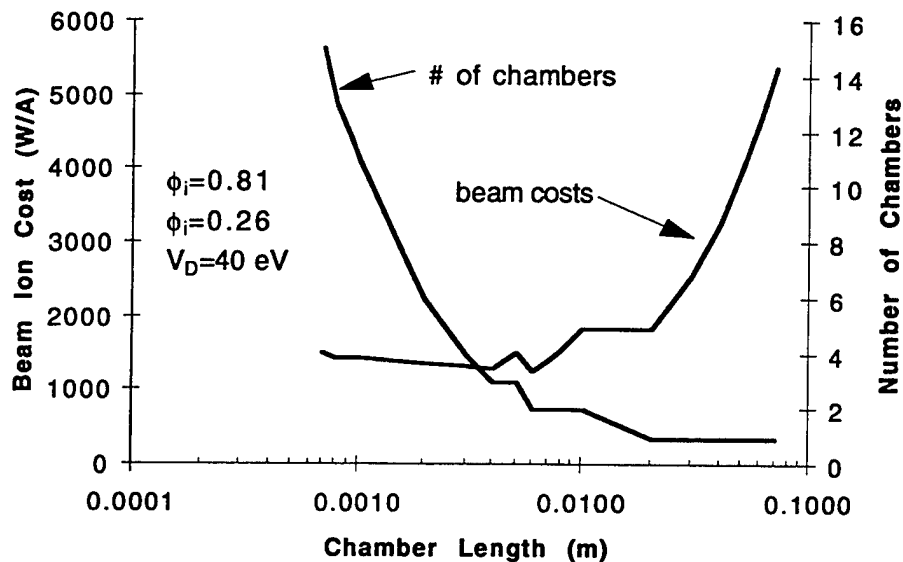


Figure 6-5. Relationship between beam cost and number of chambers.

Figure 6-6 presents analysis similar to that just performed except that it is assumed the chamber exit conditions do not hinder the passage of ions or neutrals (i.e. $\phi_i=1$ and $\phi_o=1$). The lower neutral density in the chamber results in a jump in beam ion production cost. Again it can be seen that beam costs decreases slightly as the number of chambers decreases. Optimum beam ion costs occurs at 2 chambers. For a given number of chambers, beam ion costs increases as chamber length increases.

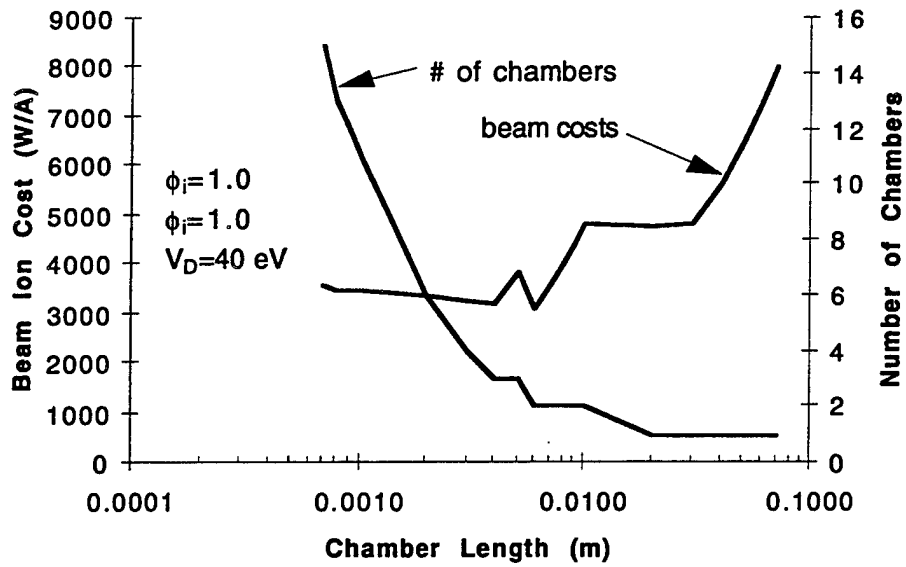


Figure 6-6. Beam ion energy cost vs. chamber length

6.2.3 Mapping Ion Energy Cost to Efficiency

Before the performance of the linear microthruster can be compared to other systems in terms of propulsion system power and mass, it is necessary to put the cost per beam ion value in terms of a more easily used parameter, namely thruster efficiency, η .

In more general terms, ϵ_B can be thought of as

$$\epsilon_B = \frac{\text{Total Power} - \text{Useful Power}}{J_B} \quad (6-2)$$

where, from Chapter 4, useful power = $J_B(V_D + V_{net})$ and total power = P_{in} .

Substituting P_{in} from equation (6-2) and with $P_{beam} = J_B V_{net}$, the efficiency, η , of the thruster can then be related as:

$$\eta = \frac{P_{beam}}{P_{in}}$$

$$\eta = \frac{V_{net}}{V_D + V_{net} + \epsilon_B}$$

$$\eta = \frac{1}{1 + \frac{(V_D + \epsilon_B)2e}{(g_0 I_{sp})^2 m_i}} \quad (6-3)$$

Figure 6-7 shows efficiencies plotted versus specific impulse as calculated using equation (6-3) for several values of ϵ_B .

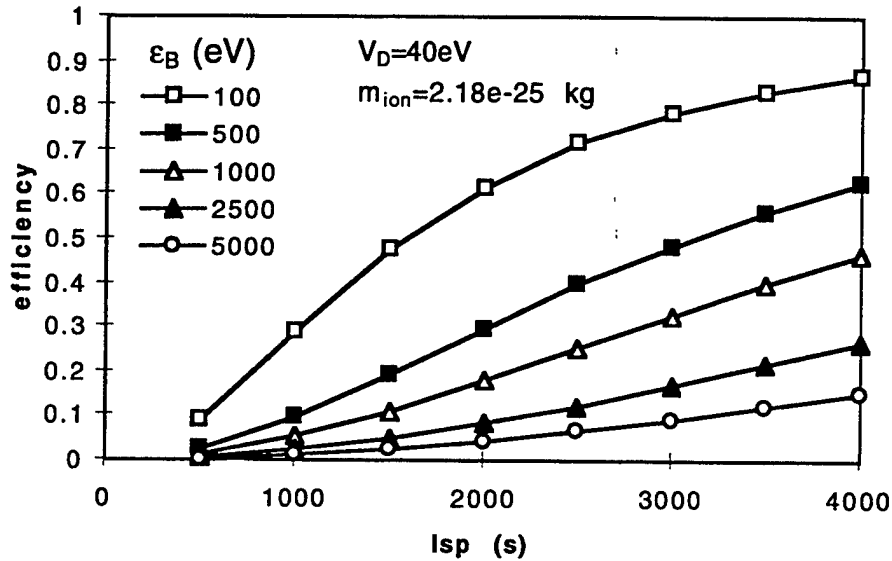


Figure 6-7. η vs. I_{sp} at Several ϵ_B

6.3 LINEAR ION MICROTHRUSTER VS. COLD GAS THRUSTER

To gauge the performance of the linear ion microthruster, a comparison is made with a hypothetical cold gas microthruster for a range of thrust times. Using equation (6-3) the lowest ϵ_B in Figure 6-6 corresponds to an efficiency $\eta=16\%$. The cold gas thruster is assumed to operate at a $I_{sp} = 75$ s. The specific power of the ion thruster power plant is assumed to be 10 W/kg. The mass of both the cold gas and linear ion microthrusters are assumed to be negligible compared with the mass of any propellant or power plant required.

Figure 6-8 shows how propulsion system mass varies with thrusting time. For short thrusting times, the mass is due almost exclusively to its large power system. The

efficiency of the linear ion microthruster is so poor that just the power plant makes up approximately 55% of the spacecraft mass. Obviously this is not acceptable. For comparison, a more efficient engine is also plotted. Notice that at 5 years thrust time, the more efficient ion engine reaches the levels of approximately 10% propellant mass and 10% power plant mass. This is consistent with the findings in Chapter 3 that the propulsion system of spacecraft in clusters should have $I_{sp} \approx 3500$ and $\eta \approx 65\%$. The cold gas system, whose mass is made up entirely of propellant, requires less mass than the linear ion engine for thrust times less than 2 months. As thrust times increase, however, the lower specific impulse of the cold gas system forces its propellant mass to increase quickly, eventually exceeding the mass of linear ion system. A linear ion thruster as presently conceived is not appropriate for clusters of microsatellites.

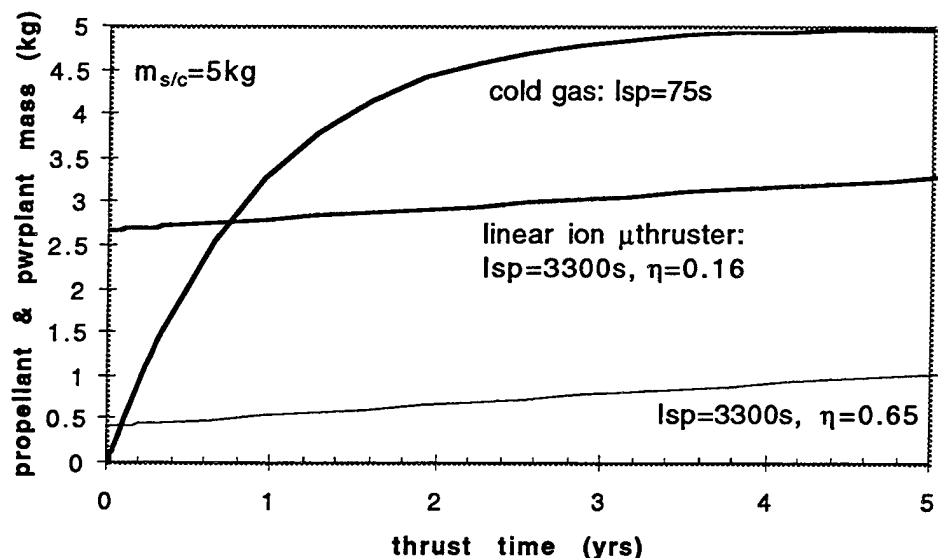


Figure 6-8. Mission Propulsion mass (excluding thruster itself)

6.4 SUMMARY AND CONCLUSIONS

The performance of the linear ion microthruster was examined using Brophy's model to predict energy costs per beam ion. This energy cost was then translated into thruster efficiencies. For linear ion microthrusters on the scale of 0.1 mm to 1 mm, magnetic fields can not be used to increase the primary electron confinement length. Path lengths are, therefore, limited to distances on the order of chamber dimensions.

Application of these findings to linear ion microthruster design indicate that beam ion production costs tends to decrease as the number of chambers decreases for a given thrust level. Further, for a given number of chambers beam ion cost increases as length increases. Shorter chamber lengths are more efficient due to a lower ratio of wall surface area to exit area. This results in a lower fraction of ions neutralized after contact with cathode potential surfaces. For short thrusting times during a microsatellite cluster mission, a cold gas system is feasible. For a period longer than a few months, the mass of propellant required eliminates a cold gas system from consideration. Unfortunately, the linear ion microthruster, as currently conceived, is not efficient enough to perform the mission for any length of time.

References

1. Brophy, J.R. et al. "Ion Thruster-On-A Chip for Microspacecraft" unpublished white paper. Jet Propulsion Lab. April 26, 1995.
2. Beattie, J.R. et al. "18-mN Xenon Ion Propulsion Subsystem", Hughes Research Laboratories, IEPC-91-010 23rd International Electric Propulsion Conference.

This page intentionally left blank

Chapter 7

Summary and Conclusions

The previous chapter examined design considerations relating to a linear ion microthruster concept. That was the last of a progression of topics discussed in this thesis. Those topics have been cost modeling of distributed satellite systems, determination of propulsion system requirements for satellite clusters and swarms, and analysis of ion micropropulsion systems for use in swarms of microsatellites. This chapter summarizes the finding of this thesis and reiterates the conclusions reached.

In Chapter 2, the total costs over a 10 year mission life were calculated for three configurations of the NPOESS mission. Distributing the primary instruments among three smaller satellites significantly increases the reliability of each individual satellite. This increased reliability substantially reduced the number of ground and on-orbit spares required, thus reducing mission costs compared to a single large satellite configuration.

From this analysis, it can be concluded that the distribution of sensors among several satellites is appropriate when the savings from increased reliability outweigh the increased cost to deploy the distributed system. Further, distribution is less advantageous for systems with high sensor reliability.

A distributed architecture makes sense if it can offer reduced cost or improved performance. Because the performance requirements, and the associated

probability of satisfying them, are embedded in its calculation, lifetime cost is a useful metric for architecture analysis. The appropriateness of distribution is highly dependent on the characteristics of a specific mission. As a means to reduce mission costs, it is recommended that satellite manufacturers trade-off the following advantages and disadvantages of distribution during the initial design phase:

- Improved resolution corresponding to the large baselines of sparse apertures formed by clusters or swarms of satellites.
- Lower failure compensation costs due to the separation of important system components among many satellites.
- An increase in system complexity leading to longer development times.

The fundamental conclusion is that large constellations of hundreds or thousands of small and microsatellites could feasibly perform missions currently being carried out by traditional satellites today.

Chapter 3 examined the propulsive requirements necessary to maintain the relative positions of satellites orbiting in a local cluster. Formation of these large baseline arrays could allow high resolution imaging of terrestrial or astronomical targets using techniques similar to those used for decades in radio interferometry. A key factor in the image quality is the relative positions of the individual apertures in the sparse array. The relative positions of satellites in a cluster are altered by "tidal" accelerations which are a function of the cluster baseline and orbit altitude.

From these findings, it can be concluded that near continuous thrusting by a propulsive system is necessary to maintain the relative positions of the satellites within allowable tolerances. Satellite mass, volume, and power constraints limit reasonable cluster baselines to approximately 30 m, 300 m, and 5000 m at

1000 km, 10,000 km, and GEO altitudes respectively. To maintain these cluster baselines, the propulsive system must operate at minimum I_{sp} and efficiency equal to approximately 3000s and 65% respectively with a thrust/spacecraft mass ratio of approximately $15\mu\text{N/kg}$. These parameters are consistent with those of ion engines. The rest of this thesis examined the performance of micro ion engines with the purpose of using them to maintain the relative positions of microsatellites in a cluster or swarm.

Chapter 4 formulates an analytical model, known as Brophy's Theory, to predict the performance of cylindrical ring-cusped ion engines. The model is used to predict the performance of ring-cusped ion engines. It was shown that energy cost per beam ion, ϵ_B , can be formulated as a simple algebraic equation. Most of the parameters in Brophy's model are known *a priori* given the choice of propellant gas, chamber geometry, and operating conditions. The remaining parameters can be determined using Arakawa's algorithm, the fundamentals of which were also described in this chapter.

Chapter 5 uses Brophy's model and Arakawa's algorithm to examine how performance of cylindrical ion engines changes as their scale is reduced several orders of magnitude. The code is discussed first with an emphasis on the formulations used to simulate particle behavior within the chamber. Next, an argument is outlined as to how thruster parameters such as mass flow rate and discharge voltage should change as thruster size is scaled. The effect on performance of scaled cylindrical ion thrusters is then presented.

Based on these findings, it can be concluded that magnetic fields can not be scaled inversely proportional to the chamber scale. At those scales the fraction of ions which reach the beam is essentially the ratio of the chamber exit area to the total chamber area. Application of these findings to linear ion microthruster design indicate that beam ion production costs tends to decrease as the

number chambers decreases for a given thrust level. Further, for a given number of chambers beam ion cost increases as length increases.

In chapter 6, the performance of the linear ion microthruster was examined using Brophy's model to predict energy costs per beam ion. This energy cost was then translated into thruster efficiencies. For linear ion microthrusters on the scale of 0.1 mm to 1 mm, magnetic fields can not be used to increase the primary electron confinement length. Path lengths are, therefore, limited to distances on the order of chamber dimensions.

Application of these findings to linear ion microthruster design indicate that beam ion production costs tends to decrease as the number chambers decreases for a given thrust level. Further, for a given number of chambers beam ion cost increases as length increases. Shorter chamber lengths are more efficient due to a lower ratio of wall surface area to exit area. This results in a lower fraction of ions neutralized after contact with cathode potential surfaces. Overall, however the performance of the linear ion microthruster is very poor. For short thrusting times during a cluster mission, a cold gas system is feasible. For a period longer than a few months, the mass of propellant required eliminates a cold gas system from consideration. Unfortunately, the linear ion microthruster, as currently conceived, is not efficient enough to perform the mission for any length of time.

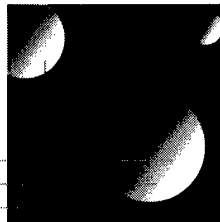
**Electron Current Collection by a Positively
Charged Tether Using a Particle-In-Cell Method**

Tatsuo Onishi

May 1998

SERC #4-98

(Under the supervision of Prof. Manuel Martinez-Sanchez)



*MIT
Space
Engineering
Research
Center*

Massachusetts
Institute of
Technology

Cambridge
Massachusetts
02139

Electron Current Collection by a Positively Charged Tether Using a Particle-In-Cell Method

by

Tatsuo Onishi

Submitted to the Department of Aeronautics and Astronautics
on May 18, 1998, in partial fulfillment of the
requirements for the degree of
Master of Science in Aeronautics and Astronautics

Abstract

A Particle-In-Cell (PIC) method is developed and applied to simulate the electron current collection by a positively charged tether in a quiescent unmagnetized plasma under the Maxwellian collisionless condition. We compare our result with the exact solution to validate our code. This simulation is performed with the help of a non-rectangular grid and a new treatment of the outside boundary condition. The error induced by a non-rectangular grid is calculated and the effect of it is considered. The outside boundary treatment improves the accuracy of the amount of current collected by the tether. A very small ion mass is used and it is verified to speed up the computation considerably without loss of quality in the result. The comparison with the exact solution shows that our code provides good qualitative and quantitative approximations.

Thesis Supervisor: Manuel Martinez-Sanchez
Title: Professor

Acknowledgments

I would like to show my profound appreciation to Professor Manuel Martinez-Sanchez for the chance he gave me to work on this splendid project. He always lighted up the path I was walking and led me to the right place. And I would also like to send my eternal thanks to my parents, Tadao and Yoshiko Onishi, who always back me up to walk the path.

Contents

1	Introduction	7
2	Orbital Motion Limit (OML) Current	9
3	Numerical Method (Particle-In-Cell)	13
3.1	Particle-In-Cell (PIC)	13
3.2	Simulation Model	15
3.3	Problems in PIC	18
3.3.1	Deformed Grid	20
3.3.2	Boundary Condition	26
3.3.3	Computational Cost	30
3.4	Results	30
4	Conclusion & Further Work	40
	Bibliography	42

List of Figures

2-1	The effective potential for the thick and thin sheath	11
3-1	A typical cycle of PIC	15
3-2	Mesh for the case $\xi_p = \frac{r_p}{d_{Debye}} = 1$	19
3-3	A uniform rectangular grid	21
3-4	A small element in a cell	22
3-5	Cells of different sizes	24
3-6	Transformed square grid (left) and the original deformed grid (right)	25
3-7	Electron and Ion Flow	28
3-8	Electric charge density for the case $\xi_p = 1$	32
3-9	Electric charge density for the case $\xi_p = 2$	33
3-10	Electric charge density for the case $\xi_p = 5$	34
3-11	Electric potential distribution for the case $\xi_p = 1$	35
3-12	Electric potential distribution for the case $\xi_p = 2$	36
3-13	Electric potential distribution for the case $\xi_p = 5$	37
3-14	History of the Current collection (left) $\xi_p = 1$, (middle) $\xi_p = 2$ and (right) $\xi_p = 5$, the OML current (dashed line) and the exact value (solid line)	38
3-15	Current collection vs. $1/\xi_p$. OML current (dashed), the exact value (solid) and computed value (error bars)	39

List of Tables

3.1 Parameters 17

Chapter 1

Introduction

In tethered satellite technology, it is important to estimate how many electrons a spacecraft can collect from its surrounding plasma by its positively charged tether. The analysis is, however, very difficult because of the small but significant Geomagnetic field and the spacecraft's relative motion to both ions and electrons [5]. One of the approaches for the solution to this problem is the numerical method. In the numerical analysis of space plasma, one of the most reliable methods has been the Particle-In-Cell (PIC) method. In this thesis, we develop a PIC code for a two dimensional collisionless plasma without magnetic field.

The original Particle-In-Cell code was established by *Birdsall* at U.C.Berkeley. [1] Using a rectangular grid and finite-size particles, he has studied the effects of grid size and timestep on the simulation and relevant numerical instabilities. As the "bible" to PIC users, his publications give us excellent criteria for its numerical stability and reliability. The concept of PIC in our code is mostly from this "bible".

The usage of a rectangular grid and a finite-size particle, however, poses some problems. In the usual numerical application, very complicated configurations require non-rectangular body fitted grids. Being defined by the grid size, the finite-size particle can not maintain its constant size any more. In this thesis, we estimate the error induced by the use of a non-rectangular grid and consider the effect on our simulation.

In order to validate our code, we apply it to the current collection by a cylindrical

tether in a collisionless unmagnetized plasma, near the boundary of Orbital Motion Limited (OML) regime, for which an exact solution exists [4]. The OML theory, which will be further discussed in the next chapter, applies in the limit of large ratios of Debye length to radius.

In the vicinity of the tether, there is a region called “sheath”, where quasi-neutrality does not apply. That is to say, the densities of ions and electrons differ from each other considerably. In order to reproduce this region, we follow the motion of both ion and electron particles. Since the mass ratio of an ion to an electron is very large, we would need a great number of iterations till both species come to have converged distributions, without having electrons travel a large distance in one iteration, which would induce a large error in the energy conservation. However, the fact that, at tether potentials much greater than the ion temperature, we can assume that no ion is absorbed by the tether, solves this problem of the computational cost. In theory, the ion density at an arbitrary point does not depend on its mass when its distribution is Maxwellian.

Since some electrons are absorbed on the surface of the tether, there is also a region called “pre-sheath” outside the sheath, where quasi-neutrality prevails but the electric potential is not the same as that of the ambient plasma at infinity.

In a computation, we have to use a finite region to calculate field quantities. And, because of the limited memory on a computer, we can not use an infinitely large grid to include the pre-sheath region. Therefore we have to clip a computational region out of this infinitely large space, and determine the outer boundary conditions by considering only the quasi-neutrality and the collisionless nature of the plasma. The limitation of the number of particles available in a computer gives fluctuating local boundary conditions. To avoid this, we use a spatially averaged boundary condition.

The goal of this thesis is to establish a code to simulate a collisionless unmagnetized plasma in and near the sheath region. Based on this code, we plan to include later all the phenomena encountered by a tethered satellite, such as Geomagnetic field and plasma cross-flow.

Chapter 2

Orbital Motion Limit (OML)

Current

Current collection by spherical and cylindrical probes (tethers) was first analyzed by *Lagmuir* and *Mott-Smith* [6] , who named the thin cylinder limit, 'Orbital Motion Limit (OML)'. When OML theory applies, namely, when the ratio of the probe (tether) radius to the Debye length of the plasma is so small that the shielding becomes unimportant, the number of electrons absorbed by the probe is determined from energy and angular momentum considerations alone.

The OML limit can be described in terms of the effective potential. [3] Let J and E be the angular momentum and the energy of a particle, respectively. From the energy conservation and the angular momentum conservation of an electron in two dimensions, although the velocity v_{\parallel} along the cylinder axis can be nonzero, we have

$$E = \frac{1}{2}m_e(v_r^2 + v_\theta^2) + q\phi \quad (2.1)$$

$$J = m_e r v_\theta \quad (2.2)$$

where r is the distance from the probe center, m_e the electron mass, q the electron charge of an electron, ϕ the local potential, v_r the radial velocity component, and v_θ the azimuthal velocity component. Substituting equation (2.2) into equation (2.1),

we have

$$v_r^2 = \frac{2}{m_e} \left(E - q\phi - \frac{J^2}{2m_e r^2} \right). \quad (2.3)$$

In order for a particle to reach the surface of the probe, the right-hand side of equation (2.3) must be positive not only at the surface of the probe, but also all along the path from infinity to the surface. To consider the particle motion from the one dimensional viewpoint, the effective potential defined by

$$U = q\phi + \frac{J^2}{2m_e r^2} \quad (2.4)$$

should be considered. Substituting the effective potential (2.4) into (2.3), we have

$$v_r^2 = \frac{2}{m_e} (E - U). \quad (2.5)$$

By taking the effective potential as a normal potential, we can treat the 2-dimensional particle motion as the 1-dimensional case. Fig(2-1) illustrates two limits regarding the effective potential. Assume that the probe is on the left of the figure. When the sheath is thin (Langmuir Limit), the second term of equation (2.4) becomes dominant near the probe and $v(r)$ has an intermediate minimum value. For some attracted particles, this bump in the effective potential prevents them from reaching the surface even if they have enough energy. When the sheath is thick (OML limit), the first term in equation (2.4) becomes dominant throughout the region, and the electric potential is large enough to overwhelm the bump in the effective potential. Therefore the effective potential becomes monotonous, and the only requirement for a particle to reach the surface is to have a positive value of the right-hand side of equation (2.3) at the probe surface.

Electrons absorbed by the probe should be accelerated by the field force up to a certain total velocity toward the probe. Therefore, in terms of energy, it is equivalent to say,

$$\frac{1}{2} m_e (v_r^2 + v_\theta^2) + q\phi_p \geq 0 \quad (2.6)$$

where ϕ_p is the probe potential.

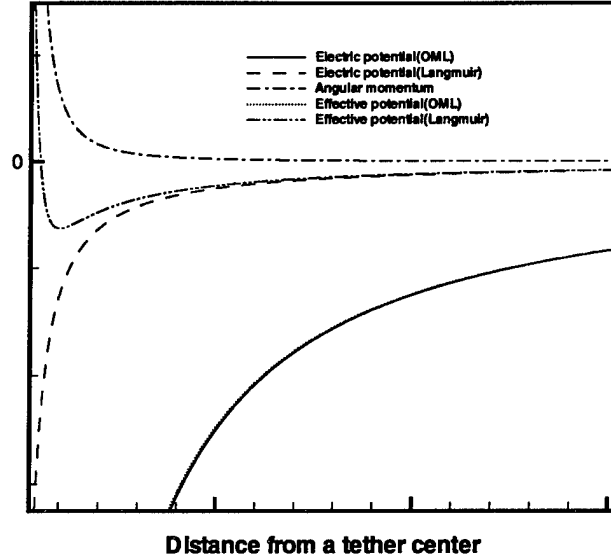


Figure 2-1: The effective potential for the thick and thin sheath

In the absence of collisions, the solution to Vlasov's equation must have the Maxwell-Boltzman form for any velocity that does occur:

$$f_e(v) = n_\infty \left(\frac{m_e}{2\pi k T_\infty} \right)^{3/2} \exp \left(- \frac{q\phi_p + \frac{m_e}{2} (v_\perp^2 + v_\parallel^2)}{k T_\infty} \right) \quad (2.7)$$

where n_∞ is the density at infinity, k the Boltzmann constant, T_∞ the temperature at infinity and v_\parallel a velocity component parallel to the cylindrical probe.

At the surface of the probe, only electrons which satisfy the equation (2.6) can exist and be counted for the current collection. The current density into the probe is given as

$$j = q \iiint_{\frac{1}{2}m_e v_\perp^2 + q\phi_p \geq 0} f_e d\mathbf{v} \quad (2.8)$$

$$= q \int_{-\infty}^{\infty} dv_\parallel \int_{\sqrt{2|q\phi_p|/m_e}}^{\infty} \int_{-\pi/2}^{\pi/2} v_\perp f_e v_\perp \cos\theta d\theta dv_\perp \quad (2.9)$$

$$= \frac{qn_\infty \bar{c}_\infty}{2\sqrt{\pi}} \left[\sqrt{\frac{|q\phi_p|}{kT_\infty}} + \frac{\sqrt{\pi}}{2} e^{\frac{|q\phi_p|}{kT_\infty}} \operatorname{erfc} \left(\sqrt{\frac{|q\phi_p|}{kT_\infty}} \right) \right] \quad (2.10)$$

$$\rightarrow \frac{qn_{\infty}\bar{c}_{\infty}}{2\sqrt{\pi}}\sqrt{\frac{|q\phi_p|}{kT_{\infty}}} \quad (2.11)$$

since, in the limiting form, $x \rightarrow \infty$, we have

$$\operatorname{erfc}(x) = 1 - \operatorname{erf}(x) = \frac{1}{\sqrt{\pi}} \int_x^{\infty} e^{-t^2} dt \quad (2.12)$$

$$\rightarrow \frac{2}{\sqrt{\pi}} \frac{e^{-x^2}}{x} \quad (2.13)$$

where \bar{c}_{∞} is the random thermal velocity given as

$$\bar{c}_{\infty} = \sqrt{\frac{8kT_{\infty}}{\pi m_e}} \quad (2.14)$$

Therefore, when $\frac{|q\phi|}{kT_{\infty}} \gg 1$, the current density (2.13) becomes

$$j = \frac{qn_{\infty}}{\pi} \sqrt{\frac{2|q\phi_p|}{m_e}} \quad (2.15)$$

which is independent of electron temperature, T_e . Note that equation (2.10), and hence equation (2.15) are independent of the shape of the cylinder's cross section (as long as OML conditions prevails).

This limiting value of current density is used in this thesis as one of the criteria in the validation of our code. To see whether our code simulates plasma behavior well in the vicinity of the OML regime, we examine several Debye ratios, r_p/d_{Debye} , for the case that the ratio of the probe potential to the electron temperature, $\chi_p = \frac{|q|\phi_p}{kT_{\infty}}$, is 25, which case *Laframboise* has exactly computed. The solutions are available as analytical fits, which we quote in this thesis. [4, 2]

Chapter 3

Numerical Method (Particle-In-Cell)

In this chapter, the Particle-In-Cell (PIC) method used here is explained in detail. First, we introduce the structure and mechanism of the PIC method. Secondly, we describe the model for our simulation and the governing equations in a nondimensionalized form. Thirdly, we discuss the problems with the PIC method, which have occurred in our application. Finally, we show the results from this simulation and compare them with the exact solutions.

3.1 Particle-In-Cell (PIC)

The Particle-In-Cell (PIC) method has been very successful in the simulation of collisionless plasmas. In PIC, many particles are distributed in phase space. That is, a particle's motion is described by its position and velocity. In kinetic theory, this particle distribution is defined as a distribution function and governed by the Boltzmann equation. The Boltzmann equation with no collisional term on its right-hand side is given as follows. (Vlasov's equation)

$$\frac{\partial f}{\partial t} + \mathbf{v} \frac{\partial f}{\partial \mathbf{x}} + \mathbf{F} \frac{\partial f}{\partial \mathbf{v}} = 0 \quad (3.1)$$

In an actual computation, the number of particles available is much less than that in reality. This fact requires us to introduce the concept of a “superparticle”, corresponding to a group of real particles. One superparticle contains many real particles, and as many particles as another.

To describe the motion of the superparticle, we need to know velocity and the force acting on it. The force acting on a superparticle can be calculated by considering all Lorentz forces caused by the other superparticles. However, this calculation is computationally too expensive. Instead of doing so, PIC uses a grid on which Maxwell’s equations are solved to give the electric field, which is then interpolated to the position of each superparticle. As the name “Particle-In-Cell” implies, in a computational domain, a superparticle moves through a grid or a cell, regardless the position of grid nodes. A PIC code method consists of four processes as described below.

At each time step, the electric charge density on each node is estimated from the positions of all superparticles. This first process is called “charge assignment”. Then on a grid, the electric potential and electric field are computed. We use a finite difference method in this second process; especially to solve Poisson’s equation, we use Successive Line OverRelaxation (SLOR). Poisson’s equation to relate electric potential to charge density is

$$\nabla^2 \phi = -\frac{\rho}{\epsilon} \quad (3.2)$$

where $\rho = |q|(n_i - n_e)$ is the electric charge density, and the electric field is

$$\mathbf{E} = -\nabla \phi. \quad (3.3)$$

if $\frac{\partial \mathbf{B}}{\partial t}$ can be neglected.

After computing \mathbf{E} on a grid, the electric field is interpolated onto each superparticle’s position, and the corresponding force and acceleration of a superparticle is calculated. This third process is called “interpolation”. The first and third process involve the same weighting method to avoid the so-called “self force”. Once we know the acceleration, a leapfrog method, the final process, updates the velocity and

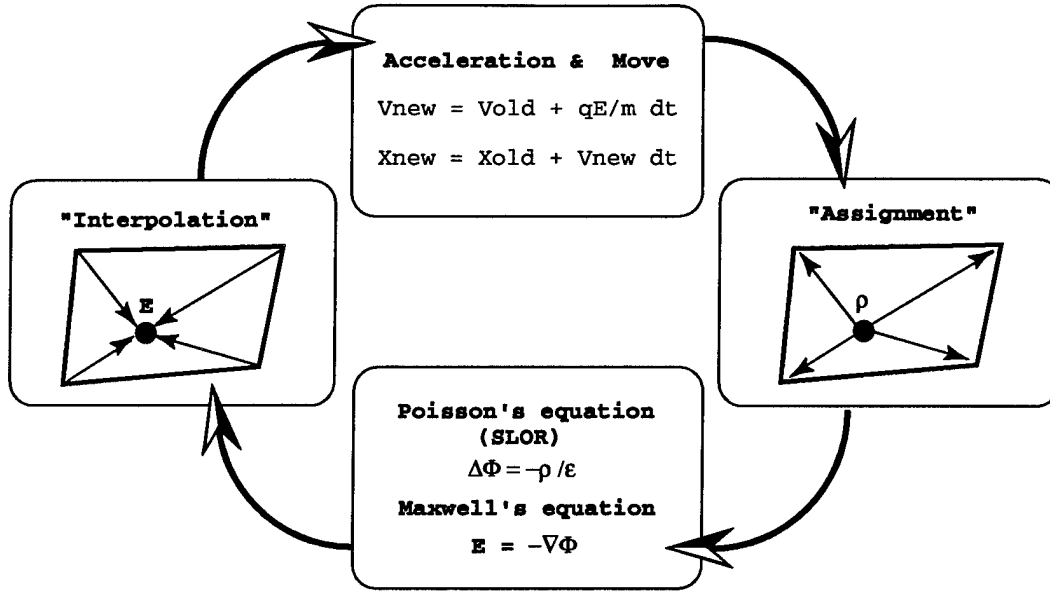


Figure 3-1: A typical cycle of PIC

position of each superparticle as follows;

$$\mathbf{v}_{new}^{(n)} = \mathbf{v}_{old}^{(n-1)} + \frac{q\mathbf{E}^{(n-1/2)}}{m} \Delta t \quad (3.4)$$

$$\mathbf{x}_{new}^{(n+1/2)} = \mathbf{x}_{old}^{(n-1/2)} + \mathbf{v}_{new}^{(n)} \Delta t. \quad (3.5)$$

This completes one iteration in a PIC calculation. One cycle of a PIC is shown schematically in fig 3-1.

3.2 Simulation Model

This section explains the simulation model. We wish to calculate the electron current collection by a positively charged cylindrical tether in a quiescent unmagnetized plasma in a Maxwellian collisionless condition. For simplicity, we first nondimensionalize the governing equations.

Non-dimensionalization

Before we consider the non-dimensionalization, we should know what equations are involved in our simulation. As we showed before, the leapfrog method uses equations

(3.4) and (3.5). To solve for electric field from electric charge density, we use Poisson's equation (3.2) and Maxwell's equation (3.3). Essentially, these four equations are the governing equations. Since we are not directly solving Boltzmann's equation (3.1), it is not considered as a governing equation. The distribution function, however, should be considered. A Maxwellian distribution function is used to calculate the number of particles replenished into the computational domain at each timestep and the density at the outside boundary.

In non-dimensionalizing the governing equations, we use reference values as follows;

Length	:	$l_{ref} = d_{Debye} = \sqrt{\frac{\epsilon k T_e}{q^2 n_\infty}}$
Time	:	$t_{ref} = 10/\omega_p \ (\omega_p = \sqrt{\frac{q^2 n_\infty}{\epsilon m_e}})$
Potential	:	$\phi_{ref} = \frac{k T_\infty}{e}$
Density	:	$n_{ref} = n_\infty/100$
Velocity	:	$v_{ref} = l_{ref}/t_{ref} = v_T/10 = \sqrt{\frac{k T_e}{m_e}}/10$
Distribution function	:	$f_{ref} = n_{ref}/v_{ref}^3$

As is discussed later, somehow strange reference values seen here is totally due to the computational limitations.

Substituting these reference values, we nondimensionalize equations (3.2), (3.3), (3.4), (3.5) and (2.7).

$$\hat{\nabla}^2 \hat{\phi} = -(\hat{n}_i - \hat{n}_e)/100 \quad (3.6)$$

$$\hat{\mathbf{E}} = -\hat{\nabla} \hat{\phi} \quad (3.7)$$

$$\hat{\mathbf{v}}_{new} = \hat{\mathbf{v}}_{old} \pm 100 \left(\frac{m_e}{m} \right) \hat{\mathbf{E}} d\hat{t} \quad (3.8)$$

$$\hat{\mathbf{x}}_{new} = \hat{\mathbf{x}}_{old} + \hat{\mathbf{v}}_{new} d\hat{t} \quad (3.9)$$

$$\hat{f} = \frac{1}{10(2\pi)^{3/2}} \exp(-50\hat{v}^2 - \hat{\phi}) \quad (3.10)$$

where a hat ($\hat{\cdot}$) indicates a nondimensional quantity. In equation (3.8), the minus sign is taken when the particle is an electron ($m = m_e$), and the plus when an ion ($m = m_i$).

In this simulation, we use the parameters in Table 3.1. In deciding these values,

Electron Temperature	$\hat{T}_e = 100$
Ion Temperature	$\hat{T}_i = 100$
Electron density	$\hat{n}_e = 100$
Ion density	$\hat{n}_i = 100$

Table 3.1: Parameters

we first consider the number of particles available in a computer memory. In order to include the sheath region completely, we have the radius of the computational domain as $15d_{Debye}$. To be consistent with the governing equations and these non-physical values, we calculate other nondimensionalized variables, starting with the Debye length equal to unity,

$$\begin{aligned}\hat{d}_{Debye} &= \sqrt{\frac{\epsilon k T}{q^2 n}} / l_{ref} \\ &= 1.0\end{aligned}\tag{3.11}$$

Since the area of the computational domain is $(15\hat{d}_{Debye})^2\pi$, we need approximately $\hat{n}_{e,i}(15\hat{d}_{Debye})^2\pi$ particles for each species. This number is limited by the computer. In our case, the number of particles available is about 200,000. In order to run the simulation with as many particles as possible but less than this, we set $\hat{n}_{e,i} = 100$. From equation (3.11), we also have the temperature, $\hat{T}_{i,e} = 100$. Consequently, we have the thermal velocity,

$$\begin{aligned}\hat{v}_T &= \sqrt{\frac{kT}{m}} / v_{ref} \\ &= \sqrt{100}\end{aligned}\tag{3.12}$$

and the plasma frequency,

$$\begin{aligned}\hat{\omega}_p &= \sqrt{\frac{q^2 n}{\epsilon m}} t_{ref} \\ &= \sqrt{100}.\end{aligned}\tag{3.13}$$

As we can see now, the factors seen in the reference values are determined by the computational limitations.

We should note that we use hypothetically light ion's mass, which is the same as an electron's mass. We discuss the validity of this hypothesis and its effect on the computational cost later. Physically, since almost no ions are lost to the probe, all velocities are possible everywhere, and their distribution is, in fact, a full Maxwell-Boltzmann distribution, so that the ion density is simply $n_i = n_\infty \exp(-\frac{|q|\phi}{kT_i})$, which does not depend on m_i at all.

Mesh

In our code, the Debye length is first determined. Therefore, for various cases of Debye ratio, i.e. the ratio of the tether radius to the Debye length, different meshes are used. The mesh used for the case of the Debye ratio equal to 1, $\xi_p = 1$, is shown in Figure 3-2. Each mesh size in the radial direction is kept to be a half of the Debye length and in the azimuthal direction mesh size is kept less than the Debye length, which should avoid numerical instabilities.

The main purpose of this simulation is to calculate how many particles, mainly electrons, are collected by a cylindrical tether in a Maxwellian collisionless condition. Particles are counted and absorbed when they reach the surface of the tether. From outside of the computational domain, where plasma is assumed to be Maxwellian, electrons and ions are replenished into the domain with velocity and position calculated from the Maxwellian distribution function using a random number generator.

3.3 Problems in PIC

As we have applied the PIC method, we have been confronted with some problems. In this section, we discuss those problems and some solutions to them.

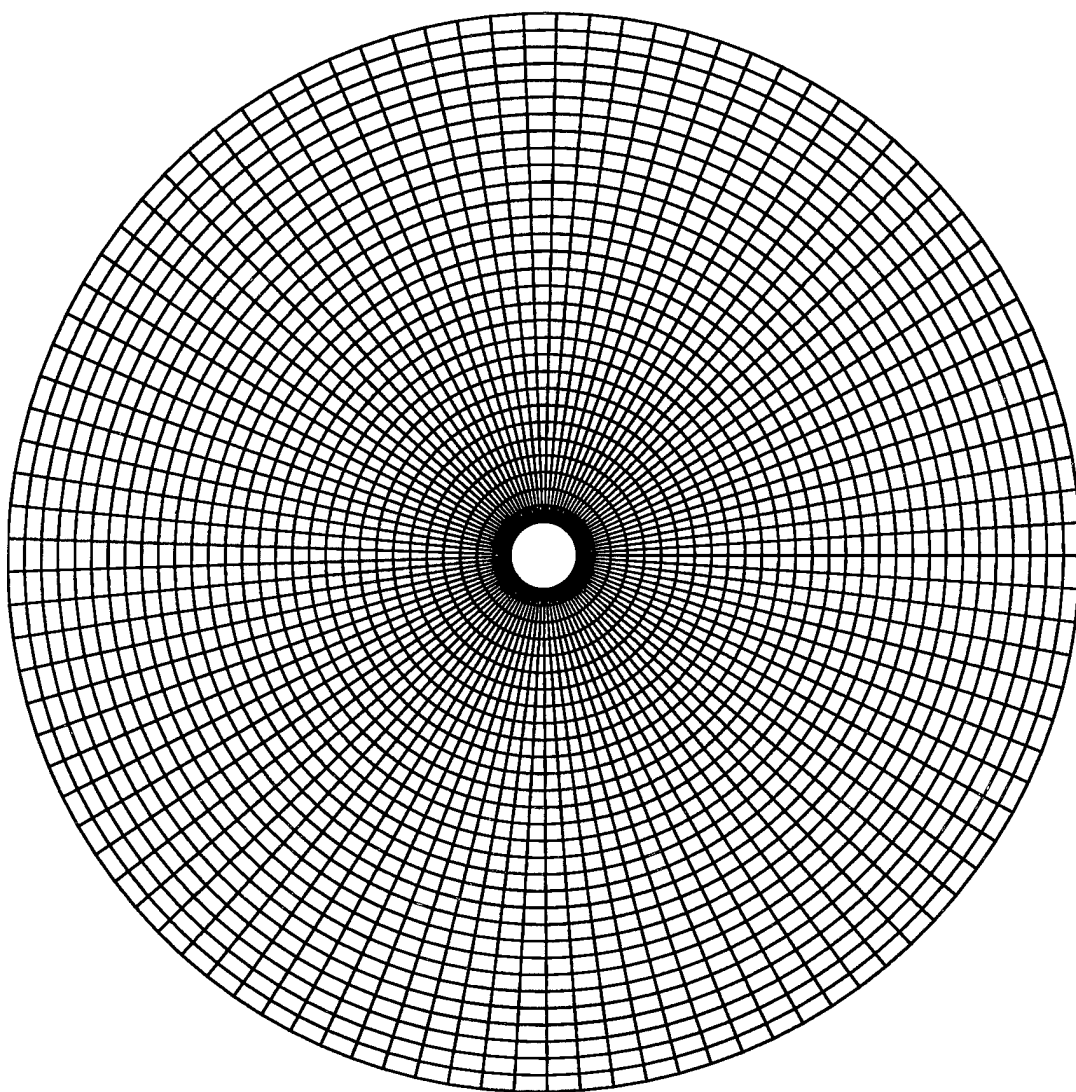


Figure 3-2: Mesh for the case $\xi_p = \frac{r_p}{d_{Debye}} = 1$

3.3.1 Deformed Grid

As we consider some practical configurations in engineering applications, it is almost impossible to do it with only a rectangular grid. The more complicated the configuration becomes, the more necessary it is to use a deformed body-fitted grid. Concerning this problem, we can think of two factors of a deformed grid, which are likely to cause problems, namely the area of the cell and the degree of deformity from a rectangle.

First, we describe the mechanism of the “assignment” and “interpolation” processes. In the original PIC method based on a rectangular grid, electric charge density is first calculated from the particle position and assigned to four nodes according to the area-weighting function. The area-weighting function is defined as follows.

Uniform rectangular grid

A particle with electric charge q is located at (x, y) in a cell of area A , which is defined by four nodes (x_i, y_i) , $(x_i + \Delta x, y_i)$, $(x_i, y_i + \Delta y)$ and $(x_i + \Delta x, y_i + \Delta y)$. That is, the area A is given as

$$A = \Delta x \Delta y. \quad (3.14)$$

First, we calculate the electric charge density, by dividing q by the area, $\Delta x \Delta y$.

$$\rho = \frac{q}{\Delta x \Delta y} \quad (3.15)$$

Next, we split this charge density into four segments, which are proportional to the area demarcated by lines parallel to grid edges. Thus, to point $A(x_i, y_i)$, charge density

$$\rho_A = \rho \frac{\square PFCG}{\square ABCD} = q \frac{(x_{i+1} - x)(y_{i+1} - y)}{\Delta x^2 \Delta y^2} \quad (3.16)$$

is assigned. Likewise, to the other points, we assign charge density as

$$\rho_B = \rho \frac{\square PGDH}{\square ABCD} = q \frac{(x - x_i)(y_{i+1} - y)}{\Delta x^2 \Delta y^2} \quad (3.17)$$

$$\rho_C = \rho \frac{\square PHAE}{\square ABCD} = q \frac{(x - x_i)(y - y_i)}{\Delta x^2 \Delta y^2} \quad (3.18)$$

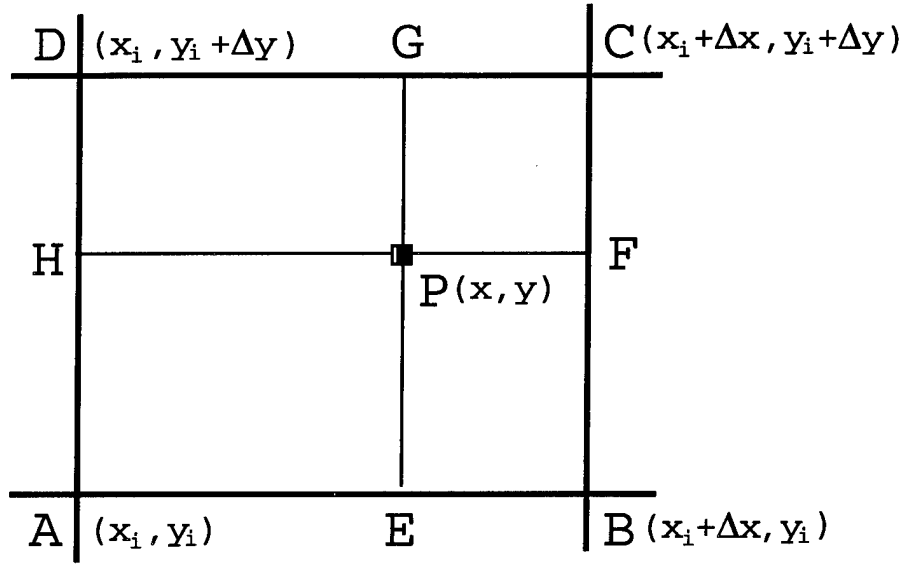


Figure 3-3: A uniform rectangular grid

$$\rho_D = \rho \frac{\square PEBF}{\square ABCD} = q \frac{(x_{i+1} - x)(y - y_i)}{\Delta x^2 \Delta y^2} \quad (3.19)$$

This assignment process is applied to all particles in the cell $ABCD$.

We next estimate the order of accuracy of this assignment method. To exclude the effects of an insufficient number of particles, we assume that there is a sufficient number of particles in a cell. This condition is expressed by requiring the density to be a continuous function. When we consider a small element in the cell, the condition requires that there be still many particles in it.

Let $f(x, y)$ be the superparticle density function at (x, y) , and $dxdy$ be the area of the small element. The condition to have a sufficient number of particles requires

$$f(x, y)dxdy \geq 1 \quad (3.20)$$

Assuming a large enough number of particles in a cell and using the Taylor series expansion, we estimate the order of accuracy at the node A . One assignment process is applied at once to all particles in the small element. Since the element is taken to be very small, we can consider that there are $f(x, y)dxdy$ particles at (x, y) . The

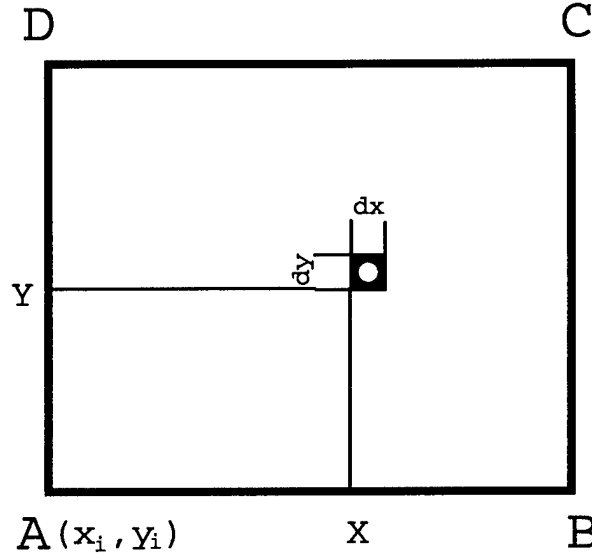


Figure 3-4: A small element in a cell

assigned charge density at A from those particles' point (x, y) is given by

$$d\rho_A(x, y) = \frac{q(x_{i+1} - x)(y_{i+1} - y)}{\Delta x^2 \Delta y^2} f(x, y) dx dy. \quad (3.21)$$

Assigning all particles in a whole cell to the node A , we have,

$$\rho_A = \int_{x_i}^{x_{i+1}} \int_{y_i}^{y_{i+1}} d\rho_A(x, y) \quad (3.22)$$

$$= \int_{x_i}^{x_{i+1}} \int_{y_i}^{y_{i+1}} \frac{q(x_{i+1} - x)(y_{i+1} - y)}{\Delta x^2 \Delta y^2} f(x, y) dx dy \quad (3.23)$$

$$= \int_0^1 \int_0^1 q(1 - X)(1 - Y) g(X, Y) dX dY \quad (3.24)$$

where $X = \frac{x - x_i}{\Delta x}$, $Y = \frac{y - y_i}{\Delta y}$ and $g(X, Y) = f(x_i + \Delta x X, y_i + \Delta y Y)$. Expanding $g(X, Y)$ around the point $(0, 0)$,

$$g(X, Y) = g(0, 0) + \left. \frac{\partial g}{\partial X} \right|_{(0,0)} X + \left. \frac{\partial g}{\partial Y} \right|_{(0,0)} Y + \dots \quad (3.25)$$

$$= f(x_i, y_i) + \left. \frac{\partial f}{\partial x} \right|_{(x_i, y_i)} \Delta x X + \left. \frac{\partial f}{\partial y} \right|_{(x_i, y_i)} \Delta y Y + \dots \quad (3.26)$$

and substituting this into equation (3.24), we have

$$\begin{aligned}
 \rho_A &= q \int_0^1 \int_0^1 [f(x_i, y_i)(1-X)(1-Y) \\
 &\quad + \left. \frac{\partial g}{\partial X} \right|_{(0,0)} X(1-X)(1-Y) + \left. \frac{\partial g}{\partial Y} \right|_{(0,0)} Y(1-X)(1-Y) + \dots] dX dY \quad (3.27) \\
 &= \frac{q}{4} f(x_i, y_i) + \frac{q}{12} \left. \frac{\partial f}{\partial x} \right|_{(x_i, y_i)} \Delta x + \frac{q}{12} \left. \frac{\partial f}{\partial y} \right|_{(x_i, y_i)} \Delta y + \dots \quad (3.28)
 \end{aligned}$$

Performing the same calculation for all particles in the other cells which surround the node A , we can cancel the 2nd and 3rd terms and get

$$\rho_A = qf(x_i, y_i) + O(\Delta x^2, \Delta y^2). \quad (3.29)$$

This shows that, as long as there are a sufficient number of particles, this area-weighting assignment method provides 2nd order of accuracy.

Rectangular grid with different cell sizes

Next, following the same procedure, we consider the effect of rectangular cells of different sizes on the assignment method (fig 3-5). When the cells are of different sizes but still rectangular, the 2nd and 3rd terms in equation (3.28) do not cancel out after the summation of corresponding terms from other cells. Instead of the second order of accuracy, we get

$$\begin{aligned}
 \rho_A &= qf(x_i, y_i) \\
 &\quad + \frac{q}{6} \left. \frac{\partial f}{\partial x} \right|_{(x_i, y_i)} (\Delta x_1 - \Delta x_2) + \frac{q}{6} \left. \frac{\partial f}{\partial y} \right|_{(x_i, y_i)} (\Delta y_1 - \Delta y_2) \\
 &\quad + O(\Delta x^2, \Delta y^2), \quad (3.30)
 \end{aligned}$$

which provides 1st order of accuracy only.

As we can see from the 2nd and 3rd terms in equation (3.30), using almost the same shape and size as those of adjacent cells, we can make these terms quite small, and make this method closer to second order of accuracy.

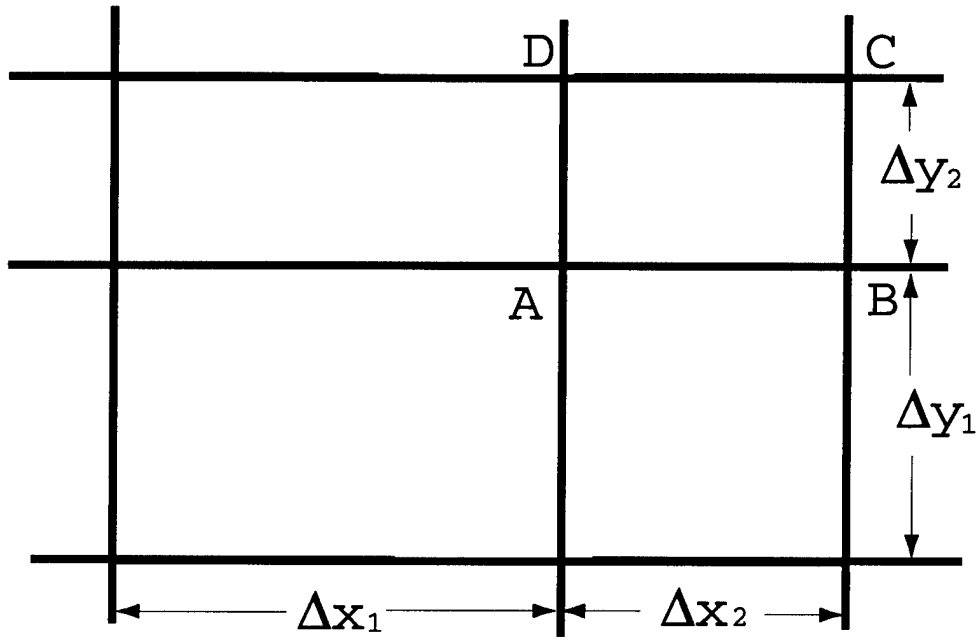


Figure 3-5: Cells of different sizes

Deformed grid

Next we consider the deformity of a grid. Since we use a linear interpolation [8, 7] from a deformed grid to a square grid on which the area-weighting is performed, we can not avoid a problem due to this deforming. In our code, we use the typical tri-linear interpolation from the physical domain (x, y) to the computational domain (r, s) given as

$$x = x_0 + x_1 r + x_2 s + x_3 r s \quad (3.31)$$

$$y = y_0 + y_1 r + y_2 s + y_3 r s \quad (3.32)$$

where

$$x_0 = x_{i,j}$$

$$y_0 = y_{i,j}$$

$$x_1 = x_{i+1,j} - x_{i,j}$$

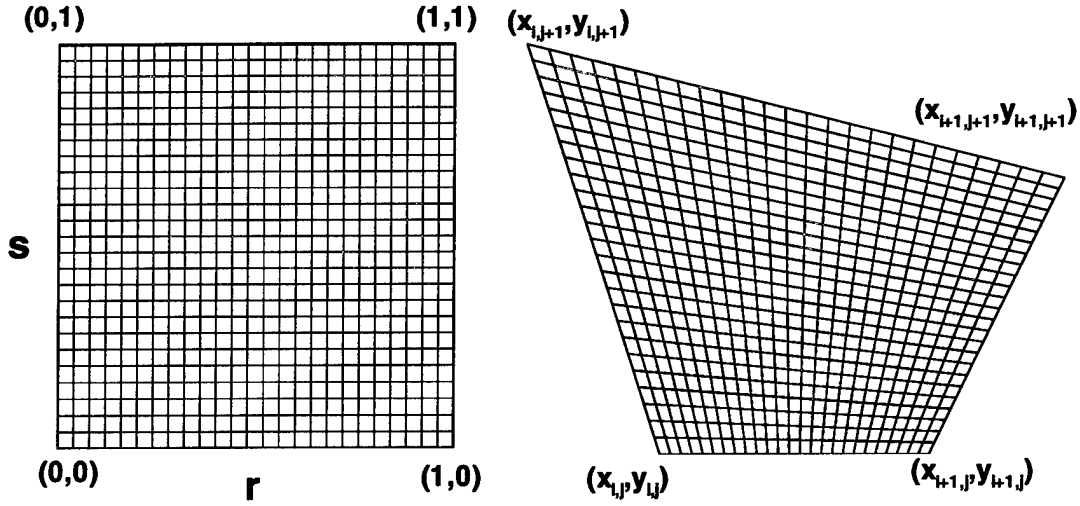


Figure 3-6: Transformed square grid (left) and the original deformed grid (right)

$$\begin{aligned}
 y_1 &= y_{i+1,j} - y_{i,j} \\
 x_2 &= x_{i,j+1} - x_{i,j} \\
 y_2 &= y_{i,j+1} - y_{i,j} \\
 x_3 &= x_{i+1,j+1} + x_{i,j} - x_{i+1,j} - x_{i,j+1} \\
 y_3 &= y_{i+1,j+1} + y_{i,j} - y_{i+1,j} - y_{i,j+1}
 \end{aligned}$$

The effect of the linear interpolation is understood when we look at Figure 3-6.

In a deformed cell, the grid density is sparser at the top and denser at the bottom. But its corresponding square cell has a completely uniform density distribution. This means that if we start for example with a particle distribution which is uniform in the grid on the left, it will not be uniform in the one on the right, and vice versa. Although we have no particular treatment done to solve this problem in our simulation, as seen in the grid we use (fig. 3-2), each cell is almost rectangular. Therefore, no serious error can be considered to be incurred due to the deformity of the cell. Moreover, in the grid no pair of adjacent cells has a significant difference in size and shape. This makes the assignment method to be close to 2nd order accurate.

3.3.2 Boundary Condition

In this section, we consider the outside boundary condition in our simulation. The importance of this boundary condition stems from the fact that some electrons are absorbed by a tether. We assume here that no ion is absorbed by the tether, because of its very high positive potential. Figure 3-7 illustrates the overall flow of electrons and ions. Due to this partial absorption of electrons by the tether, the electric potential at the computational outside boundary can not be zero with respect to the ambient plasma. If it were zero, the electron density would be less than the ion density, and thus it would violate the quasi-neutrality outside the sheath. To maintain the quasi-neutrality, the electron potential at the outside boundary should be more than zero. Positive potential attracts more electrons and fewer ions. This boundary condition is formulated as follows.

Let ϕ be the electric potential at an arbitrary point including the outside boundary. Assuming that ions are singly charged, we have the quasi-neutrality equation as

$$|n_e - n_i| \ll n_e. \quad (3.33)$$

In the computation, we use this condition in the form of

$$n_e = n_i. \quad (3.34)$$

However this does not allow us to transform Poisson's equation to Laplace's equation by equating the source term to zero, because the small difference $|q|(n_i - n_e)$ is divided by the small quantity ϵ_0 , leaving $\nabla^2 \phi$ indeterminate. As the plasma approximation claims, plasma tends to neutralize itself by imposing $n_e = n_i$. Therefore we impose the condition (3.34) on the outside boundary, and solve Poisson's equation inside that boundary only with non-zero source term on its right-hand side.

To determine the boundary condition, we need the potential, which is calculated as follows. The assumption that no ions are absorbed by the tether enables us to calculate the ion density at any point. Given the ion temperature, T_i and the potential,

ϕ , and integrating the Maxwell-Boltzmann distribution function in velocity space, we have the ion density as

$$n_i = n_\infty \exp\left(-\frac{|q|\phi}{kT_i}\right) \quad (3.35)$$

On the other hand, we can calculate only the density of inbound electrons¹. Since some electrons are absorbed, we do not know the limits of outbound electron distribution function in phase space. We denote the density of those outbound electrons as n_e^{out} . As for the inbound electron density, we can calculate it by integrating the Maxwellian distribution, since all those electrons can be tracked back to infinity, where the Maxwellian distribution prevails. The inbound electron density is given at any radius by

$$\begin{aligned} n_e^{in} &= \int_{-\infty}^{\infty} \int_{\pi/2}^{\pi/2} \int_{\sqrt{|q|\phi/m_e}}^{\infty} n_\infty \left(\frac{m_e}{2\pi kT}\right)^{3/2} \exp\left(-\frac{\frac{1}{2}m_e(v^2 + v_z^2) + q\phi}{kT}\right) v \cos\theta dv d\theta dv_z \\ &= \frac{n_\infty}{2}. \end{aligned} \quad (3.36)$$

Substituting (3.35) and (3.36) into (3.34), Then, we have

$$n_e^{out} + \frac{n_\infty}{2} = n_\infty \exp\left(-\frac{|q|\phi}{kT}\right). \quad (3.37)$$

Given the outbound electron density at the outside boundary, equation (3.37) allows us to calculate the potential there.

The outbound electron density, n_e^{out} is calculated computationally by considering the outbound flux, Γ . The flux through the boundary is given by

$$\Gamma = n_e^{out} v_e^{out} \quad (3.38)$$

where v_e^{out} is the flow velocity due to the outbound electrons, that is, the average

¹In this thesis, we call a particle which is coming into the computational domain, an “inbound” particle, and one going out of the domain, an “outbound” particle.

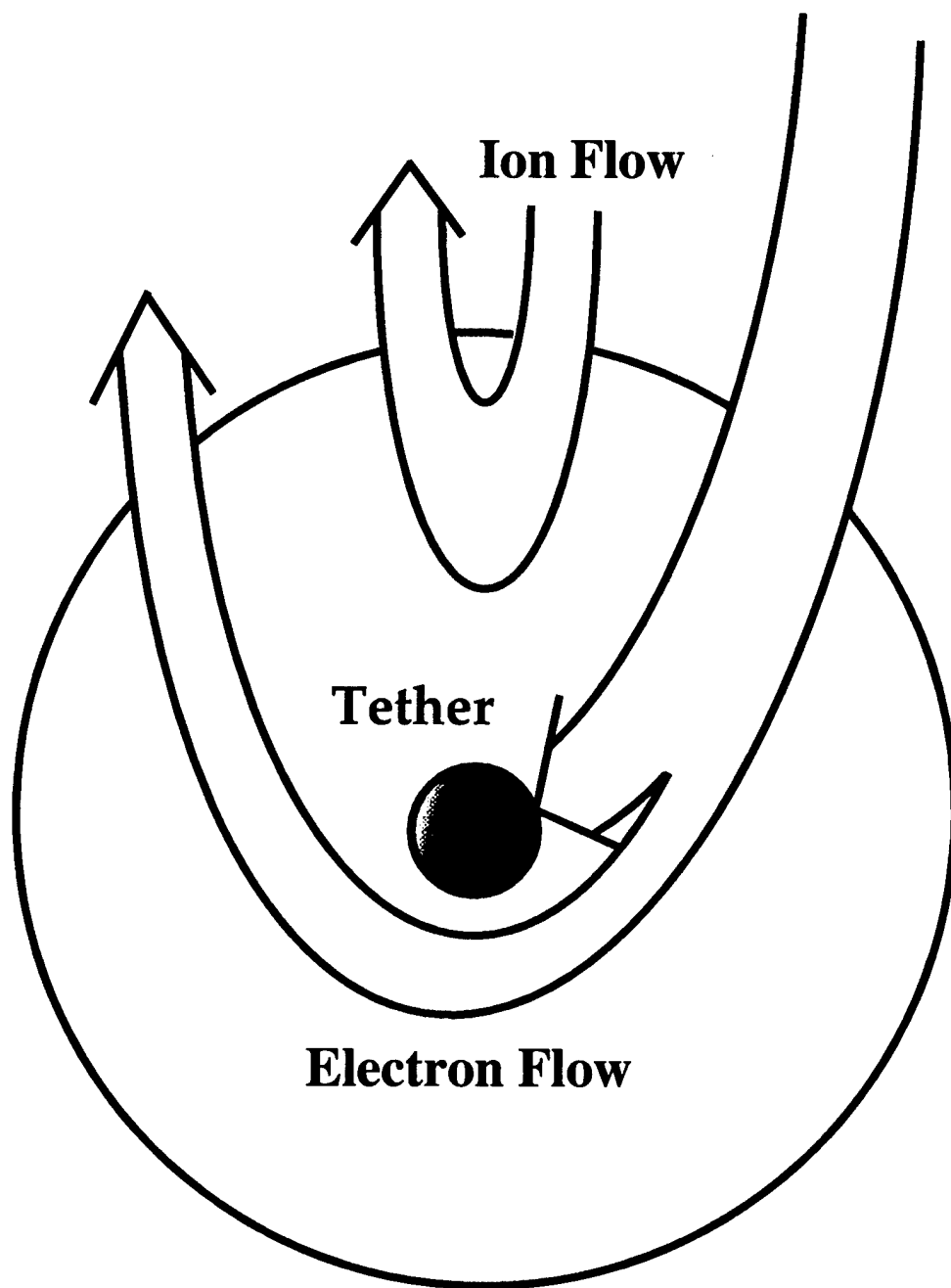


Figure 3-7: Electron and Ion Flow

velocity normal to the boundary, given as

$$v_e^{out} = \frac{\sum_{i=1}^k \mathbf{w}_{ei} \cdot \mathbf{n}_i}{k} \quad (3.39)$$

where k is the number of electrons counted as they cross the boundary, \mathbf{n}_i the normal vector to the boundary and \mathbf{w}_{ei} the particle velocity. The number of electrons which go out of the domain, k , is

$$k = \Gamma dt S \quad (3.40)$$

where dt is the timestep and S is the area of the outside boundary. Substituting (3.40) and (3.39) into (3.38), we have the outbound electron density as

$$n_e^{out} = \frac{k^2}{\sum_{i=1}^k \mathbf{w}_{ei} \mathbf{n}_i dt S} \quad (3.41)$$

Now we are ready to calculate how many electrons and ions are to be replenished at each timestep. The number of those particles is calculated by multiplying the flux by the timestep and the area of the outside boundary. The number of electrons to be replenished, k_e , is given

$$\begin{aligned} k_e &= \int_{-\infty}^{\infty} \int_{\pi/2}^{\pi/2} \int_0^{\infty} n_{\infty} \left(\frac{m_e}{2\pi kT} \right)^{3/2} \exp \left(-\frac{\frac{1}{2}m_e(v^2 + v_z^2) + q\phi}{kT} \right) v^2 \cos \theta dv d\theta dv_z S dt \\ &= \frac{n_{\infty} \bar{c}_{\infty}}{4} \left\{ \frac{2}{\sqrt{\pi}} \sqrt{\frac{|q|\phi}{kT}} + \exp \left(\frac{|q|\phi}{kT} \right) \operatorname{erfc} \sqrt{\frac{|q|\phi}{kT}} \right\} S dt \end{aligned} \quad (3.42)$$

where \bar{c}_{∞} is the random thermal velocity given in equation (2.14). It should be noted that this is the same as equation (2.10), except for ϕ instead of ϕ_p . And the number of ions to be replenished, k_i , is given

$$\begin{aligned} k_i &= \int_{-\infty}^{\infty} \int_{\pi/2}^{\pi/2} \int_0^{\infty} n_{\infty} \left(\frac{m_i}{2\pi kT} \right)^{3/2} \exp \left(-\frac{\frac{1}{2}m_i(v^2 + v_z^2) + q\phi}{kT} \right) v^2 \cos \theta dv d\theta dv_z S dt \\ &= 2n_{\infty} \left(\frac{kT}{2\pi m_i} \right)^{1/2} \exp \left(-\frac{|q|\phi}{kT} \right) S dt \end{aligned} \quad (3.43)$$

In the simulation, a random number generator is used to locate the place to be

replenished and provide the particle with a velocity estimated from the Maxwellian distribution function.

3.3.3 Computational Cost

In order to resolve the non-neutral domain, namely a sheath domain, both electrons and ions should be moved. Typically, heavy, slow ions require very long computational time till the ion distribution has converged. To speed up this computation, we use hypothetically light ions, which have the same mass as electrons. The use of such a light ion is justified by the fact that we are only interested in the ion density, and the assumption that no ion is absorbed by the tether and hence that the ion's distribution function is Maxwellian. From this assumption, we can show that the ion density does not depend on the ion mass. That is,

$$\begin{aligned} n_i &= \int_{-\infty}^{\infty} n_{\infty} \left(\frac{m_i}{2\pi kT} \right)^{3/2} \exp \left(-\frac{\frac{1}{2}m_i \mathbf{v}^2 + |q|\phi}{kT} \right) d\mathbf{v} \\ &= n_{\infty} \exp \left(-\frac{|q|\phi}{kT} \right), \end{aligned} \quad (3.44)$$

This fact enables us to use the very light ion, with which the computation gives the ion density in the computational domain. We should note here that the trajectory of light ions is different from that of real ions, but the corresponding density is the same. Actually with these light ions ($m_i = m_e$), we can get the same result as with other ion mass, say $m_i = 1840m_e$, and that more than 5 times as fast.

3.4 Results

In this section, we show the results from our simulation. First, to check our simulation qualitatively, we show and examine the field quantities. In Figures 3-8, 3-9, and 3-10, instantaneous charge densities for the cases of the Debye ratio equal to 1, 2 and 5 are shown. As we would expect, in the vicinity of the tether, there is a region where electrons are dominant and quasi-neutrality no longer prevails. This region is the

“sheath”.

From this electric charge density, we solve by Successive Line OverRelaxaion (SLOR) to obtain the electric potential distributions, which are shown in Figure 3-11, 3-12 and 3-13 for the same cases. These figures clearly illustrate the sheath region in the vicinity of the tether. The electric potential there is positive, indicating the non-neutrality.

Next we examine the quantitative result from the simulation. Figure 3-14 shows the history of current collected by the tether and the corresponding value from the results of *Laframboise*. After some perturbation, the observed current oscillates just below the *Laframboise*'s value. This oscillation is attributed to the small timestep and the small number of particles used in this simulation. The reason why the current collection in the case of $\xi_p = 1$ has a larger amplitude than the others is that the surface area of the tether is smaller than that of the others and thus one particle difference becomes more significant to the current density calculation.

The consistent negative bias in the result (about 7%) is probably due to the grid distortion, as noted before. But more work needs to be done to verify this.

Finally, the figure 3-15 shows the comparison of the current collection obtained in the simulation with the analytical values for different cases of the Debye ratio. From this figure, the PIC method is verified to give the same trend of the analytical solution. In the figure 3-15, current collected is normalized by the random thermal current given by

$$I = Sn_{\infty}|q|\sqrt{\frac{kT_{i,e}}{2\pi m_{i,e}}} \quad (3.45)$$

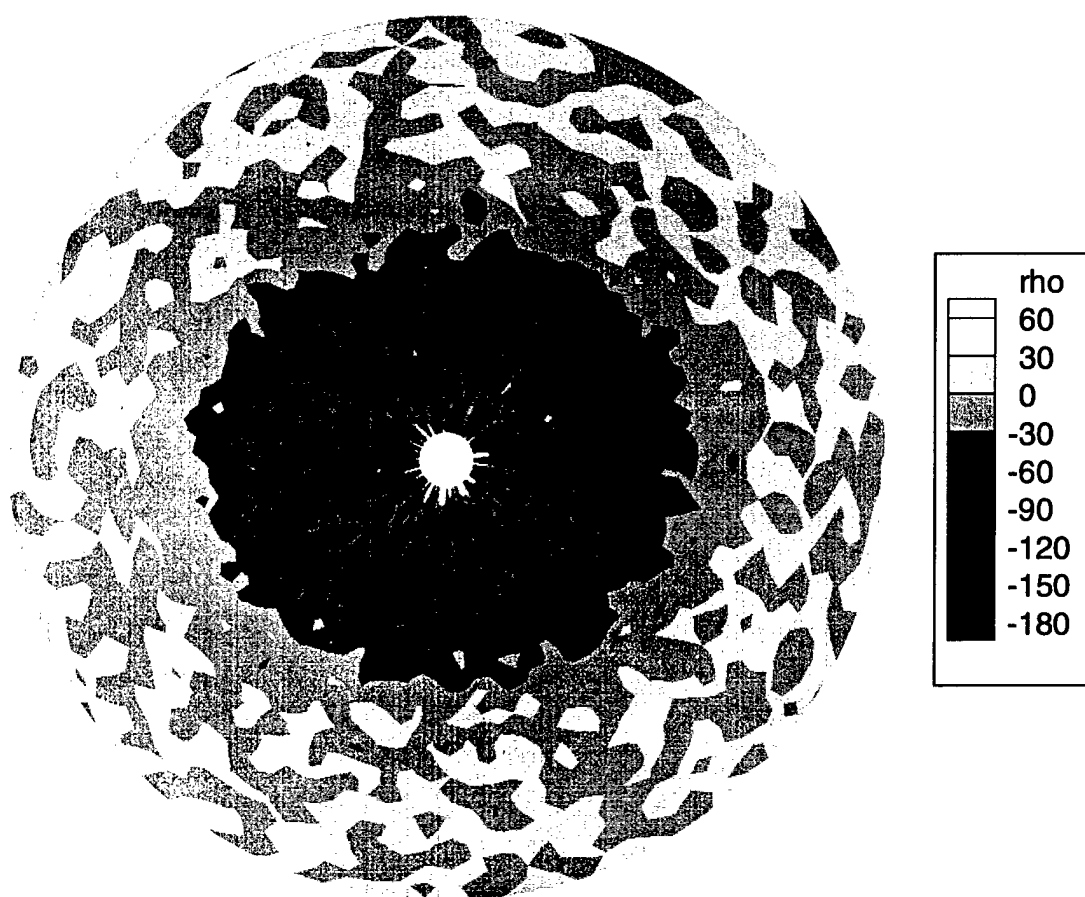


Figure 3-8: Electric charge density for the case $\xi_p = 1$

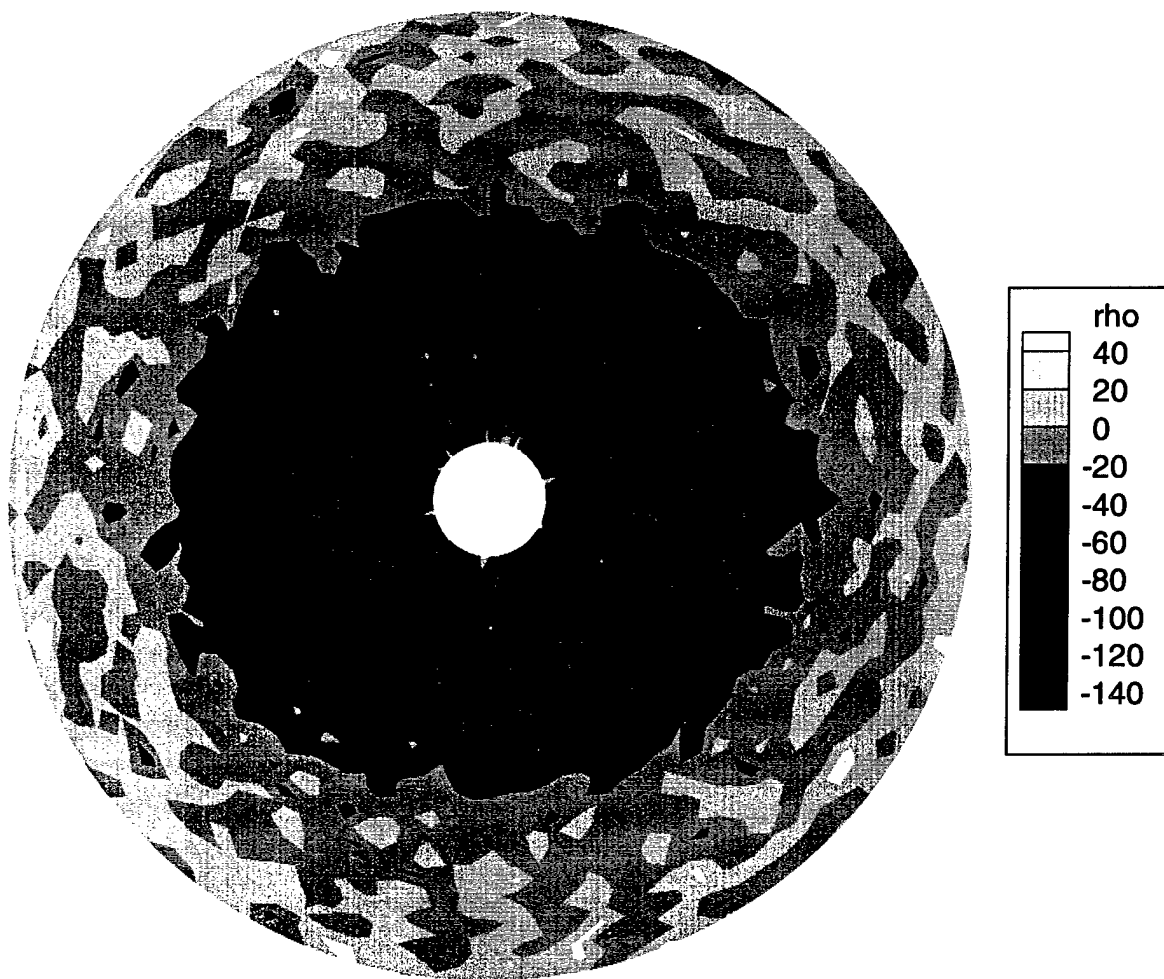


Figure 3-9: Electric charge density for the case $\xi_p = 2$

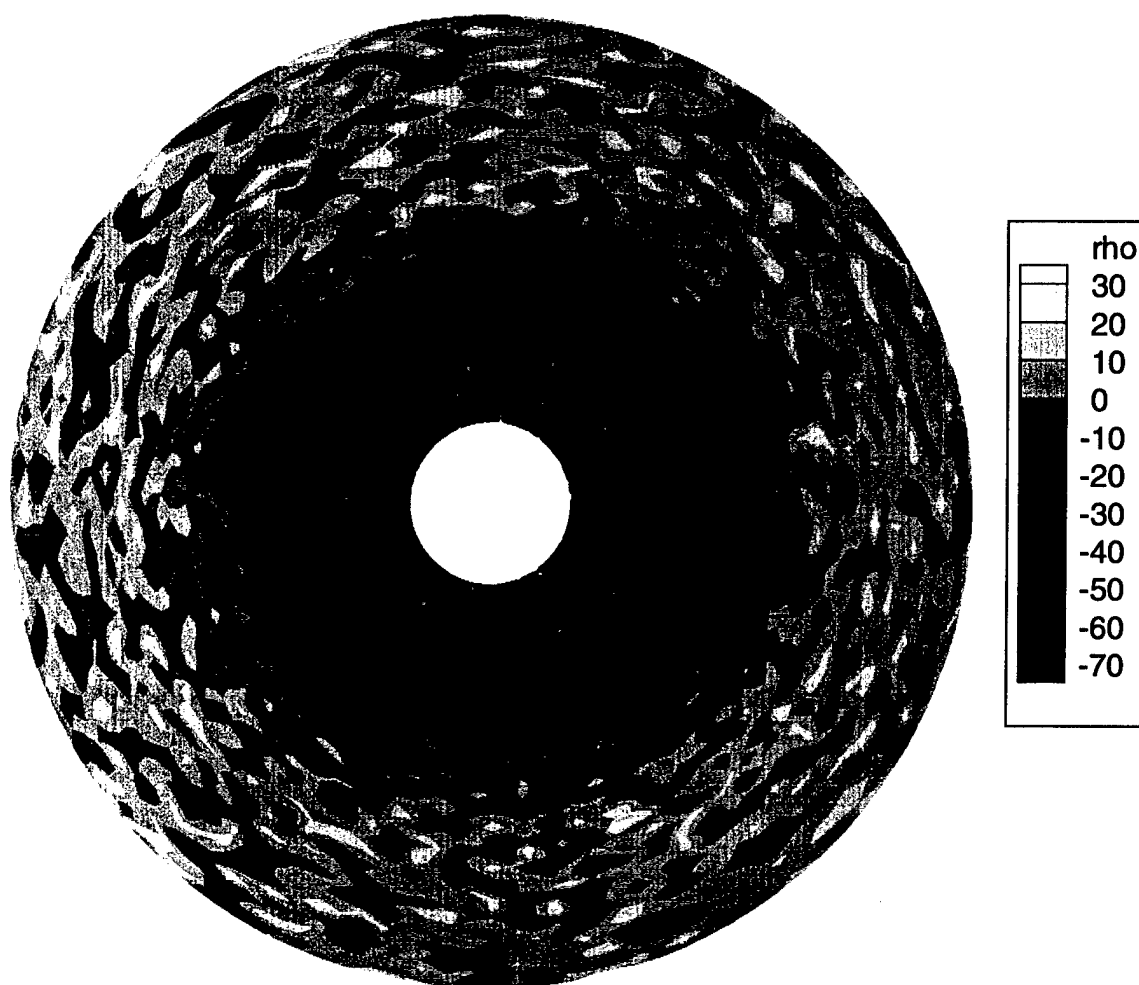


Figure 3-10: Electric charge density for the case $\xi_p = 5$

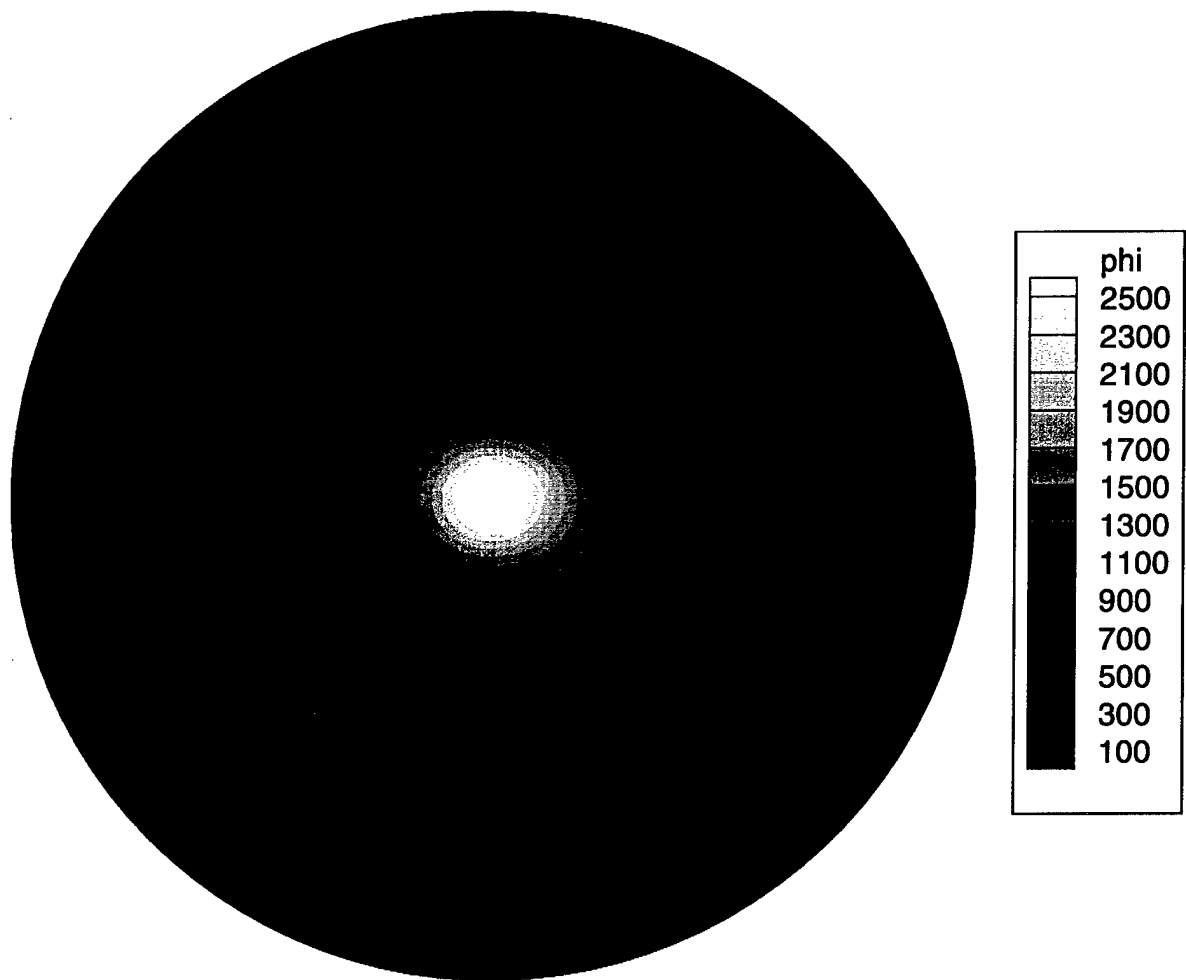


Figure 3-11: Electric potential distribution for the case $\xi_p = 1$

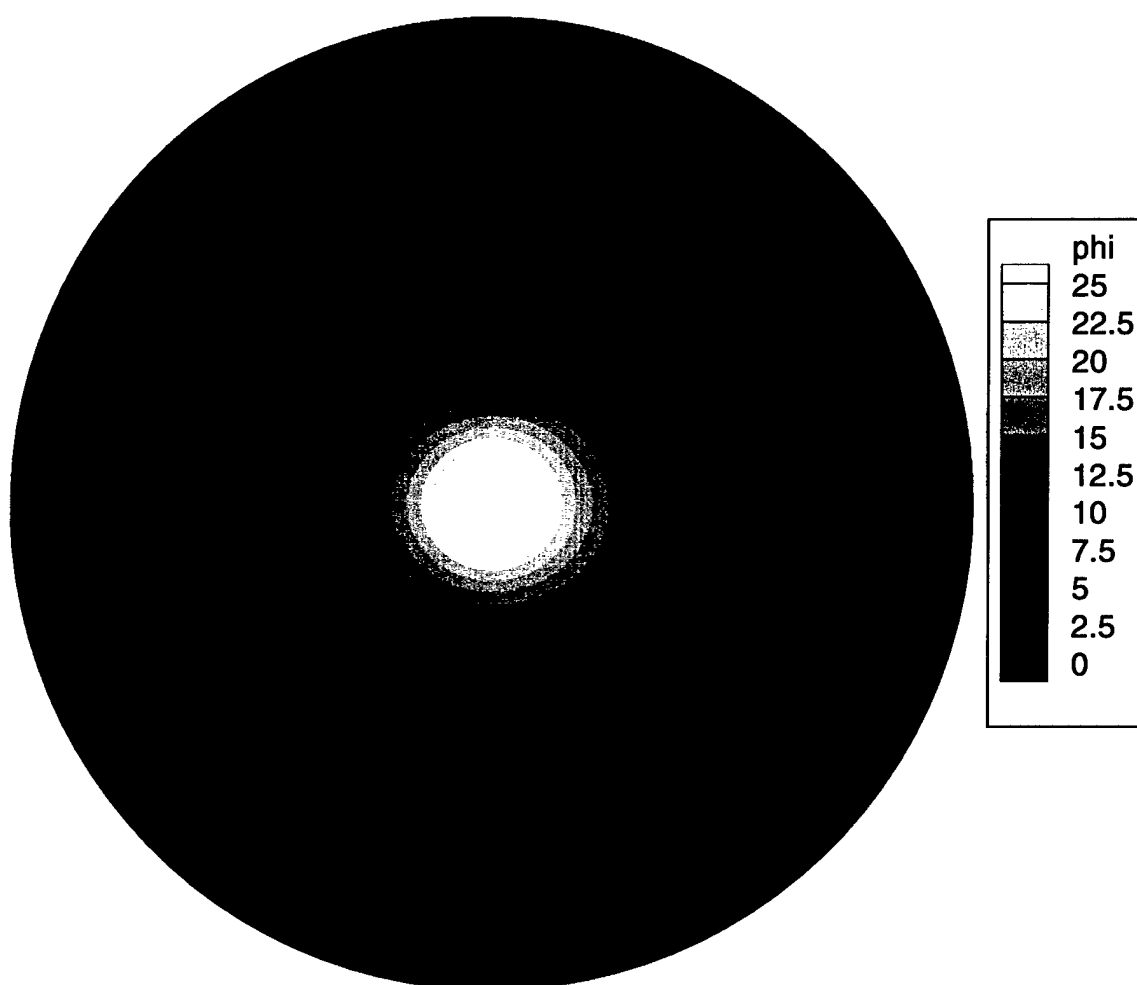


Figure 3-12: Electric potential distribution for the case $\xi_p = 2$

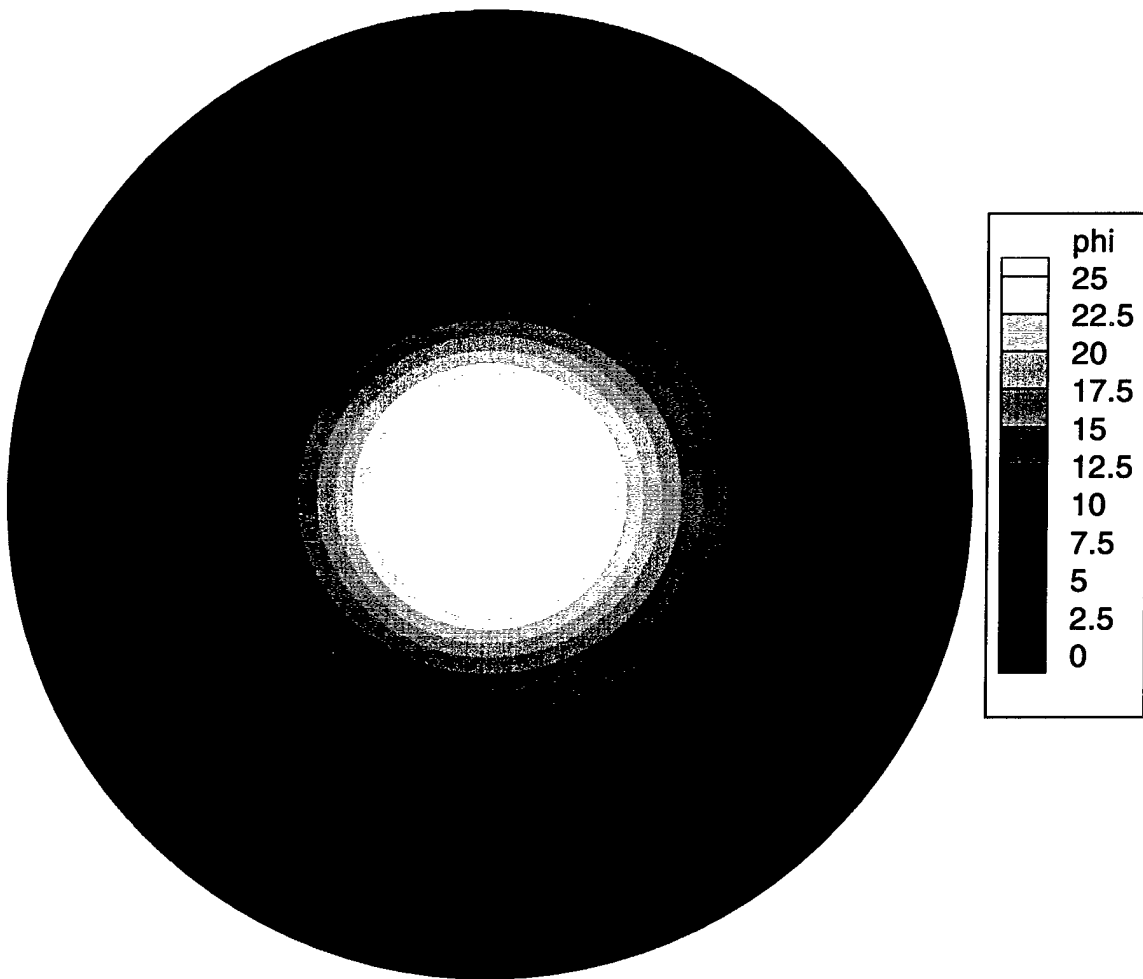


Figure 3-13: Electric potential distribution for the case $\xi_p = 5$

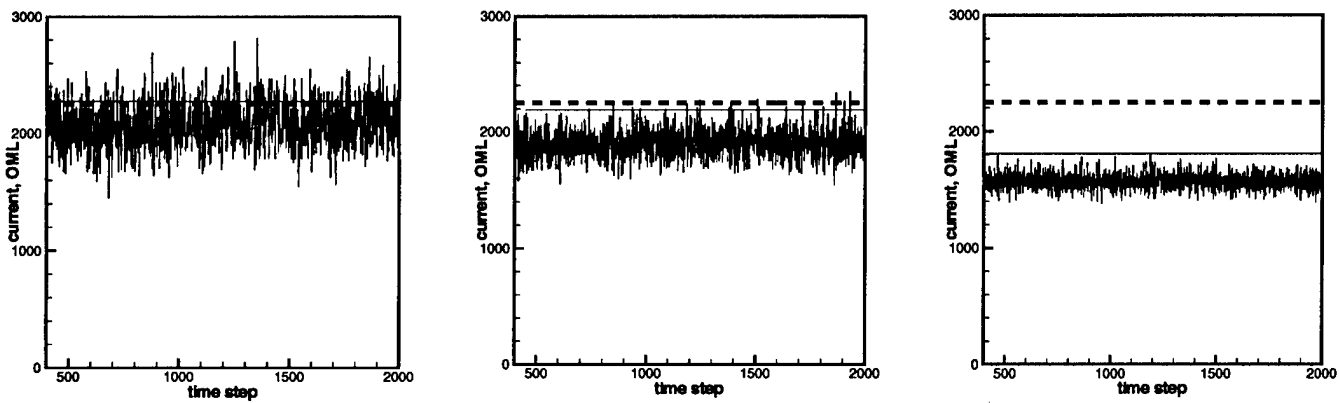


Figure 3-14: History of the Current collection (left) $\xi_p = 1$, (middle) $\xi_p = 2$ and (right) $\xi_p = 5$, the OML current (dashed line) and the exact value (solid line)

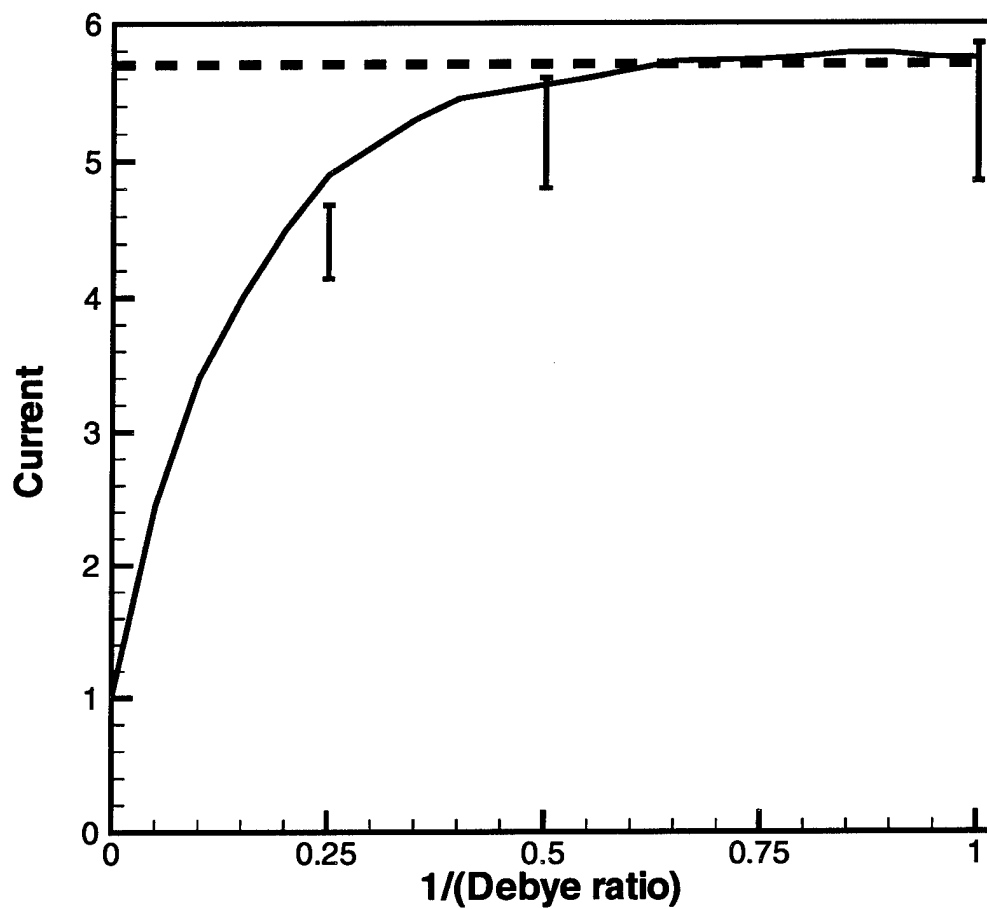


Figure 3-15: Current collection vs. $1/\xi_p$. OML current (dashed), the exact value (solid) and computed value (error bars)

Chapter 4

Conclusion & Further Work

In this chapter, we conclude the possibility and perspective of PIC method to be applied to the space engineering, based on what we discussed in previous chapters. First, we re-state the result from the PIC simulation.

(1) PIC method qualitatively shows the same trend of the current collection with the analytical solution

Figure 3-14 illustrates the exact current collection as a function of the Debye ratio and the value obtained from our simulation. As the Debye ratio decreases, the amount of current collected by the tether gets closer to the limiting value. This limiting value is the one shown by equation (2.13). And as the ratio increase, the current collection decreases. This is because of the bump in the effective potential which prevents the particles from reaching the surface of the tether even if the particle has an enough energy to reach the surface.

(2) PIC method quantitatively shows the current collection with 7% error from the analytical value for all cases of Debye ratio

As illustrated in Figure 3-14, the amount of current collected by the tether oscillates just below the analytical value. The cause of the error can be attributed to the distortion of the grid, as noted before. To avoid this problem, we plan to use different

methods for the interpolation. One possibility is to use the triangular grid with the area-weighting function analogous to one we use in this thesis. The use of the triangular grid does not need the linear interpolation, therefore we can expect to get rid of the error caused by the distortion of the grid.

(3) The current collection code requires non-zero potential as an outside boundary condition.

The partial absorption of electrons requires non-zero potential region, “pre-sheath” outside the sheath. The pre-sheath extends very far. To run the simulation on a relatively small grid, we need to know the local potential at the computational outside boundary. This potential was calculated from the equation of quasi-neutrality. The quasi-neutrality equation relates the local potential to the instantaneous outbound electron density. We calculated the density from the outbound electron flux.

(4) The current collection code can reduce the computational time by using a hypothetically light ion mass.

Since we are only interested in the ion density, not in the ion trajectories, we can use a very light ion mass. The reasonable assumption that no ion is absorbed by the tether allows us to use a very small ion mass. Since the ion density does not depend on the ion mass, when the ions have Maxwellian distribution, the light ion becomes a critical factor to speed up the computation considerably.

Based on this PIC method, we plan to consider (1) the case of flowing unmagnetized plasma, and (2) the case of magnetized plasma as seen in the space engineering application. For either case, the tether potential is still high and, therefore, we can still use the light ion mass. As for the symmetry of the phenomena, we have not taken into account so far any symmetric conditions except for the outside boundary potential, which is taken as an average. This only symmetric condition can be removed by applying local potential values. Therefore, practically this method does not need any symmetry conditions. For future applications, where the symmetry condition is no longer valid, we can apply our PIC method without a substantial modification.

Bibliography

- [1] Charles K. Birdsall and A. Bruce Langdon. *Plasma physics via computer simulation*. Institute of Physics Publishing, Bristol and Philadelphia, 1991.
- [2] P. M. Chung, L. Talbot, and K. J. Touryan. *Electric Probes in Stationary and Flowing Plasmas; Theory and Application*. SPRINGER-VERLAG, 1975.
- [3] H. Goldstein. *Classical Mechanics*. Addison-Wesley Pub. Co., Massachusetts, 1980.
- [4] J.G. Laframboise. Theory of spherical and cylindrical langmuir probe in a collisionless, maxwellian plasma at rest. Technical Report 100, University of Toronto Institute of Aerospace Studies Report, 1966.
- [5] J.G. Laframboise. Current collection by a positively charged spacecraft: Effects of its presheath. *Journal of geophysical research*, 102(A2), February 1997.
- [6] S. Langmuir and H. M. Mott-Smith. The theory of collection in gaseous discharge. *Physical Review*, 28, October 1926.
- [7] D. Seldner and T. Westermann. Algorithms for interpolation and localization in irregular 2d meshes. *Journal of Computational Physics*, 79:1–11, 1988.
- [8] J. Wang, P. C. Liewer, S. R. Karmesin, and D. Kondrashov. 3-d deformable grid electromagnetic particle-in-cell for parallel computers. *AIAA*, (97-0365), 97.